Mass & Energy Efficient Tin Laser Produced Plasma Light Sources

Ph.D. thesis, Vrije Universiteit Amsterdam, 2025
Mass & Energy Efficient Tin Laser Produced Plasma Light Sources
Yahia Mostafa

Cover: A photograph of handmade wheel-thrown porcelain vases representing the laser driven propulsion of plasma through a liquid tin sheet.
Printing: Ridderprint | www.ridderprint.nl.

An electronic version of this dissertation is available at: research.vu.nl

VRIJE UNIVERSITEIT

Mass & Energy Efficient Tin Laser Produced Plasma Light Sources

ACADEMISCH PROEFSCHRIFT

ter verkrijging van de graad van Doctor of Philosophy
aan de Vrije Universiteit Amsterdam,
op gezag van de rector magnificus
prof.dr. J.J.G. Geurts,
in het openbaar te verdedigen
ten overstaan van de promotiecommissie
van de Faculteit der Bètawetenschappen
op vrijdag 10 januari 2025 om 13.45 uur
in een bijeenkomst van de universiteit,
De Boelelaan 1105

door

Yahia Mostafa

geboren te Gizeh, Egypte

promotor: dr. O. O. Versolato
copromotor: dr. J. Sheil

promotiecommissie: prof.dr. K.S.E. Eikema
prof.dr. P.C.M. Planken
prof.dr. G.J. van Rooij
dr. A. Diallo
dr. E. Olsson

The work described in this thesis was conducted at the Advanced Research Center for Nanolithography (ARCNL), a public-private partnership between the University of Amsterdam (UvA), the Vrije Universiteit Amsterdam (VU), Rijksuniversiteit Groningen (UG), the Dutch Research Council (NWO), and the semiconductor equipment manufacturer ASML.

This project has received funding from the European Research Council (ERC) under the European Union's Horizon 2020 research and innovation programme [ERC StG 802648].

Contents

Symbols & Abbreviations vii

Introduction 1

1 Extreme Ultraviolet Broadband Imaging Spectrometer 9
- 1.1 Introduction . . . 9
- 1.2 Design . . . 10
- 1.3 Results . . . 12
- 1.4 Conclusion . . . 14

2 5% Efficiency of 2 µm Laser Driven Tin Microdroplet Plasma 19
- 2.1 Introduction . . . 19
- 2.2 Experimental Setup . . . 20
- 2.3 Conversion Efficiency . . . 22
- 2.4 Energy Scaling . . . 24
- 2.5 EUV Source Size . . . 25
- 2.6 Conclusion . . . 27

3 Energy Partitioning of 2 µm Laser-Produced Plasma 29
- 3.1 Introduction . . . 29
- 3.2 Experimental Setup . . . 30
- 3.3 Photonic Emissions . . . 32
- 3.4 Ionic Emissions . . . 35
- 3.5 Energy Balance . . . 38
- 3.6 Optimum Emission Plasma . . . 41
- 3.7 Conclusion . . . 42

4 Mass Efficient 2 µm Laser-Produced Plasma 43
- 4.1 Introduction . . . 43
- 4.2 Experimental Methods . . . 44
- 4.3 Theoretical Methods . . . 47
- 4.4 Mass Use . . . 48
  - 4.4.1 Burnthrough . . . 50
- 4.5 Mass Use Dependencies . . . 56
  - 4.5.1 Power Density . . . 56
  - 4.5.2 Pulse Duration . . . 58
- 4.6 Conclusion . . . 59

Conclusion 63

Bibliography 69

List of Publications 75

List of Symbols & Abbreviations

CE	**C**onversion **E**fficiency	%
	of laser light into EUV light	
DUV	**D**eep **U**ltra**v**iolet	nm
	λ =130–400 nm	
EUV	**E**xtreme **U**ltra**v**iolet light	nm, eV
	λ =13.5 nm, E =91.84 eV	
IB	**I**n-**B**and of a spectrum (13.5 nm $\pm$ 1%)	%
IE, IP	**I**onization **E**nergy or **P**otential	eV
OOB	**O**ut **o**f **B**and (spectrum excl. 13.5 nm $\pm$ 1%)	%
SP	**S**pectral **P**urity	%
VUV	**V**acuum **U**ltra**v**iolet	nm
	λ =70–130 nm	

BU	Bottom Up method
	Poirier et al. [1]
CCD	Charge-Coupled Device
DG	Droplet Generator
	or, confusingly, Delay Generator
IBA	Inverse Bremsstrahlung Absorption
ImSpec	Imaging Spectrometer, *see Chapter 1*
MP	Main-pulse
MOPA	Master Oscillator Power Amplifier
PP	Pre-pulse
QE	Quantum Efficiency
RF(E)A	Retarding Field (Energy) Analyzer
RALEF-2D	2D Radiation Arbitrary
	Lagrangian-Eulerian Fluid dynamics
	for finite volume simulations
TGS	Transmission Grating Spectrometer
VP	Vaporization Pulse
ZP	Zone Plate

Introduction

> We write to taste life twice,
> in the moment and in retrospect.
>
> *Anaïs Nin*

Passing information down from person to person, from generation to generation, has enabled the success and spread of humanity. From the origin of languages and the invention of tools, processed materials, and writing, we have empowered our species to progress and advance beyond the natural. For thousands of years, writing and printing have allowed us to memorialize our knowledge, wisdom and experience.

A brief history of printing

Around 200,000 years ago, two (archaic human) children of the ages 7 and 12 imprinted their hands and feet into a travertine boulder [2], see Fig. 1(a). Their prints immortalized their presence by fixing evidence of their existence on a permanent medium. Later in history, homo sapiens utilized prints, on cave rock, clay, and then paper, to provide records of their knowledge and beliefs. This process was first adjusted, to enable repeatability of prints, by the (predynastic) ancient Egyptians around 4000 BC by the introduction of stamps & seals as shown in Fig 1(b) [3].

Printing technologies have evolved since the introduction of these stamps, across a 6000-year period. Babylonian societies utilized stylized signet stones covered in pigments, or mud, to form shapes and stamp personal signatures: 2300 BC. Graphite- and coal-covered paper was used by Confucian scholars to print the Six Confucian Classics: 200 AD. The T'ang dynasty's records depicted Buddha and holy attendants with woodcut prints: 800 AD. Separately controlled clay characters were used by Chinese printers in printing common texts: 1100 AD. Johannes Gutenberg reinvented the Chinese movable type printing using metal types to mass-produce religious books: 1439 AD. Alois Senefelder invented lithographic multicolor printing using acid to cast an image on limestone: 1796 AD. More recently, Nicephore Niepce demonstrated the *photo*lithographic process using a mask of Flemish engravings and bitumen as a photoresist: 1820 AD.

Naturally, the printing process has become more controlled and finer as it evolved. A version of the photolithographic process is utilized in modern semiconductor manufacturing. These nanolithography machines use cast shadows of predesigned masks to print nanoscale electronic features, enabling modern computing and memory devices. Chip manufacturers pattern nanometer-size transistors onto silicon wafers, in the order of 132 million transistors per square millimeter [4]. Although these prints

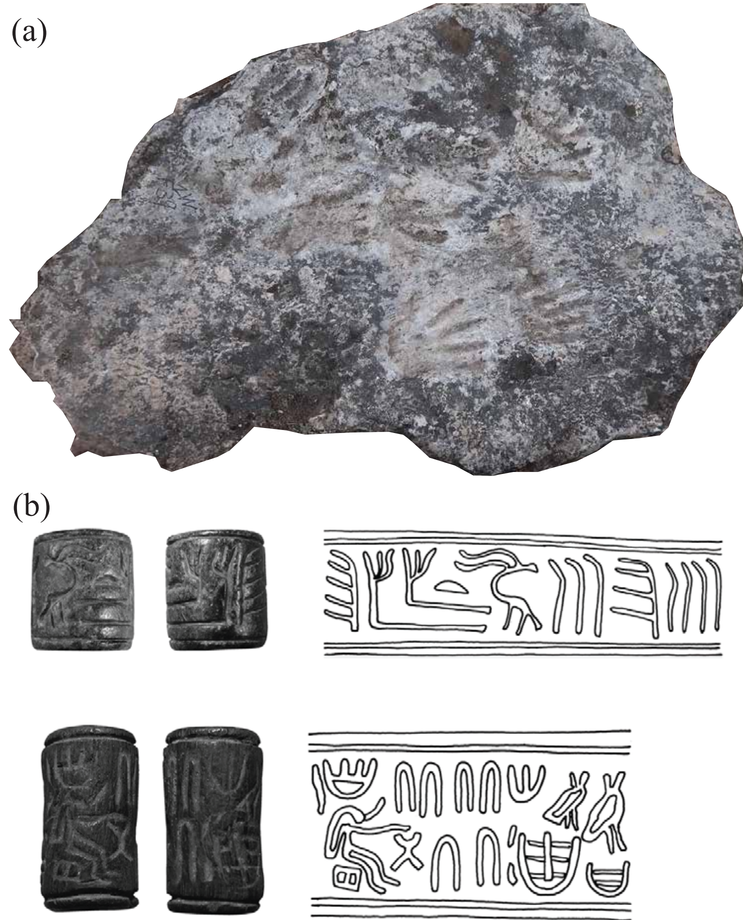

FIGURE 1: Earliest known forms of printing. (a) Prehistoric (200,000 BC) homonin hand and footprints on travertine rock on the Tibetan Plateau [2]. (b) Egyptian Early Dynastic (4000 BC) stamps cylinders (left) and their printed pattern (right) as adapted from [3].

are finer in resolution than the ones shown in Fig. 1, we have essentially returned to printing on rock.

The resolution of a shadow cast by a mask onto a silicon wafer is determined by the Rayleigh criterion and is dependent on chemical and physical factors (denoted by k_1), the color of light used (wavelength denoted by λ) and the numerical aperture (NA) of the device. The smallest distinguishable feature that can be printed is thus $k_1\lambda/NA$. Since smaller semiconductor features result in higher computing power and more efficient processing, it is of great industrial interest to reduce k_1 & λ, and increase NA. State-of-the-art machines utilize extreme ultraviolet light of wavelength $\lambda = 13.5\,\text{nm}$ to drive the lithographic process. In this thesis, we focus on the generation of extreme ultraviolet light.

The choice of extreme ultraviolet light (EUV, 13.5 nm $\pm$ 1%) is guided by the Rayleigh criterion requiring lower wavelengths. The wavelength band is dictated by the available collection and light control mirrors needed to utilize the light in lithography. Many X-ray, vacuum ultraviolet (VUV) and deep ultraviolet (DUV) mirrors exist, with Mo/Si multi-layer mirrors (MLMs) standing out due to their peak reflection occurring at low wavelength and high reflectivity. Mo/Si multi-layer mirrors have achieved peak reflectivity of 70% at a short wavelength of 13.5 nm [5].

Following the availability of mirrors, the criterion for a light source is set. A lithography-relevant light source needs to have the main emission feature be centered at 13.5 nm, matching the mirrors, and have a relatively adequate efficiency to drive this high-volume manufacturing process. Luckily, the abundant elemental tin (Sn, electron configuration: [Kr] $4d^{10}5s^{2}5p^{2}$) has its main emission feature centered perfectly at 13.5 nm, originating from highly ionized (Sn^{10+}–Sn^{14+}) [6, 7].

In modern lithography machines, tin is excited to highly ionized states in a high density ($\sim 10^{19}$ e/cm^3), high temperature (∼30 eV) plasma driven by the impact of a high-power density laser on a liquid tin target [8].

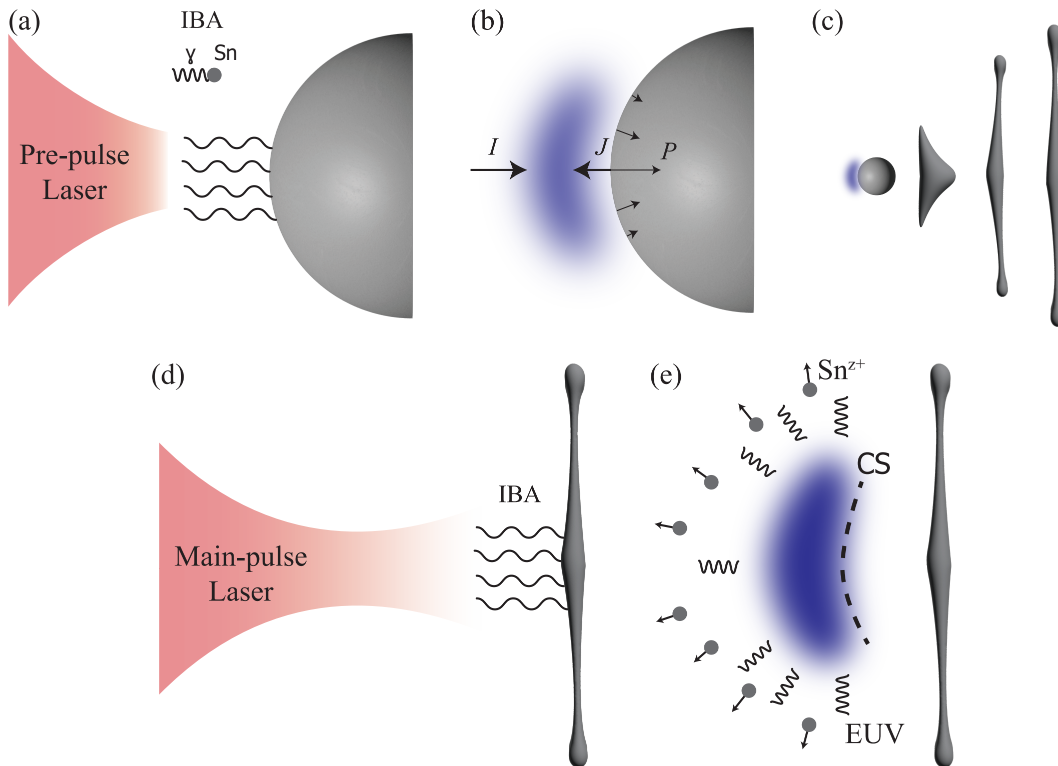

FIGURE 2: Schematic side-view impression of the laser-produced tin plasma light sources which are relevant for this thesis. Subfigures (a)-(c) describe the pre-pulse process and (d), (e) describe the main-pulse. (a) The front part of the tin droplet is irradiated with a 1 µm laser light where it is absorbed by the tin through inverse bremsstrahlung absorption (IBA). (b) With a sufficiently high laser intensity I, the energy deposited generates a tin plasma which drives further mass flow J and imparts a pressure impulse P on the liquid tin. (c) The pressure impulse induces hydrodynamic deformation of the droplet into a thin sheet profile. (d) After a predetermined expansion time of the sheet, a higher energy main-pulse impacts the tin target. (e) The main-pulse driven plasma establishes a quasi-stationary ablation front best described by the critical surface (CS). The plasma emits light and debris in the form of tin particles and ions of several charge states z.

Droplets of tin are streamed at multiple kHz where they are first impacted by a low energy ‘pre-pulse’ as shown in Fig. 2(a) [8]. Through inverse bremsstrahlung absorption (IBA), tin atoms heat up and ionize, generating a plasma at the front of the tin droplet. The generated pre-pulse plasma is maintained by the laser intensity I and a mass flow rate J as in Fig. 2(b) [9]. The plasma expansion imparts a pressure

impulse P on the surface of the droplet which causes hydrodynamic deformation as highlighted in Fig. 2(c) [10, 11]. The droplet then deforms and expands into a thin ($\sim$100s nm), wide ($\sim$100s µm) sheet [10, 12].

The pre-pulse induced deformation optimally prepares the target to absorb a larger higher energy 'main-pulse'. After a preset delay between the two pulses, to allow for hydrodynamic expansion of the tin mass, the main-pulse impacts the tin sheet generating the high-density, high-temperature plasma (Fig. 2(d) and (e)). A critical surface (CS) forms where the plasma oscillation frequency matches that of the laser light, leading to high absorption of the energy in the plasma volume preceding this surface [9]. The plasma establishes a steady-state profile throughout the laser pulse [9] where energy and mass are provided by the laser and tin sheet, respectively.

The laser-maintained tin plasma emits light into various wavelength bands, charged tin ions, and neutral debris [8, 13]. In an industrial setting, the EUV light is collected using a concave Mo/Si MLM that reflects the light and channels it further along the lithography machine. The reflectivity and lifetime of the MLM are affected by the plasma emissions. Unreflected (non-EUV) emissions heat up the mirror, potentially deforming its carefully designed curvature [14, 15]. High energy tin ions may implant into and etch the mirror surface affecting the reflectivity [16]. Finally, neutral cluster debris deposited on the mirror surface absorbs the EUV light and reduces the reflectivity [13]. Accordingly, plasma non-EUV and ionic emissions need to be minimized, or mitigated [17], in order to extend the MLM lifetime and reduce operation cost. Thus, an energy and mass efficient plasma light source is vital to the successful operation of the EUV light source.

Energy-Efficient Plasma Sources

In modern nanolithographic machines, the CO_2 laser (10.6 µm wavelength) driving the EUV generation consumes the majority of the energy of the machine (∼1 MW) [18]. With a wall-plug (electrical to optical) efficiency of 3.6 % [18], the bulk of the energy is lost. Further energy is lost in the conversion efficiency (CE, laser energy to EUV energy) of the generated plasma which is around 6 % [19, 20]. The total process efficiency is around 0.035 % [18]. To improve the efficiency of EUV production, both efficiencies, wall-plug and conversion, need to be addressed.

The wall-plug efficiency is dependent on the optical and mechanical designs of the laser system. Generally, the wall-plug efficiency of solid-state lasers is higher than that of gas-state lasers. For this associated higher efficiency, solid-state drive lasers are an attractive replacement to the CO_2 lasers utilized in high-volume nanolithographic applications. Previous studies have investigated 1.064 µm (Nd:YAG gain medium) wavelengths as a driver for the EUV generating plasma, due to the availability and efficiency of Nd:YAG lasers [21, 22]. On the other hand, 1 µm laser-produced plasmas exhibit a lower CE than their higher 10 µm counterparts [21].

The conversion efficiency of laser light into EUV light is dependent on the laser wavelength and tin target morphology. Langer et al. [23] and Hemminga et al. [24] have investigated the dependence of CE on the laser wavelength, finding an optimum achieved using laser wavelengths of 4 µm for unoptimized targets. Besides CE, the size of the emitting area is important to assess the overall efficiency of the LPP. Ideally, this source size is matched to the etendue of the optics, with typical values ranging 1–3.3 mm^2 sr depending on specifics of the lithography apparatus [25, 26].

Schupp et al. [22, 27] and Behnke et al. [28] have investigated 1- and 2 µm laser-produced plasmas formed from tin droplets in preformed sheets. The driven plasma reaches optimum efficiency at half the laser intensity for the 2 µm laser case [22]. They have found higher conversion efficiencies from 2 µm laser-driven plasmas compared to 1 µm laser wavelength [28]. The higher efficiency is attributed to the increased self-re-absorption of 13.5 nm light in dense 1 µm laser driven plasma compared to the 2 µm case [27]. Further increase in conversion efficiencies is hypothesized for homogenously heated plasma light sources.

Balancing the wall-plug and conversion efficiencies, 2 µm laser-produced plasmas are an attractive alternative to both 1 and 10 µm laser light sources. 2 µm thulium lasers have recently been shown to have wall-plug efficiencies of ∼20 % [29, 30]. On simple solid tin targets, 2 µm wavelengths have achieved higher efficiencies than 1 µm solid-state lasers [28]. In addition to the higher efficiencies, due to the high plasma density generated by low-wavelength lasers, 2 µm laser-produced plasmas may exhibit small source sizes. It is thus interesting to continue investigating the full capabilities of tin plasmas driven by 2 µm laser wavelengths as they combine the advantages of solid-state lasers and higher CEs of longer wavelength drivers.

Mass-Efficient Plasma Sources

Plasma light sources depend on both the energy deposited by the laser and the available tin mass sustaining the plasma as illustrated in Fig. 2(b). Accordingly, efficient plasma light sources can be achieved only when laser drivers interact with sufficient (liquid) mass. The mass use rate, and the optimal mass required to sustain an efficient plasma light source, are essential parameters we study in this thesis.

Optimizing the mass use in a laser-produced plasma source may allow for efficient light emission and limited debris emission. With too little mass in the liquid tin target, the laser-to-EUV-light conversion efficiency may decrease as there are too few emitters (ions) to sustain the high-temperature and density plasma. With too much mass, the extra mass may be deposited on nearby optics or require an increased cost of production to mitigate the emission.

Studies have previously investigated the mass use rate of laser-produced plasma [9, 31]. The mass ablation rate is found to depend on the drive laser intensity and to be inversely proportional to the drive laser wavelength. Since we focus in this thesis on 2 μm wavelength laser-produced plasma due to their high energy efficiency, we investigate the effect of laser intensity on mass use. Based on the mass use rate, we can generate mass-optimized plasma light sources.

In this thesis, we aim to address a fundamental question imposed on tin laser produced plasma light source:

What parameters determine the mass & energy efficiency of tin plasmas driven by a 2 µm wavelength laser?

We address the research question using (primarily) experimental investigations of tin laser-produced plasmas. In a laboratory setting, we study such plasmas under controlled conditions of both the laser and the tin target. Similar to the industrial process, we stream liquid tin droplets and preform their morphology towards thin sheets. Using an in-house built master oscillator power amplifier (MOPA) of 2 µm [32], we generate and EUV emitting plasma from the tin target. The plasma is accordingly studied using EUV selecting diodes, transmission grating spectrometry, plasma EUV imaging, ion detection and energy analysis, along with many other diagnostic and characterization devices of both the laser and the tin target.

Thesis Outline & Summary

The key to successful experimental exploration is proper metrology and instrumentation. As a basis for all the topics discussed in this thesis, we paid serious consideration to the experimental tools utilized. EUV sensitive diodes have been routinely tested and cross-calibrated to maintain accurate quantification of EUV emission. Fast-response EUV diodes were installed to enable time-resolved characterization. A new high resolution EUV imaging tool was introduced, characterized and calibrated to shed insight onto the emission area, size and morphology of the plasma radiance. Furthermore, we begin this thesis by demonstrating a novel measurement instrument which is to be added to the arsenal of experimental techniques in future research.

Chapter 1 presents an imaging spectrometer capable of simultaneously acquiring wavelength resolved 1-D images in the range 5–80 nm to study plasma light sources. Using a combination of a transmission grating and a carefully designed set of 1-dimensional zone plates, both the full spectrum and images of each component wavelength can be captured. We demonstrate here the capabilities of the device and correspond it to plane-wave propagation simulations. The simulations confirm the performance of the device and shed further understanding on the limitation of its resolution. We hope this imaging spectrometer is further used to characterize laser-produced plasma light sources, revealing insight into their spatial structure.

In **Chapter 2**, we demonstrate laser-to-EUV light conversion efficiencies of plasmas driven by a 2.1 µm wavelength laser. High conversion efficiencies of up to 5 % are shown for driver laser pulses with uniform spatio-temporal intensity profiles. The constant intensity profiles generate plasma of optimum temperature for EUV emission, across space and time. We further demonstrate the scaling of emission energies with increase of: average laser intensity, beam diameter and pulse duration. Investigating further the plasma emission area we conclude that pulse duration is an optimal parameter to scale EUV emission energies. All source emission areas we report are smaller than typical source sizes required by etendue limits in high-volume manufacturing. We thus here provide insight into creating high efficiency, high energy, compact tin light sources driven by 2 µm lasers.

Chapter 3 addresses the energy balance of 2 µm laser produced plasmas. The measured energies of emitted light and ions are weighed against the input energy to the

plasma, the laser energy. We show that we are able to reconstruct a significant fraction of the laser energy of up to 82 %. We identify out-of-band UV emissions to be the dominant energy loss channel, followed up by ion kinetics. Investigations of the change of energy partitioning as a function of laser power density reveal higher than optimum intensities (determined by most efficient EUV emission) show a decrease in ion kinetic energies and out-of-band emissions. We have thus identified channels of energy loss in 2 μm laser produced tin plasmas and gained understanding of their dependencies on laser parameters to allow mitigation.

Contrary to the preceding two chapters, which address energy efficiency, **Chapter 4** undertakes the *mass* use efficiency of 2 μm LPPs. Preformed tin targets where used to vary the mass overlapping the flat-top laser beams driving the plasma. We show that sheet thickness, for sheet diameters larger than the beam, is a strong determinant for mass and energy efficiency of the plasmas discussed.

Chapter 1

Extreme Ultraviolet Broadband Imaging Spectrometer Using Dispersion-matched Zone Plates

The best investment is in the tools of one's own trade.

Benjamin Franklin

We present simultaneous 1D imaging and broadband spectroscopy of a laser-produced plasma (LPP) source of extreme ultraviolet light, using a tapered zone plate that is matched to the dispersion of a transmission grating. We describe the design and fabrication of the zone plates in the 5-80 nm wavelength regime with designed spatial resolution of ∼10 µm and spectral resolution of ∼0.8 nm. Subsequently, we benchmark the imaging spectrometer with a solid tin target LPP. Plane wave propagation simulations qualitatively match the experimental results and confirm the device performance.

1.1 Introduction

The reliability, throughput, and efficiency of extreme ultraviolet lithography machines depend on the characteristics of the EUV light source, which is currently a laser-produced plasma (LPP) generated from microdroplets of tin [33–36]. This tin LPP emits light from the soft x-ray to the visible region, with its emission peaking in the 13.5 nm ± 1% "in-band" region where multilayer mirrors (MLMs) can be employed to guide the light [37]. Maximizing in-band emission compared to the complementary out-of-band emission improves the quality of the EUV source [38, 39]. Out-of-band EUV light contributes to collector mirror heating and ionization of ambient hydrogen gas which can damage nearby optics. Additionally, out-of-band light cannot be reflected by the narrow-bandwidth multilayer mirror optical systems employed in EUV lithography and contributes to power loss [37, 40]. Longer-wavelength, deep ultraviolet emissions may still be reflected by the MLMs and expose the wafer, potentially reducing the pattern contrast [14, 15]. Accordingly, it is critical to investigate the emissions in the out-of-band region.

The contents of this chapter have been published as denoted in List of Publications. Minor changes to the introduction have been made to ensure readability within the thesis.

Two fundamental techniques for characterizing plasma sources are spectroscopy and imaging. The spectrum of a microdroplet tin LPP in a 5.5–265.5 nm wavelength range was previously studied [37]. However, this emission spectrum represents the spatial average across the plasma and does not provide information on the spatial distribution of the emission. This distribution is key for understanding the further transport of light through the complex optics system. Understanding the spatial distribution provides the means for optimizing source brightness in the EUV regime while obtaining information on the emission area in (deep) ultraviolet wavelength band enables assessing how much of the light falls within the etendue – and would potentially contribute to wafer exposure. Spatial information of the emission can be obtained using, e.g., pinhole or concave mirror imaging since refractive elements are not applicable due to the high absorption of EUV light. Concave mirror imaging however relies on wavelength-dependent reflections limiting numerical aperture (NA) and is particularly alignment sensitive. The more accessible technique of pinhole imaging is typically limited in resolution given the minimum available distances to the plasma, leading to a low NA. For 1D imaging, the pinhole may be changed to a slit to increase transmission.

Generally, when combining imaging with wavelength selectivity, established imaging techniques are restricted to either very broad wavelengths (e.g., pinhole imaging combined with a metallic filter) or very narrow bandwidths (e.g., imaging using MLMs). Fresnel zone plate (ZP) optics provide an alternative method of focusing EUV light [41–43], enabling a combination of relatively high NA and long working distances. ZPs can be accurately fabricated using nano-fabrication techniques, and have been successfully applied as high-resolution focusing lenses for arbitrary, single wavelengths of light ranging from the soft-x-ray to UV region [42, 44, 45]. However, Fresnel ZPs are highly chromatic. As a result, only a narrow wavelength band can be imaged from light emitted by a broadband plasma source, with the other wavelengths being out of focus.

We present an imaging spectrometer operating across a broad 5-80 nm range with a spectral resolution of $\sim$0.8 nm (at 13.5 nm), combined with a designed spatial resolution of $\sim$10 µm. This novel device employs a transmission grating in series with a set of one-dimensional zone plates that are individually matched, or *tapered*, to a particular wavelength according to the grating dispersion. We note that the concept of Fresnel zone tapering was introduced previously, but for optimizing single- and not for multi-wavelength operation [46–48]. Our imaging spectrometer is designed for one-dimensional imaging of plasma light sources in the extreme, vacuum, and deep ultraviolet regimes.

1.2 Design

Fig. 1.1a shows a 3D schematic view of the setup, demonstrating the laser impacting a solid tin target, along with the operation of the imaging spectrometer. In Fig. 1.1b and c, we show the diffraction axis and the imaging axis respectively. At a distance $p_1 = 53$ cm, a 150 µm slit is used in combination with a 780 lines/mm transmission diffraction grating to disperse the light. The diffracted light impacts a set of 1D-wavelength-tapered zone plates at a distance $p_2 = 5$ cm from the diffraction grating. The zone-plates image the source onto a back-illuminated Greateyes (GE2048 512BI UV1) CCD at a distance $q = 110$ cm. This combination of distances results in a magnification $M = 1.9$.

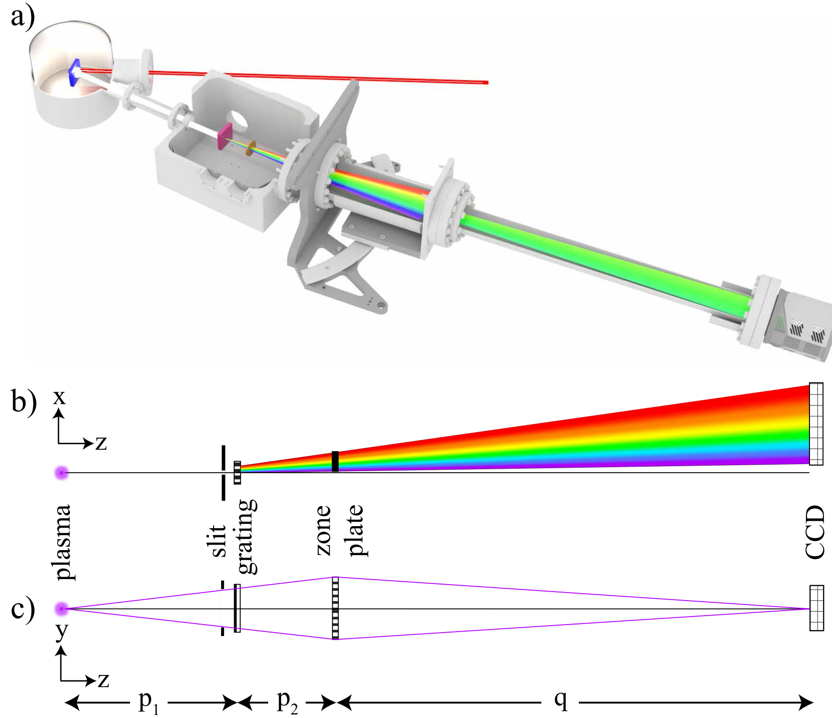

FIGURE 1.1: a) Schematic 3D overview of the experimental setup, b) Top-down view showing the spectrometer axis (x) and c) Side view showing the imaging axis (y).

We show the design of the zone plate in Fig. 1.2a. Along the diffraction axis, a series of 1D zone-plates are constructed, with each individual zone plate matching a specific wavelength as dispersed by the grating. The radius $r_{i,n}$ of the nth zone of the ith zone-plate, dispersion-matched to the λ_i^{th} wavelength, is determined by

$$r_{i,n} = \sqrt{n\lambda_i\left(f + \frac{n\lambda_i}{4}\right)} \quad \text{with} \quad \lambda_i = d\frac{x_i}{\sqrt{p_2^2 + x_i^2}}, \tag{1.1}$$

where f is the focal distance, d is the grating period of 1.3 µm (corresponding to the 780 l/mm grating) and p_2 and q are as previously described. The spatial resolution of the imaged source is determined by $\Delta w = \lambda f / 2r_N$. In order to maintain near-diffraction-limited performance, the magnitude of the focus shift Δf due to the finite wavelength resolution $\Delta\lambda$ (being 0.8 nm at 13.5 nm for the used grating [49]) should be less than the depth of focus (DOF) of the system. This sets a limit on the useful number of zones of the ZP given by $N \leq \lambda/\Delta\lambda$. Any zones beyond this number do not improve the spatial resolution. In the following, the number of zones N at each wavelength λ_i is set to achieve a constant spatial resolution across all wavelengths, $\Delta w \equiv 10\,\mu\text{m}$. We note that the design choices are highly interwoven, with a higher resolution grating enabling higher spatial resolution in step with wavelength resolution (given the capabilities to produce zone widths below 2 µm, a spatial resolution better than 3 µm would be achievable in principle). However, higher-resolution gratings would reduce the spectral window provided for a single CCD position and the current design presents a trade-off between sufficient magnification, range, and resolution taking into account limitations for the current implementation.

The fabrication process of the ZPs is similar to processes that have been previously

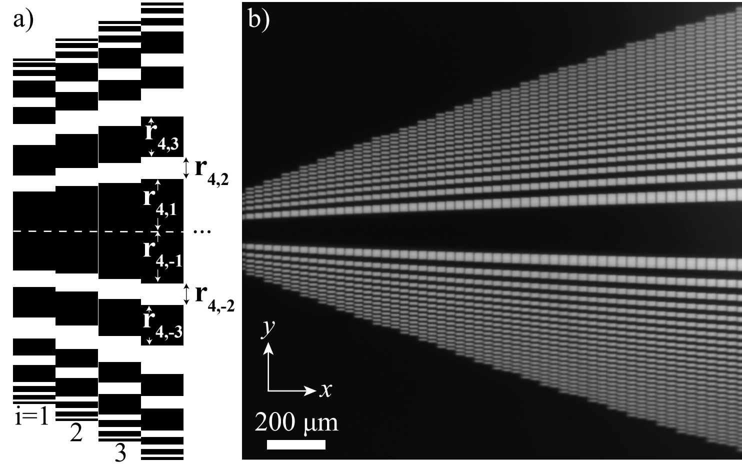

FIGURE 1.2: Dispersion-matched zone plate design. a) A schematic of the design where index i indicates the zone plate number in the dispersion axis. The radius $r_{i,n}$ of the nth zone of the ith zone-plate is given in the text. b) Optical microscopy image of the tapered zone plate designed for the range 5-80 nm.

described [49, 50]. The ZP stack consists of Si_3N_4 (200 nm), Cr (15 nm), Au (200 nm), Cr (15 nm) layers to act as fully absorbing layers to produce an amplitude ZP. Patterns are defined by optical lithography, combined with lift-off and etching. The Si wafer is etched from the backside, enabling free-standing structures. In order to keep the integrity of the absorber zones, periodic vertical support bars are implemented in the design of the system. The width of the support bars is 4 µm with a period of 40 µm. For practical purposes, we use the support bar period as the width corresponding to the spectral resolution $\Delta\lambda$. The effect of any support bars on the measured spectra can be neglected.

1.3 Results

A 1 mm thick poly-crystalline tin target is mounted onto a 2D translation stage in a vacuum chamber held at 10^{-6} mbar. Using an Nd:YAG 1 µm laser, we irradiate the tin target at 10 Hz while regularly moving the stage to irradiate a new spot. The laser beam has a temporal FWHM of 6 ns and a spatial FWHM of 60 µm. We set the laser power density to 1.6×10^{11} W/cm^2 for the measurements shown in this work (cf. Ref. [51]). The imaging spectrometer described in this work is mounted at 30° backward with respect to the laser beam propagation as shown in Fig. 1.1a. First, we only install the transmission grating and exclude the zone plates to obtain the emission spectrum as shown in Fig. 1.3a. It covers the 5-25 nm wavelength range captured at a single CCD position. In all data presented here and in the following a background subtraction has been performed. The CCD image is summed vertically to produce the spectrum shown in the lower segment of the plot. The resulting spectrum is similar to previously obtained spectra for solid and liquid tin LPPs with its main emission feature at 13.5 nm resulting from transitions between multiply excited states in multiply charged tin ions [28, 37–39].

By adding the dispersion-matched zone plate, the wavelength-dependent source image is obtained as shown in Fig. 1.3b. The figure exhibits a central band alongside several diverging features that are the result of the various diffraction orders of the

zone plate. It is the central band, originating from the 1st diffraction order, that represents the 1D source image. The diverging band are the result of 0th, 3rd and 5th order diffraction (even diffraction orders are suppressed [49]). A vertical lineout at $\lambda = 13.5$ nm is shown on the right side of the plot; the spectrum (summed over the central band) is inset on the bottom for comparison.

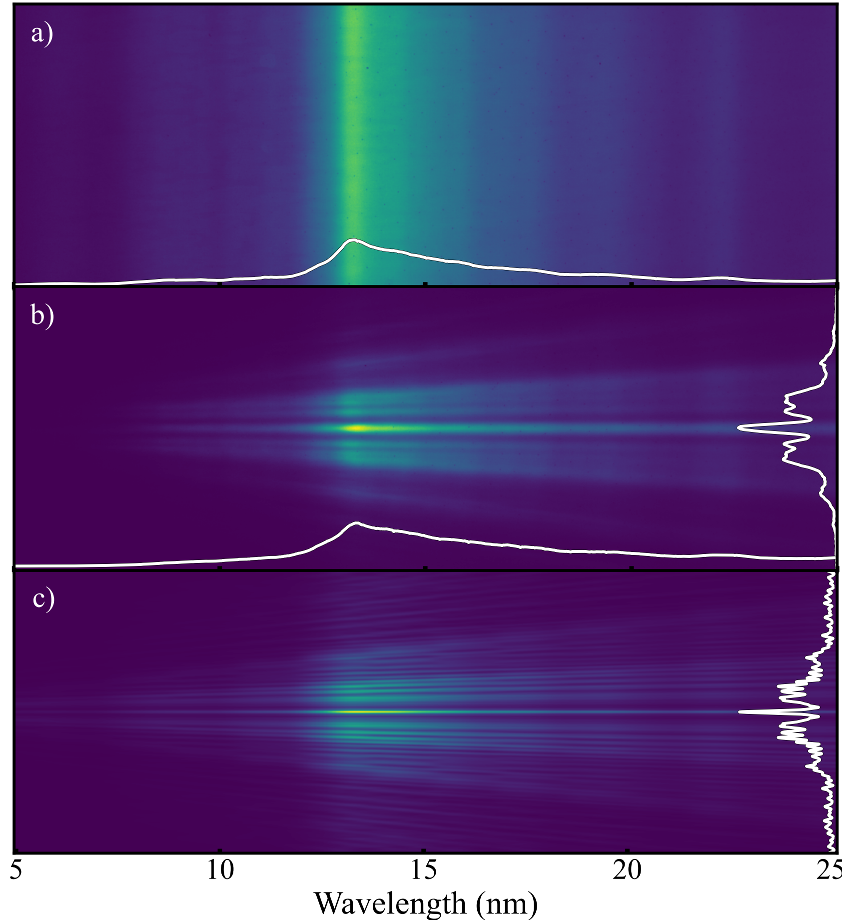

FIGURE 1.3: Experimental and simulation results of tin LPP generated light traversing dispersion-matched zone plates and grating in the 5-25 nm regime. a) Experimentally acquired spectrum from LPP (see main text) without ZP system with the binned spectrum shown as a lineout. b) Experimentally acquired spectroscopic image. The bottom lineout represents the spectrum as averaged across the 1st order (center) image. The right lineout represents the image at 13.5 nm. c) Simulations of the dispersion matched zone-plate system. The right lineout represents the image at 13.5 nm.

To better understand the obtained image, we next execute wave propagation simulations to verify the imaging response of the ZPs, following the angular spectrum method outlined in Ref. [52]. We adopt a simplified scheme and for each wavelength simulate the diffraction of a monochromatic plane wave through its corresponding set of zones. The simulation is repeated for the 3rd and 5th *grating* diffraction orders (i.e. any particular set of zones is impinged on by wavelengths having 1/3 and 1/5 of the value of the corresponding first order). The resulting intensity profile at the focal distance is scaled by the experimentally measured spectrum, summed for all orders weighed by the inverse square of the order as shown in Fig. 1.3c [53]. A vertical lineout across the center of the propagated images (at the focal plane) is taken

and aggregated for all wavelengths. The simulation results are convoluted with a 2D Gaussian function to account for the finite spectral resolution (set to $2\Delta\lambda$=1.6 nm at 13.5 nm along the dispersive axis) which in turn causes image blurring (approximately 8 µm) given that a single zone is impinged on by a wavelength band. The lineout for $\lambda = 13.5$ nm is shown on the right, to be compared to the experimental lineout in Fig. 1.3b.

We observe good qualitative agreement between simulation and experiment. The main differences can be attributed directly to the fact that the LPP has finite size and the obtained image thus gives direct insight into the spatial emission characteristics.

By varying the CCD position laterally, along the dispersive x-axis, we can study the plasma emission for longer wavelengths. The CCD is moved in steps corresponding to the width of the CCD chip while maintaining some overlap between subsequent positions.

In Fig. 1.4a, four such images are stitched by moving the CCD a total of 4° towards the laser axis, corresponding to the wavelength range 5-80 nm. Similar to Fig. 1.3b, the spectrum is obtained along the 1st order image and shown in the lower segment of the plot as a lineout. In Fig. 1.4b we show the spectrum-normalized result in order to remove intensity variation along the x-axis due to underlying spectral variations and highlight the presence of the 1st order image across all wavelengths. We note that some noisy features at the edges of the image, due to low signal levels, and non-perfect stitching features are also visible.

Care should be taken in interpreting the source size in these images. Higher diffraction orders of the grating affect the observed image. The zone-plate's n^{th} diffraction order of an mth grating diffraction order will coincide with the 1st orders on the CCD for $n = m$ (since the focal distance $f_n = r_1^2/n\lambda_m$).

The prominent higher orders are that of the 13.5 nm peak observed at 40.5 nm and 67.5 nm in Fig. 1.4b. Contributions of higher orders to the image however are noticeable only at odd orders of the main emission feature at 13.5 nm and do not impede interpretation of the overall spatial emission characteristics. In specific applications, filters and zone blocks may be added to suppress higher orders if need be, and the concept may be straightforwardly extended to other wavelengths (shorter and longer).

Returning to the dominant 1st order image, we note that its width increases with wavelength, indicating an increasing source size with wavelength. This observation is in line with the expectation that when emission from a hot surface is considered, the temperature reduces moving away from the core. The center of the plasma is the smallest and hottest region of the plasma, responsible for the emission of the shortest wavelengths, as these are emitted by the higher charges states. Longer wavelengths are expected to be emitted from areas away from the core where the temperature is also lower.

1.4 Conclusion

In conclusion, we demonstrate an effective spectrally resolved imaging device for wavelengths in the range 5-80 nm. Using a combination of a transmissive diffraction grating and a sequence of zone plates matched to the diffraction, simultaneous measurement of the emission spectrum and 1D imaging is achieved. We employ the

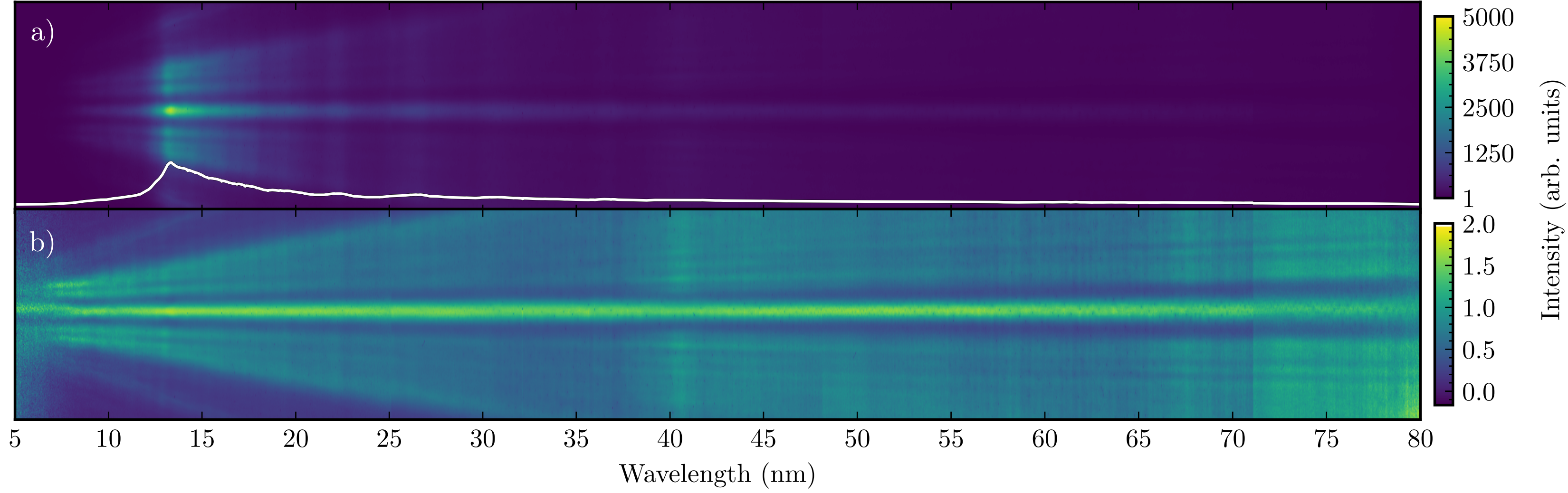

FIGURE 1.4: Experimental results of dispersion-matched tapered zone plates and grating in the 5-80 nm regime. The total image is a composite of exposures at subsequent CCD positions along x. a) The emission spectrum of solid tin target LPP in linear color scale, highlighting the prominence of the 13.5 nm emission feature. The image center is binned vertically and shown at the bottom as a lineout. b) The spectrum-normalized result, highlighting the central image across all wavelengths and the higher grating diffraction orders of 13.5 nm (3rd order at 40.5 nm and 5th order at 67.5 nm).

described device to study laser-produced plasma light sources. The results are supported by wave propagation simulations of the zone plate. Having demonstrated the working principle in proof-of-concept experiments, the imaging spectrometer may find application in plasma characterization studies in the nanolithography field and beyond, e.g., in research on short-wavelength light sources.

Acknowledgments

We would like to thank Henk-Jan Boluijt, Dr. Laurens van Buuren and Caspar Bruineman for their contribution to the design and the construction of the experimental setup, and Dr. Boris Vratzov for the fabrication of the zone plates and gratings, and Dr. Mengqi Du for valuable contribution to the simulations' part of this work.

Funding

This project is funded by TKI-HTSM with the project name "Spectral Unraveling of EUV Lithography Light Sources (SUN)". Part of this work has been carried out within ARCNL and was financed by TKI from the Dutch Ministry of Economic Affairs. The transmission grating spectrometer was developed in the Industrial Focus Group XUV Optics at the University of Twente and supported by the FOM Valorisation Prize 2011 awarded to F. Bijkerk and RVO NanoNextNL Valorisation Grant awarded to M. Bayraktar in 2015. This project received further funding from the European Research Council Starting Grant No. 802648 and is part of the VIDI research programme with Project No. 15697, which is financed by NWO.

Chapter 2

Production of 13.5 nm Light with 5% Conversion Efficiency from 2 µm Laser Driven Tin Microdroplet Plasma

Good is not good, where better is expected.

Thomas Fuller

We demonstrate efficient generation of extreme ultraviolet (EUV) light from laser-produced plasma (LPP) driven by 2 µm wavelength laser light as an alternative for 10 µm CO_2 gas LPP currently employed in EUV lithography machines for high-volume-manufacturing of semiconductor devices. High conversion efficiencies of laser light into 'in-band' EUV photons up to 5.0% are achieved by homogeneously heating the plasma that is laser-generated from preshaped tin microdroplet targets. Scaling the laser pulse duration, spot size, and intensity yields a high in-band EUV energy output of up to 12.5 mJ. The EUV emission source size is studied under a similar parameter range and is shown to match typical etendues of EUV optics columns. Our findings make 2 µm LPP a particularly promising candidate to power future EUV nanolithography.

2.1 Introduction

Today's most advanced nanolithographic machines utilize extreme ultraviolet (EUV) light to 'print' ever smaller features on chips [54, 55]. EUV light is generated by laser-produced tin plasma sources driven by 10.6 µm wavelength CO_2 gas lasers [8, 20]. Laser light impacting tin microdroplets generates plasmas that contain highly excited, multiply charged ions that emit EUV light primarily in the 2% 'in-band' region around 13.5 nm [5–7, 56]. Generated EUV light can be collected using concave multilayer reflective optics enabling the lithographic process [5].

The contents of this chapter have been published as denoted in List of Publications. Minor changes to the introduction have been made to ensure readability within the thesis.

A revision of the calibration of EUV sensitive diodes suggests that actual EUV emission values are approximately 10% lower than the values reported here.

The performance of laser-produced plasmas (LPP) is assessed in multiple ways, primarily by the conversion efficiency (CE) of laser light into in-band light emitted in the 2ß hemisphere facing the laser. Current nanolithographic machines using CO_2 lasers have a CE of approximately 5–6%, emitting several 10 mJ of in-band radiation per pulse [19, 20]. Besides CE, the size of the emitting area is important to assess the overall efficiency of the LPP. Ideally, this source size is matched to the etendue of the optics, with typical values ranging 1–3.3 mm^2 sr depending on specifics of the lithography apparatus [25, 26].

Plasmas generated by 10 μm lasers require complex tin target preparation and shaping to achieve high CE [19, 24, 26, 57, 58]. Combined with the low wall-plug efficiencies of 10 μm gas lasers, this has motivated research into plasmas driven by shorter wavelength, highly efficient solid-state lasers to strongly accelerate in recent years [22, 23, 27–29, 59, 60]. Radiation-hydrodynamic simulations have shown promise of high CE plasma sources driven by 2-5 μm lasers [24] without the need for complex target shaping. Given the maturity of 1.064 μm solid-state laser technology, and the strong progress in 1.88 μm laser development [29, 60], studies have focused on tin plasmas generated by 1- and 2 μm laser light [23, 59, 61–63]. Relatively low CEs have been recorded for 1 μm plasmas due to re-absorption losses in dense plasma media [22, 28], given the relation $n \sim \lambda^{-2}$ between drive laser wavelength λ and n, the critical plasma density [8]. Consistently twofold higher CEs have been found using 2 μm laser light, under otherwise comparable conditions [22, 27, 28]. However, the experiments using focused 2 μm light did not yield CE values competitive with the CO_2 state-of-the-art, with maximum CEs being limited to approximately 3% – and no information on 2 μm-driven source size is currently available. It was hypothesized [27, 51, 64] that CE values could increase significantly if the plasma is heated homogeneously, i.e. in a manner that is constant spatially and temporally to generate a uniform (optimum) temperature plasma. However, no direct experimental evidence for the 2 μm case is yet available.

In this chapter, we present high-efficiency operation of 2 μm laser-produced plasmas, achieving up to CE = 5% using a simple two-pulse scheme. We demonstrate that the optimization of the laser's temporal and spatial profiles, as enabled by our recent laser development [32], allows for future, high-performance EUV sources powered by 2 μm laser technology. Scaling to high (up to 12.5 mJ) EUV pulse energies is demonstrated while maintaining a small emission size.

2.2 Experimental Setup

In our experiments, tin microdroplets are generated by streaming liquid tin through a nozzle within a vacuum chamber held at 10^{-6} mbar. A low energy 1 μm wavelength 'pre-pulse' laser preshapes the tin droplet into a flat target [8, 10, 27]. A second, high energy, 2 μm 'main-pulse' laser is later fired onto the tin target, generating an EUV emitting plasma [27, 32]. We control the target diameter ($Ø_T$) impacted by the main-pulse by varying the delay time between pre-pulse and main-pulse, allowing for larger targets at longer delays. A schematic of the setup is shown in Fig. 2.1(a). The 2 μm main-pulse used in this work is an in-house-built master oscillator power amplifier system (10 Hz repetition rate) as described in our recent

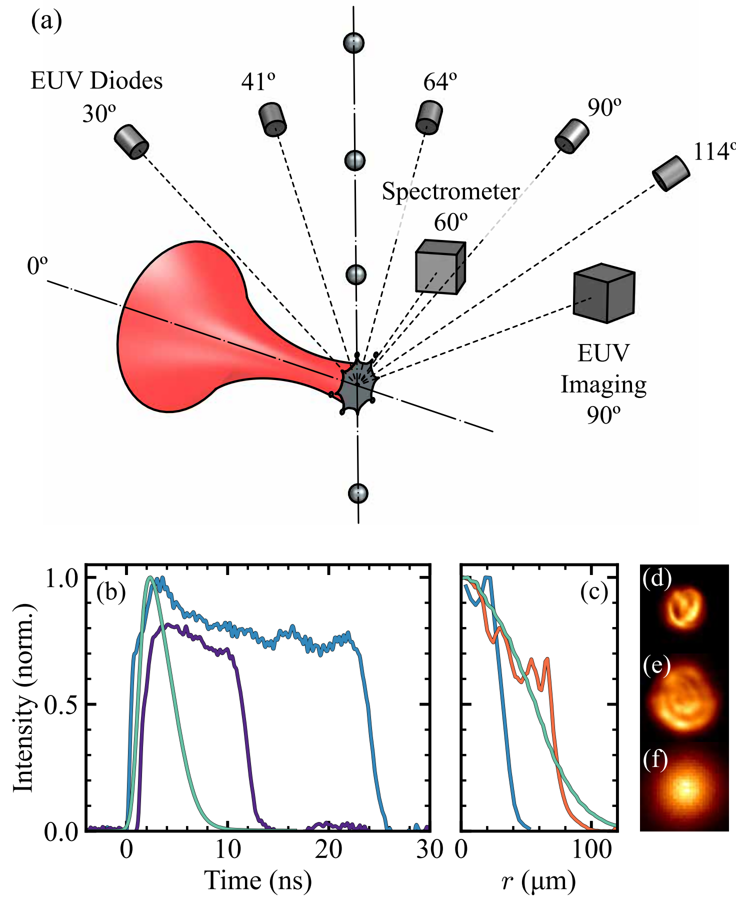

FIGURE 2.1: (a) Overview of experimental setup showing 2 μm main-pulse impacting preformed tin targets. Five diodes are placed at angles 30, 41, 64, 90, and 114° with respect to the laser axis. EUV spectra are measured using a transmission grating spectrometer positioned at 60°. EUV emission profiles are imaged using a concave multi-layer mirror imaging system at 90°. For three different main-pulse diameter cases of 67 μm flat-top (●), 144 μm flat-top (●), and 120 μm Gaussian (●) we show (b) laser temporal profiles where a shorter pulse duration 67 μm flat-top (●) case is also presented, and (c) angularly averaged laser radial profiles and (d), (e), (f) showing the respective spatial intensity profiles.

work [32]. The laser temporal profile is shaped into a uniform 'box-shape' intensity as shown in Fig. 2.1(b). We control the pulse duration and vary it in the range 10-32 ns using a series of Pockels cells. We similarly control the spatial profile by scanning along the propagation of the laser beam and implementing various imaging configurations. The spatial radial average of the beam profile at the tin target is shown in Fig. 2.1(c) for two flat-top beam diameters of 67 μm and 144 μm. Shown also in Fig. 2.1(b) and (c) are the Gaussian beam profiles as studied in previous work [22], to be compared to the here-studied flat-top cases. The spatial profiles are shown in detail in Fig. 2.1(d), (e) and (f) for the 67 μm flat-top, 144 μm flat-top and 120 μm Gaussian beam, respectively.

To study the in-band emission, we place calibrated, EUV-sensitive photodiodes at angles 30, 41, 64, 90, and 114° with respect to the laser axis as shown in Fig. 2.1(a).

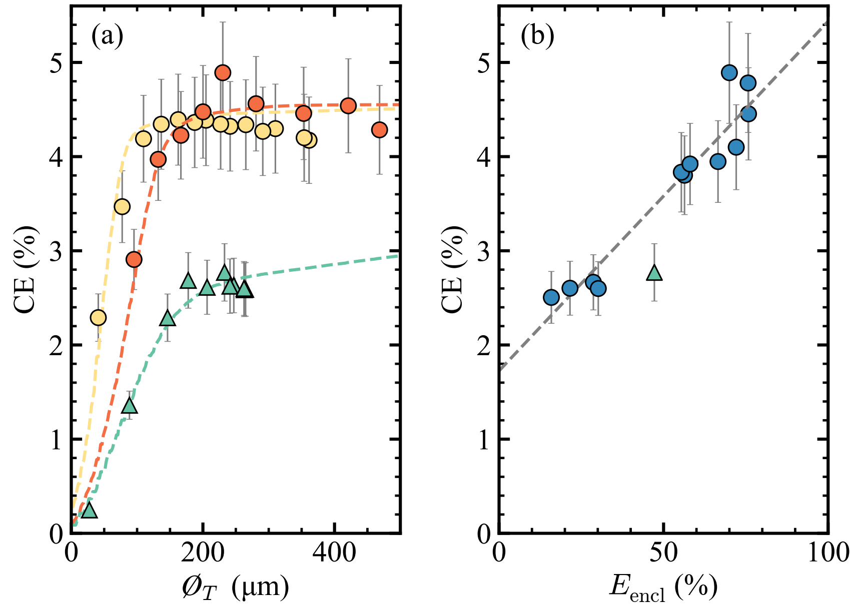

FIGURE 2.2: (a) Scaling of CE with tin target diameter for three different main-pulse laser cases of 67 µm flat-top (○), 144 µm flat-top (●) and 120 µm Gaussian (▲). The dashed lines indicate the fit of the geometrical overlap of the beam and target areas. (b) Scaling of CE with energy enclosed within the flat-top (●) main-pulse beam's spatial FWHM. The dashed line is a trendline fit to the data.

The combined measurement of the EUV photodiodes results in the anisotropy corrected absolute total emission of EUV light. The conversion efficiency of laser light energy into 13.5 nm light emitted in the hemisphere towards the laser is calculated accordingly. The uncertainty in the CE value is calculated considering the uncertainties in the laser energy measurement (2%), calibrating the EUV photodiodes (6%), and the anisotropic fit used to extract the emission fraction into 2π (9% systematic uncertainty), as well as accounting for statistical errors. We study emission spectra in the range 5.5–25 nm using a transmission grating spectrometer which we orient at 60° (cf. Bouza et al. [37]). We additionally investigate the source emission area by acquiring images of the 13.5±1% nm emission using a concave multilayer Mo/Si mirror in combination with an EUV-sensitive CCD (Greateyes BI UV1). This EUV imaging system is placed at 90°. Data presented are averages of 100–200 laser shots.

2.3 Conversion Efficiency

We observe an increasing CE for increasing target diameters for three main-pulse cases as shown in Fig. 2.2(a). The dashed lines are based on a CE scaling with the geometrical overlap of the main-pulse laser spatial profile [taken from Fig. 2.1(c)] with the tin target for the three cases, with the amplitude as a free fit parameter following the approach of Schupp et al. [22]. We offset the geometrical overlap function along the x-axis by a common 21 µm [number taken from Fig. 2.4(c), consistent with simulations [24]] to account for plasma expansion, which enlarges the area where the beam is absorbed [24, 27] for pulse durations beyond several ns [9, 22]. These simple model curves closely match the experimental data. For the flat-top cases, the CE plateaus but at target diameters larger than the beam, as may be expected given that part of the laser energy is situated outside of the area set by the flat-top

diameter. Fig. 2.2(a) shows that flat-top pulses result in higher conversion efficiencies than the Gaussian one. This difference is attributed to the uniform heating of the LPP, resulting in a uniform temperature and emission within the 13.5 nm band across the plasma. Non-uniform illumination may overheat and underheat areas of the plasma, resulting in unwanted out-of-band emission [65]. Underheated plasma regions may moreover lead to additional self-absorption [28, 65, 66]. We note that there is no difference in the maximum obtained CE comparing the 67 and 144 µm flat-top cases. Schupp et al. [51] found that enlarging beam size negatively impacted CE when using 1 µm drive laser pulse due to increasing optical depth, in contrast with the current findings. This contrast is indicative of the lower plasma densities, and optical depth, of the 2 µm case leading to less self-absorption of the produced EUV light [28].

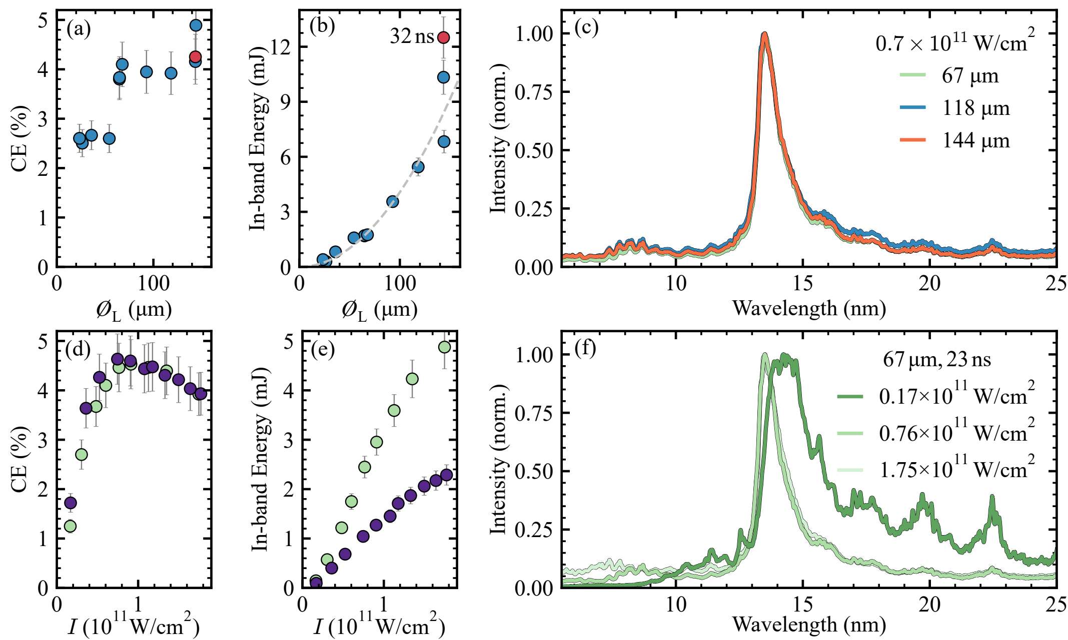

FIGURE 2.3: Scaling of emitted EUV energy for tin targets that are much larger than the beam size. (a) The CE obtained for different laser beam spot sizes for 23 ns (●) and 32 ns (●) pulse durations. (b) The total emitted in-band EUV energy, in the hemisphere towards the laser, of the LPP as a function of the laser spot size. The gray dashed line indicates the $\sim Ø_L^2$ scaling (see main text). (c) EUV spectra in the range 5.5-25 nm for three different laser spot sizes under optimum intensity. (d) CE as a function of laser intensity for two pulse durations: 11 (●) and 23 ns (●) for a 67 µm beam diameter. (e) Total in-band energy for the two pulse duration cases under different illumination intensities. (f) EUV spectra for the 23 ns pulse duration case for three different laser intensities.

Having understood the difference in obtainable CE between flat-top and Gaussian pulses in terms of illumination homogeneity, we next study the influence of beam intensity uniformity on the maximum CE. As a simple metric of uniformity, we use the energy enclosed within the 50% intensity contour of the spatial beam profile, denoted E_{encl}. Fig. 2.2(b) shows optimal CEs under various E_{encl} illumination cases, maintaining constant average intensity as is verified by comparing the emission spectra [27]. The movement of the laser focusing lens enables scaling the beam spot size, moving from near-focusing conditions to and beyond the image plane [beam

spot sizes can be found in Fig. 2.3(a,b)] We observe a clear upward trend of CE with E_{encl} indicating CE values beyond 5% may be achieved for perfectly uniform illumination. The highest conversion efficiency we observed within the studies contained in this paper is $5.0 \pm 0.6\%$ when optimizing all parameters at optimum beam quality. We note that the Gaussian pulse case ($E_{\text{encl}} = 50\%$) undershoots the trend as expected from the aforementioned over- and underheating associated with the Gaussian profile, leading to significant self-absorption and out-of-band reemission [28].

2.4 Energy Scaling

Having achieved CE values competitive with state-of-the-art CO_2-laser-driven industrial EUV light sources [19, 20], we next focus on scaling towards higher EUV pulse energies while maintaining high CE. For nanolithographic applications, EUV emitting plasmas typically emit several 10 mJ of in-band radiation [19, 20]. To achieve similar emission energies, we investigate the output EUV energy scaling with respect to three laser parameters: spot diameter on tin target (Ø_L), intensity (I), and pulse duration (τ_L). Target size is maintained much larger than the beam size, guaranteeing complete geometric overlap. In Fig. 2.3(a) and (b) we show the scaling of CE and forward emitted in-band energy with laser spot diameter, respectively, for a 23 ns main-pulse duration. The spot diameters are averaged over the major and minor axes of the 50% intensity contour. The CE is observed to increase at laser diameters of ∼70 μm which is a reflection of the higher enclosed energies of the larger beams close to the imaging plane. Experimental beam quality limitations result in different E_{encl} for smaller beams and a resulting lower CE as previously discussed. The in-band energy emission scales approximately with the illumination area, i.e. as $\sim\text{Ø}_L^2$, reaching a value of 12.5 mJ for a 32 ns with 144 μm diameter. The spectra for three different beam diameters of 23 ns flat-top illumination at optimum intensity are shown in Fig. 2.3(c). We observe only minute differences in the spectra, which implies similar plasma opacity profiles and underlying plasma conditions such as temperature and density. This similarity in spectral emission across larger beam sizes is a result of optically thin plasma generation by 2 μm laser systems [28] and allows for scaling the beam size without a loss in CE in this range.

In Fig. 2.3(d), the variation of CE with laser intensity is shown for two pulse duration cases of 11 and 23 ns, employing a 67 μm diameter beam. The two pulse durations result in a similar CE profile across a range of intensities, with their optimum at $0.7 \times 10^{11}\,\text{W/cm}^2$. This value matches similarly established optimum intensities for solid and liquid tin targets [27, 28]. We note the slow decrease of CE with increasing laser intensity due to the slowly varying charge state with increasing temperature [67]. Such dependencies further allow for increasing in-band energy by increasing laser energy without significantly reducing CE. This possibility matches simulations under simplified conditions (without considering e.g. target preshaping) in previous work [24]. The scaling of the in-band energy with laser intensity is shown in Fig. 2.3(e). It is immediately clear that given the similarity in CEs in Fig. 2.3(d), the in-band energy scales linearly with laser pulse duration. Laser intensity changes lead to differences in emission spectra as shown for underheated, optimally heated, and overheated plasmas in Fig. 2.3(f). Although lower-than-optimum intensities underheating the tin plasma result in a broad spectrum, we observe but small differences between the optimum and overheated spectra around the 13.5 nm regime. Major differences are only observed in the 6–10 nm range, which reflects

information on the plasma ionic charge state composition and correspondingly, the plasma temperature [68].

We have thus created efficient, high energy, EUV emitting plasmas driven by 2 µm laser light and investigated potential for further scaling of in-band energies. With careful control of the tin target, larger uniform-intensity laser profiles coupled with longer pulse durations and higher intensities, within the studied range, would provide even higher in-band energy emissions at high efficiency to power the nanolithographic process.

2.5 EUV Source Size

Given the importance of the emission source size for the lithographic process, we next study the source size in the radial ($\hat{r}$) and propagation directions ($\hat{z}$) of the laser beam as a result of scaling the in-band energy. For this purpose, images of the EUV emitting area are acquired at 90° [see Fig. 2.1(a)] and shown in Fig. 2.4(a) for a high CE case of a 67 µm diameter beam at optimum intensity with tin targets larger that the beam. The main-pulse laser propagates from left to right impacting the target (not visible). Similarly, for a high in-band energy emitting source (32 ns, 144 µm), an image of the significantly larger EUV emission area is shown in Fig. 2.4(b). In Fig. 2.4(c), we systematically study the source size as determined from its full width at 20% of maximum intensity along each ($\hat{r}, \hat{z}$) axis independently using the same data underlying Fig. 2.3. The 20% contour is chosen such that all reported sizes enclose a significant (>75%) fraction of the total emission energy. As expected, we observe that the source diameter increases with increasing laser spot size [64]. The gray line represents a linear fit to the data trend, with an offset of 21 µm attributed to plasma expansion. The trend indicates a scale invariance of the emission, with a slope (of approximately 2.8×) attributed to the fact that (i) plasma is heated (through conduction but mostly via radiation transport [24]) well outside the laser absorption area and that (ii) significant laser energy is deposited outside [cf. Fig. 2.2(b)] of the area defining E_{encl} while (iii) the definitions of size of the (x, y) axes strongly differ – reducing the $\varnothing_{EUV}$ threshold to 50% is in fact found to reduce the fit slope to 1.5–2. Related to the above argument (ii), we indeed observe a notable downward deviation from the trend for the optimum CE case, due to a high E_{encl} reducing the energy deposited outside $\varnothing_L$. Here we find that maximizing CE through E_{encl} goes hand-in-hand with reducing emission source size.

We further examine the source size dependency on drive laser intensity for a spot size of 67 µm in Fig. 2.4(d). Higher intensities are observed to generate larger sources, similar to previous work [69], primarily due to higher induced temperatures and charge states within the plasma, and increased plasma expansion rate – pushing the critical surface outward [24]. The EUV emission size correspondingly increases. The observed increase is a complex function incorporating also the dependence of the EUV image on the CE [cf. Fig. 2.3(d)]. The inset to Fig. 2.4(d) shows the varying sizes with laser pulse durations under optimum intensity and beam diameters. We note that there is a much lower sensitivity of the source size with laser pulse duration. In fact, the multiplication $\varnothing_r \times \varnothing_z$, yielding the emission area, is nearly independent of pulse length, allowing longer pulses and, thus, enabling higher in-band energy emission without significantly increasing source size.

All presented source sizes match typically reported etendues [25, 58]. For example, an etendue of 3.3 mm^{2}sr (number taken from Ref. Tolstikhina et al. [25] and

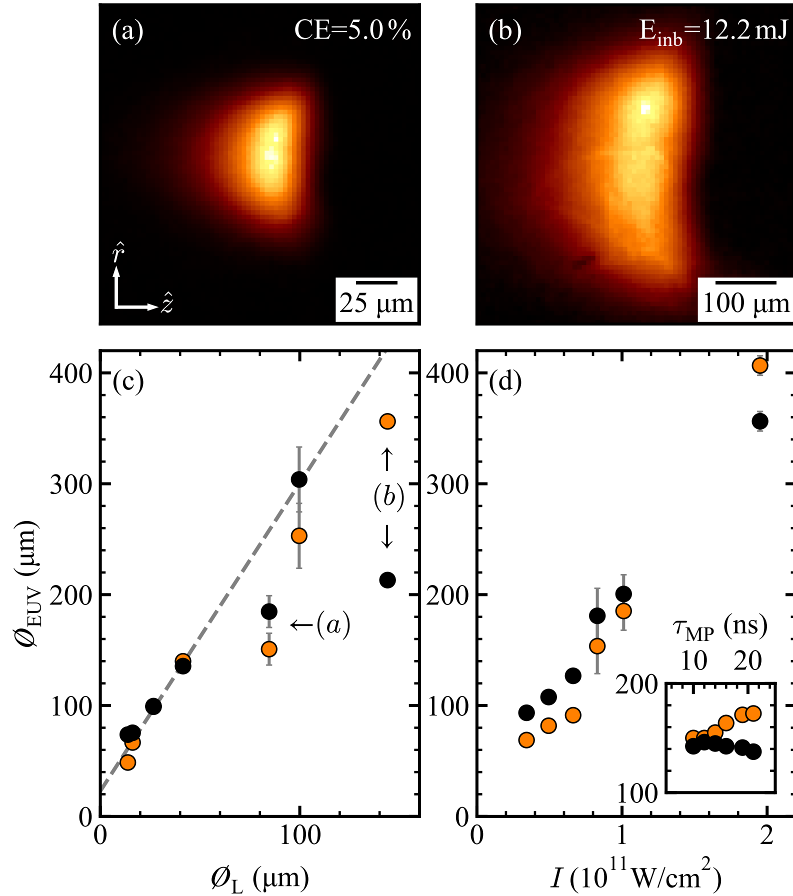

FIGURE 2.4: Scaling of EUV source size (measured at 90°) with laser diameter and intensity. (a) Image of the EUV emission area for a maximum CE= 5.0% case. The laser propagates along the $+\hat{z}$ direction. (b) Image of the EUV emission area for high in-band emission (12.2 mJ). (c) Plasma source size Ø_{EUV} as calculated by its full width at 20% of the maximum intensity along the $\hat{r}$ (●) and $\hat{z}$ (●) directions as a function of laser spot size Ø_L. All data points are acquired at a laser intensity of 0.7×10^{11} W/cm^2. The gray dashed line indicates a trendline fit to the data. Data entries corresponding to the images in panels (a) and (b) are indicated. (d) Source size of a 67 µm laser beam with different intensities in the range 0.3–2×10^{11} W/cm^2. Inset of (d) shows the scaling of source size with pulse duration in the range 10–23 ns. All source sizes above enclose ≥75% of the EUV emission energy.

Fomenkov et al. [26]) for a collector covering 5.5 sr of the forward hemisphere [25, 26], may be efficiently matched to a source size below approximately 600^2 µm^2, assuming isotropic hemispherical emission. Of course, this view represents a strong simplification of the complex beam transport through the optical column through which EUV light is guided onto the wafer.

2.6 Conclusion

In conclusion, we have demonstrated highly efficient in-band EUV production from 2 µm-laser-generated plasma, obtaining a peak 5% conversion efficiency competitive with the industrial CO_2-gas-laser powered state-of-the-art. Combined with the benefits of solid-state laser technology currently under development, in particular with its promise of much larger (up to ∼20%, see Ref. Tamer et al. [29] and Reagan et al. [30]) wall-plug efficiency, and laser pulse energy and power scalability [23, 30], our findings make 2 µm-LPP a particularly promising candidate to power future EUV nanolithography machines. We further show the possibility to scale the extreme ultraviolet light emission towards high energies, by studying output in-band energy scaling with laser spot size, intensity, and pulse duration. High in-band EUV energies of up to 12.5 mJ have been achieved, with scope for further scaling while maintaining small emission source sizes match typical etendues of the EUV optics column. Further studies are required to optimize tin-target delivery, minimizing 'debris' generation [25, 33], including investigating the potential of further simplifying the plasma formation process.

Acknowledgments

We would like to thank Iliya Cerjak and Henk-Jan Boluijt for their work designing the experimental setup and Laurens van Buuren for the aid in assembling the setup and its operation. We would like to further thank Ruben Schupp and Muharrem Bayraktar for their help with the experimental work as well as Lucas Poirier and Michael Purvis for helpful discussions.

Funding

This research was funded by the European Research Council (ERC StG 802648) and the Dutch Research Council (Vidi 15697 and OTP 19458).

Chapter 3

Energy Partitioning of Efficient 2 µm Laser-Produced Plasma Light Sources

The whole is something beside the parts.

Aristotle

We study the energy partitioning of 2 µm laser produced plasmas. By quantifying the photonic and ionic emissions, we can account for up to 99 % of the input laser energy. For plasmas driven under optimum laser intensity, the reconstructed fraction is at 82 % of the input energy. We identify the majority of the emission energy fraction to be in the out-of-band wavelength range. The photonic and ionic emissions are deconstructed into the constituent emission wavelengths and ion charges, respectively. We further study the dependence of the energy partitioning on drive laser intensity and propose several energy channels that may account for the unaccounted energy fraction.

3.1 Introduction

In the previous chapter, we demonstrated high conversion efficiencies of laser light into EUV (13.5 nm$\pm$1%) emissions of up to 5% for the 2 µm laser-driven plasmas. The high conversion efficiency along with the compact emission source size offer 2 µm laser-produced plasma as an attractive alternative to the current 10.6 µm laser systems. Although the high efficiency allows for industrial application use, much is still not understood regarding the energy partitioning and non-in-band EUV emission efficiencies of laser-produced plasma. Particularly, without considering non-EUV emissions, more than 90 % of the input laser energy remains unaccounted. Much of this energy may be channeled into higher wavelength emissions and ion kinetics, both of which influence the operation of industrial EUV sources.

Since the effect of the emitted light on the surrounding optics in an industrial source depends on the emission wavelength, we differentiate the following bands: EUV

A publication manuscript with the contents of this chapter is in the works.

(13.5 nm ± 1 %), sideband (13.2–13.8 nm), out-of-band (5–70 nm excl. sideband), vacuum ultraviolet (70–130 nm) and deep ultraviolet (130–265.5 nm) [70]. While multilayer optics utilized in nanolithography reflect EUV light efficiently, a large fraction of the side-band (SB) emissions are absorbed by the mirror and substrates. The absorbed light contributes to the heating of the mirror, inducing deformities. The out-of-band (OOB) wavelength range may also be absorbed by the mirrors or mirror substrates, affecting the optics' reflection and lifetime [14, 15]. OOB light additionally interacts with the surrounding H_2 buffer gas inducing photoionization ($H_2 \rightarrow H_2^+ + e^-$) and photodissociation. Deep-ultraviolet (DUV) light emitted by the plasma may be reflected by the Mo/Si multilayer mirror and affect the contrast of the exposure on the resist layer further along in the industrial process. Vacuum ultraviolet (VUV) wavelengths are absorbed by H_2 buffer gas causing photodissociation of the molecular hydrogen [71]. The absorption of light (OOB and VUV) by the surrounding gas may result in the generation of secondary hydrogen plasma that may affect the quality and lifetime of the surrounding optics [72].

Previous work by Hemminga et al. [24] has demonstrated the energy partitioning in 2D radiation-hydrodynamic simulations of laser-driven plasma light sources. The work investigates the dependence of the power partitioning on the drive laser wavelength as well as its dependence on the laser intensity for 1 µm wavelength laser-driven sources. The resulting dependencies may provide an essential guide for future light sources, resulting in minimal debris and disadvantageous out-of-band emissions. It is thus interesting to extend this investigation by studying the energy partitioning for experimentally produced plasmas, particularly that of the efficient 2 µm laser-driven plasma.

In this chapter, we aim to observe and study the full emission characteristics of 2 µm laser-driven tin plasma. Accordingly, we need to observe the full light spectrum and ionic emissions. By doing so, we can quantify the fraction of laser light that is channeled into photonic, non-EUV, emission that is not utilized for nanolithography. Longer wavelength emissions may lead to heating of the surrounding industrial system and affect nearby sensitive optics at sufficiently high powers [14, 15]. Thus, longer wavelength emissions are vital to study for EUV light sources in order to obtain a high spectral purity source (ratio of in-band to non-in-band). Similarly, charged tin ions escape the plasma at high velocities. The tin ions interact with surrounding gases and may cause damage to nearby sensitive MLM surfaces [13, 16]. Respectively, understanding the ionic emission fraction and its composition is essential to mitigating charged debris induced damages.

3.2 Experimental Setup

We generate a stream of liquid tin droplets in a vacuum chamber held at $\sim 10^{-6}$ mbar. First, a low-intensity pre-pulse is fired onto 30 µm diameter tin droplets, deforming them into flat sheets (see Introduction). After a certain time delay (0.5 µs), at a sheet diameter of 220 µm, a high energy 2 µm wavelength main pulse impacts the sheet generating the tin plasma. The tin sheet is chosen to have a diameter larger than the laser beam and a large average sheet thickness to prevent low-CE, mass-limited plasma formation (see Chapter 4). While the main pulse intensity profile is uniform temporally and spatially, the intensity I is varied by changing the total energy using a combination of a half-wave plate and a thin film polarizer. Throughout this study,

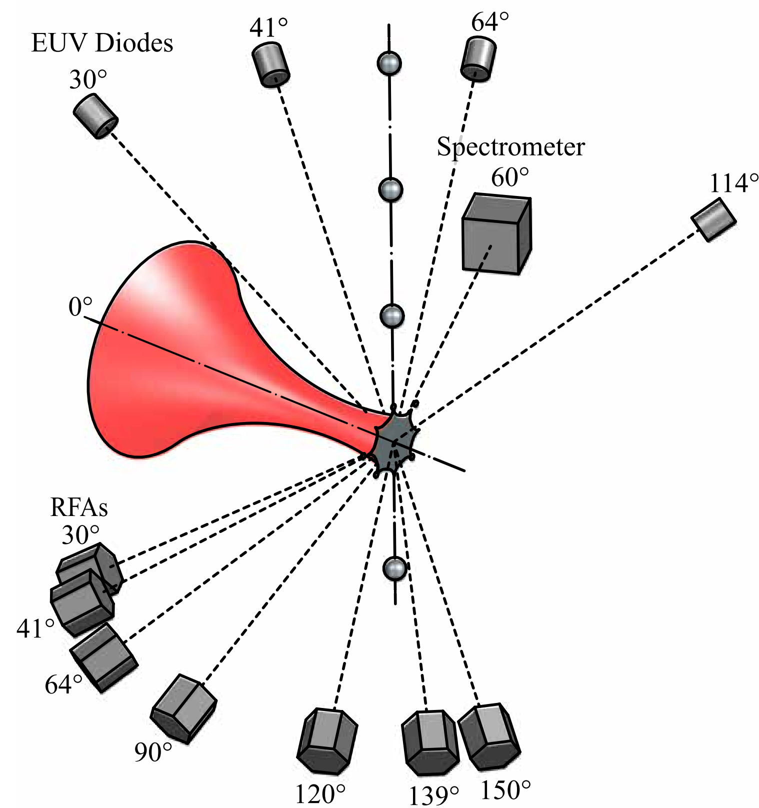

FIGURE 3.1: Schematic overview of the experimental setup showing a preformed tin droplet impacted by a 2 µm laser. Four EUV sensitive photodiodes are places at 30°, 41°, 64° and 114° with respect to the laser axis. A spectrometer active in the range 5.5-265.5 nm is placed at 60°. Additionally, a set of 7 retarding field analyzers (RFA) are placed at 30°, 41°, 64°, 90°, 120°, 139° and 150°. Both EUV detectors and RFAs are distributed around the cylindrically symmetric laser axis, but are shown here to be on one side for simplicity.

the temporal duration of the main pulse is kept at ∼30 ns while the spatial profile has an energy enclosed E_{encl} of 75% (see Chapter 2).

In this chapter, we employ a combination of optical and ionic measurement tools to study the full emission energies of laser-produced plasmas. Four absolutely calibrated in-band photo-detectors are placed at angles 30°, 41°, 64° and 114° with respect to the laser axis as shown in Fig. 3.1. These EUV diodes are designed using a combination of a wavelength selecting Mo/Si multi-layer mirror and an EUV sensitive photodiode. The full spectral range of 5.5–265.5 nm is obtained using a transmission grating spectrometer placed at 60° with respect to the laser. The operation wavelength range of the spectrometer has been previously demonstrated by Bouza et al. [37]. Additionally, a set of seven retarding field energy analyzers (RFAs) are placed at 30°, 41°, 64°, 90°, 120°, 139° and 150° with respect to the laser axis. The operation and response of RFAs has been previously described by Poirier et al. [1].

In the spectrometer [1], light from the plasma source is passed through a filter and a 50 μm slit and subsequently a 1,000 lines/mm grating. Using multiple filter materials, specific wavelength bands are diffracted separately, allowing for the mitigation of higher diffraction orders at a resolution of 0.8 nm at 13.5 nm [37]. The diffracted light is collected on a back-illuminated CCD and spectra obtained using different filters are concatenated, resulting in a higher-order-free total spectrum. The spectrum obtained is then corrected for grating diffraction efficiency and CCD quantum efficiency as well as filter transmission [37]. Another spectrum is measured without filters using a 10,000 lines/mm grating to retrieve a higher resolution measurement (0.11 nm at 13.5 nm [73]) of the 5.5–25.5 nm wavelength regime. Both spectra are cross-calibrated. The corrected total spectrum is integrated in the EUV range and compared to an EUV photodiode placed at a similar angle (64°) to obtain absolute calibration and extrapolate to the 4π emission. Accordingly, we can calculate the emission energy for each observed wavelength. The spectrum is then divided into emission bands and integrated to obtain the energy emitted into each wavelength region.

We [2] analyze the output of the retarding field analyzers to resolve the ions emitted from the plasma as previously studied [1]. The ions emitted by the plasma are detected ∼1 m away using an RFA: a Faraday cup (FC) with retarding and suppressing voltage grids. Using incrementally varying voltages on the retarding grid, lower energy ions are consecutively retarded and not detected by the Faraday-cup. Accordingly, a charge and energy resolved ion spectrum is calculated [1]. The charge-state resolved ion spectra are integrated to obtain the amount of energy carried by each charge state. Additionally, the ionization energy of the detected ions is calculated using the ion count and tabulated ionization energies of tin [74, 75]. Although the calculated ionization energies are that of ions far from the plasma (>200 μm), and higher charge states may have already recombined [76–79], the calculation gives us a lower-bound estimate of the laser energy channeled into ionization.

3.3 Photonic Emissions

In Fig. 3.2(a) we present the emission spectrum in the wavelength range 5.5–265.5 nm for varying main pulse laser intensities in the range $0.9–9.9 \times 10^{10}$ W/cm^2. The laser

[1] The analysis of photonic spectra was aided by Zoi Bouza.
[2] The analysis of the ion energy spectra was executed by Xyoisan Danser and Lucas Poirier.

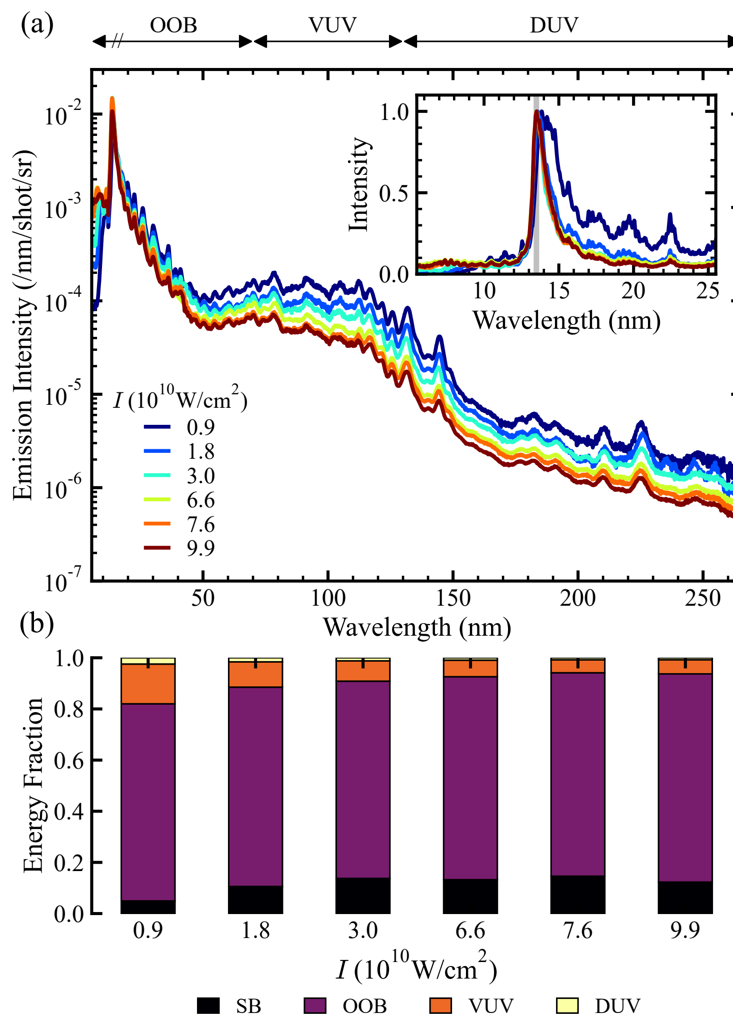

FIGURE 3.2: (a) Emission spectra in the 5–265.5 nm wavelength range of 2 µm laser-produced tin plasma under various laser intensities ranging from 0.9–9.9 $\times 10^{10}$ W/cm^2. The inset shows spectra obtained under the same conditions using a higher resolution grating and normalized by their peak emission. The EUV band is highlighted in gray. (b) Band-resolved emission energy fraction under different laser illumination intensities. The emission is discretized to: sideband (13.2–13.8 nm), out-of-band (5–70 nm excl. sideband), VUV (70–130 nm) and DUV (130–265.5 nm).

intensity range is chosen to cover under- and overheating of the plasma, where optimal heating, in terms of EUV emission efficiency, lies at 7×10^{10} W/cm^2 [28]. The spectra are normalized by the main pulse laser energies to highlight the variation of emission in the wavelength bands, relative to the main emission at 13.5 nm. The inset of Fig. 3.2(a) shows higher resolution spectra for the wavelength range 5.5–25.5 nm obtained with a 10,000 lines/mm grating and normalized by the peak emission at 13.5 nm.

The energy fraction emitted into each wavelength band is shown in Fig. 3.2(b) for each main pulse laser intensity. The fraction of energy of light emitted in each band is normalized by the total detected emission across the full range. The DUV contributions may not be visible in this sub-figure for higher intensities due to the very low fraction of light emitted into this wavelength region.

In Fig. 3.2(a) the spectra demonstrate that for higher driving laser intensities, a higher spectral purity is obtained. Emission contained in the higher wavelength bands decrease with increasing intensity compared to the 13.5 nm peak. The emission energy shifts to lower wavelengths, centered in the EUV band with increasing 5.5–10 nm emission intensities. The inset to Fig. 3.2(a) shows behavior similar to that observed in Fig. 2.3(f). Plasmas driven by lower-than-optimum main pulse intensity have low spectral purity, i.e. they emit across multiple wavelengths, due to underheating of the plasma. Higher intensity driven plasmas demonstrate a high spectral purity with intense emission centered around the 13.5 nm band. The higher main pulse intensity spectra demonstrate limited self-absorption at 13.5 nm compared to the plasma driven by lower main pulse intensities [22].

The sideband emission energy fraction (which includes in-band EUV) shown in Fig. 3.2 behave similar to that previously shown in Fig. 2.3(d), with a maximum emission fraction at the optimum intensity (here at 6.6×10^{10} W/cm^2) and a slow decrease with overheating, at higher intensities. In contrast, the VUV and DUV contributions continuously decrease with increasing intensity and plasma temperature. The largest fraction of energy is emitted in the OOB range, accounting for $\sim$70 % of the total emissions.

The emissions in the OOB 5.5–12 nm range have been previously identified to be primarily due to Sn^{8+}–Sn^{15+} [6, 73] and show an increasing energy fraction with increased drive laser intensity. Similarly, the emission peaks in the 15–40 nm range have been identified to originate from Sn^{4+}–Sn^{10+} [65, 70]. The emissions due to the lower charge state are expected to be less intense in higher temperature, higher average charge-state plasmas as is observed. The out-of-band emission highlighted here contribute the most emission energy as can be seen in the fraction of energy emitted in Fig. 3.2(b). The emission peaks in the 50–150 nm range are yet to be identified but are expected to originate primarily from lower charge states.

There exists uncertainties in the shown spectra and corresponding energy fractions. Due to drive laser instabilities, there exists a drift in the average laser intensity across different filter measurements in the same spectrum. These fluctuations are slightly mitigated by concatenating averaged spectra from each filter measurement. An additional error is due to the corrections applied to the spectra measured, particularly, the filter transmission and CCD quantum efficiency (QE) corrections. Tabulated material transmissions were used to correct for the filter transmissions in this chapter. Depending on the filter thickness, oxide layer formation and debris deposited on the filter, the transmission values and their dependence on wavelength may change. As

discussed by Bouza et al. [37], QE curves, and their effect on the spectrum, differ for different CCDs. We utilize here the QE curves supplied by the manufacturer, while considering the effect on the total spectrum if other QE curves were used instead [80]. Finally, the most significant contribution to the uncertainty in the photonic spectra is due to the assumption that the emission magnitude and anisotropy matches that of in-band EUV (as detected by the diodes). Since the spectrometer is placed at only one angle, and we seek to find the 4π emission characteristics, we assume the anisotropy of the emission at all wavelengths is similar to the in-band EUV emission anisotropy. However, we expect spectral emission anisotropy to match EUV emission anisotropy, where the 64° diode accurately represents the averaged 4π emissions.

We have characterized the photonic emissions in the 5.5–265.5 nm wavelength range from plasma light sources driven by 2 µm laser drivers. We explored the dependence of the emission on the drive laser intensity in a range relevant for nanolithographic applications, particularly around the laser intensity where optimum EUV emission occurs. The emission spectra were analyzed and decomposed into multiple wavelength bands in order to characterize the energy fraction emitted into each band. We were able to find dependencies of the energy fractions on drive laser intensities and identify the major contributors to the uncertainty in the reported values. Based on the sideband emission fraction we conclude that an optimum sideband and EUV emitting plasma is driven by a laser intensity of 6.6-7.6$\times 10^{10}$ W/cm^2. Higher and lower intensities result in photonic emissions of different wavelengths that are not utilized for EUV nanolithography.

3.4 Ionic Emissions

Similar to the photonic emission, we study the charged tin ions emitted from the 2 µm laser-driven plasma as a function of laser intensity. Fig. 3.3(a) shows the energy-resolved charged emissions as detected by the 64° RFA and thus comparable in angle to the spectrometer. The ion emission spectra are shown for driving laser intensities in a range similar to the photonic emission studies of 0.9–10 $\times 10^{10}$ W/cm^2. The spectra shown here are that of FC-like, i.e. no retarding field is applied and thus capturing the total charge. The inset to Fig. 3.3(a) demonstrates the charge resolution as calculated for the 6.6$\times 10^{10}$ W/cm^2 intensity case as previously studied [1, 74]. The charge resolved dQ/dE shows the decomposition including charges up to 6+ based on the optimization of the charge reconstruction method.

We observe a shift in the high energy peak to higher energies with increasing drive laser intensities. The source of this high energy peak is attributed to the ballistic expanding shell of tin ions at early times, as studied by Hemminga et al. [76]. Although the authors note the result is specific to plasma illuminated using a temporally Gaussian pulse [76], we observe the same peak in ion spectra here, using a temporally flat-top profile. The intensity dependent shift of the energy spectra has been studied previously by Poirier et al. [81]. They find a dependence of $E \propto I^{0.67(5)}$ which is very similar to the dependence $E \propto I^{0.7}$ derived from analytical hydrodynamic modeling [9]. Consequently, the origin of the shift is concluded to be due to the increased average plasma temperature which increases the average charge states and kinetic energy. The data shown in Fig. 3.3(a) deviate from this power law particularly at higher drive laser intensities. The dependency found based on this data is $E \propto I^{0.4}$, where the different power, compared to the literature, is attributed to

the flat-top drive laser temporal profile as well as experimental uncertainties in this work.

The charge-state reconstruction calculation is executed for each laser intensity case and the fraction of kinetic energy carried by each charge is shown in Fig. 3.3(b). For each retarding field voltage step, an average is taken of hundreds of laser shots. Accordingly, a statistical uncertainty is introduced that is based on the stability of the drive laser system. The ion energies shown are normalized by the total kinetic energy of all ionic emissions. Charges of up to Sn^{8+} are identified for the highest driving laser intensities. Based on the knowledge of the number and charge of the constituent charge states shown in Fig. 3.3(b), the total ionization energy is calculated.

We detect higher charge states from plasmas driven using higher laser intensities. This matches the expectation laid out by the atomic kinetics model of an increased plasma temperature and accordingly average charge state $\bar{z} \propto T^{0.60}$ [9].

We note that plasmas generated in this study are driven by laser intensities near that of optimum EUV emission, resulting in the generation of charges of Sn^{10+}-Sn^{14+} in the plasma [6, 7]. As the plasma expands into vacuum, the charged tin ions recombine (primarily dielectronic recombination) into lower charge states [77, 78]. Consequently, at ∼1 m away from the plasma, we may only detect the recombined tin ions, and thus only measure lower charge states of up to 8+.

In order to estimate the uncertainty in the calculated ion kinetic energies, we employ the model of the average charge state at each energy $\bar{z}(E)$ [79]. Sheil et al. [79] find a universal power-law dependence of the average detected charge state and its energy. The resulting power-law is found to be independent of plasma parameters, e.g. independent of drive laser intensity. According to the estimation provided by this model, we avoid the dependence on systematic effects of the charge reconstruction method. The expectation value for the total kinetic energy of the detected ions is

$$< E_{kin} >= \frac{\int_0^\infty \frac{dN}{dE} E dE}{\int_0^\infty \frac{dN}{dE} dE}, \tag{3.1}$$

where the number of ions N at each energy is calculated by

$$\frac{dN}{dE} = \frac{\frac{dQ}{dE}}{e\bar{z}(E)}, \tag{3.2}$$

where e denotes the elementary electron charge. Following Sheil et al. [79] and Poirier [82], we find an average prediction for the global estimate of the average charge state $\bar{z}(E) = 0.3E^{0.4}$ and Eq. 3.2 results in

$$\frac{dN}{dE} = 2.39 \times 10^{19} \frac{dQ}{dE} E^{-0.4} \tag{3.3}$$

By using Eq. 3.3 in Eq. 3.1, we find the expected value for the total kinetic energy of the detected ions. For our data near the optimum EUV emission intensity, $I = 6.6 \times 10^{10}$ W/cm^2, the charge-reconstructed total ion kinetic energy was calculated

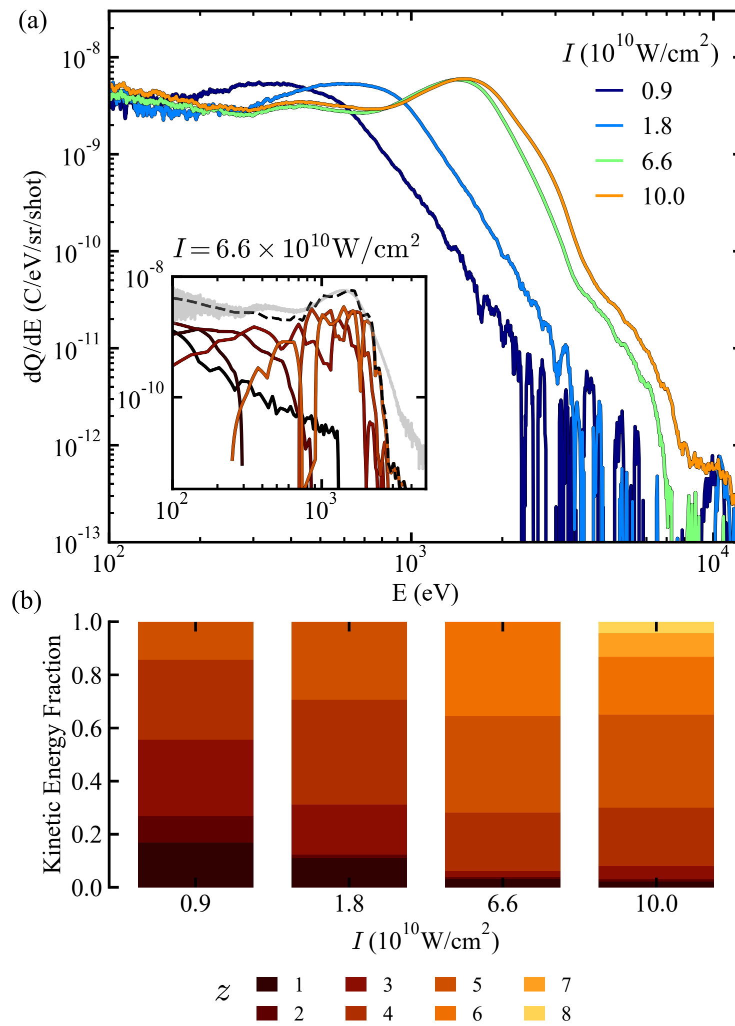

FIGURE 3.3: (a) Ion kinetic energy charge-spectra for four different main pulse average intensities in the range 0.9–10 $\times 10^{10}$ W/cm^2. The inset shows the charge resolved spectrum for $I = 6.6 \times 10^{10}$ W/cm^2. The dashed black line shows the sum of all calculated charge states and the gray line shows the Faraday-cup-like spectrum, similar to the green line. (b) Fraction of kinetic energy carried by each charge state z for each laser intensity as calculated using the retarding field charge-state resolution method [1].

to be 13.9 mJ. With the average charge state per energy assumption employed above, the total kinetic energy is calculated to be 14.6 mJ. This minor difference may be attributed to the lower quality calculation of the charge reconstruction, which is shown to deviate from the FC-like measurements in the inset of Fig. 3.3(a), specifically at higher energies. The lower quality reconstruction of the method is primarily due to laser instabilities. As mentioned above, since an average is taken of many laser shots and due to the long time to acquire such signals, drifts in the laser alignment, beam quality and average intensity all occur. This results in the production of plasmas with slightly different emission characteristics and thus the reconstruction, which assumes identical emissions across all retarding field values, is impaired. Insufficient retarding grid voltage steps may also contribute to the inaccuracies.

We have thus investigated the ionic emissions and decomposed the energy fraction into each detected charge state for plasmas relevant for nanolithographic applications. Particularly, we have revealed the dependence of the ionic emissions on the drive laser intensity of a 2 µm wavelength driver in the wavelength range that is optimum for in-band EUV emission. We have demonstrated the dependence on the emission spectra on intensity, showing increasing ion energy with laser intensity. Following the charge state reconstructions, we identified the charge states carrying the majority of the energy to be Sn^{1+}–Sn^{6+} as detected far from the plasma. This enables the choice of suitable mitigation techniques such as deflecting magnetic fields or the introduction of an ion stopping gas. The choices for the magnetic field strength and stopping gas pressure depend on the needed stopping power, and thus the ion studies shown provides the needed input. Since we study a drive laser intensity range similar to the photonic study, we can thus combine the results to estimate the total energy partitioning of 2 µm wavelength laser driven plasmas.

3.5 Energy Balance

Combining the results from the transmission grating spectrometer and the angularly resolved RFAs, we can investigate the energy partitioning of the generated plasma. The fraction of energy emitted into each channel is shown in Fig. 3.4(a) for different driving laser intensities. From the spectrometer, energy partitioning into the different wavelength bands is shown, where the emission anisotropy is assumed to be similar to that detected by the EUV photodiodes. Similarly, from the RFAs, the 4π angular corrected ion emission and potential energies are shown for different main pulse intensities.

The origin of uncertainties in the measurements shown have been discussed in the previous two sections for the photonic and ionic emissions. The error in the combined sum is calculated based on the quadratic sum of the two emission components. Accordingly, the total reconstructed energy and the uncertainty in its value can be compared to the measured input energy of the 2 µm wavelength drive laser.

A large uncertainty is due to the estimated laser beam transmission through the vacuum window. The transmission of the 2 µm wavelength light varies across our measurements. The measurements were executed consecutively, with the transmission decreasing gradually due to deposited tin on the inside facing side of the window. We tackle this issue by measuring the transmission before the experiments run, i.e. before vacuum is achieved, by comparing the laser energy before and after the window. We additionally do the same calibration after the experiments have concluded. Furthermore, we regularly estimate the laser transmission during the experiments

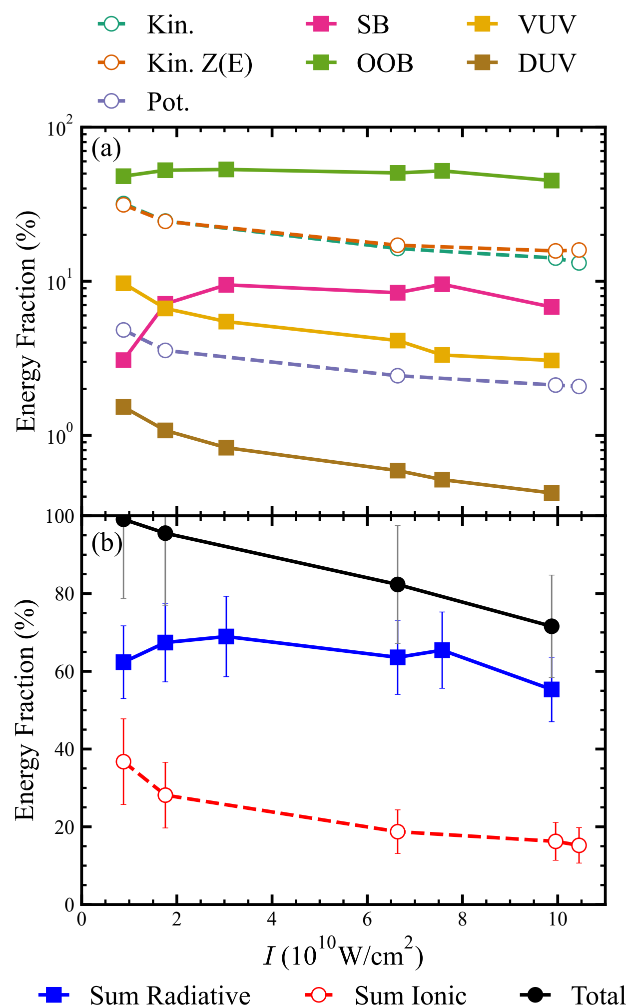

FIGURE 3.4: Intensity dependence of the power partitioning of emissions from 2 µm laser-driven plasma.(a) The reconstructed kinetic (Kin.) and ionization energy (Pot.) of ionic emissions as well as the calculated kinetic energy (Kin. $z(E)$) based on the universal power law assumption. Photonic emissions of sideband (SB), Out-of-band (OOB), vacuum ultraviolet (VUV) and deep ultraviolet (DUV) photonic emissions are similarly demonstrated. (b) The sum of ionic energies and sum of radiative emissions as well as the total reconstructed energy fraction from the plasma.

by observing the CE while varying the laser intensity. In such a scan, the highest CE is known to be at a known laser intensity ($I = 6.6 \times 10^{10}$ W/cm^2) and thus the decrease in transmission can be calculated by noting the increase in laser energy at which the highest CE occurs. A (Beer–Lambert law) transmission curve is fitted assuming a constant optical density and increasing thickness of the deposited tin layer. Accordingly, the transmission of the 2 μm laser light is interpolated, and the energy of the laser beam impacting the target is calculated.

While most energy channels shown in Fig. 3.4(a) decrease with increasing intensity, the SB and OOB emissions exhibit a peak of emission around the optimum intensity (similar to CE dependence on intensity shown in Chapter 2). For both wavelength bands, this peak is attributed to the generation of charge states which contribute to the emission in these wavelength regions. Many of these higher charge states have been previously identified as mentioned above. Underheating and overheating the plasma light source generates lower and higher charge state, respectively, compared to the Sn^{10+}–Sn^{14+} which emit in the SB. For the higher wavelength bands, VUV and DUV, an optimum emission laser intensity would be at much lower intensities than studied here, since it is primarily lower charge states which emit at these wavelengths.

The total energies measured using the spectrometer and RFAs, and their sum are shown in Fig. 3.4(b) for the intensity range studied. At low intensities, around 99 % of the laser energy is accounted for. We observe that the total reconstructed energy decreases with increasing laser intensities. This results from both decreasing ion energy fraction and photonic energy emissions. There are other energy channels not accounted for in this work, which may have an increasing energy fraction with laser intensity. For example, the fraction of escaped (transmitted or reflected) laser light may increase for higher intensities. However, we predict the fraction of escaped laser light to be minor. Based on the EUV and ionic emission anisotropy we can confidently conclude the plasmas formed in this chapter are not mass-limited and do not exhibit burn-through of the laser. In addition to the fact that the tin targets all have larger diameters than the main pulse laser beam, i.e. full geometrical overlap, we predict there is little to no laser light to be measured in the backwards side of the setup. Another possibility for the increasing missing energy fraction is the kinetic energy deposited into neutral debris, i.e. neutral tin vapor and nano-clusters. Such debris is imaged using shadowgraphy techniques and can be shown to have high velocities, and thus high energy, but the discussion of this contribution lies beyond the scope of this study.

The experimental study of the intensity dependent energy fractions shown in this work is similar to the simulation work of Hemminga et al. [24] for plasmas formed from tin droplets. They simulate the dependence of the power fraction for different laser intensities of a 1 μm wavelength laser driven source in the intensity range around the optimum intensity (which is 1.4×10^{11} W/cm^2 for a 1 μm driven plasma). The simulation results show relatively independent kinetic and radiative power fractions with increasing intensity. There is minor change in the fractions around the optimum laser intensity where the kinetic power is shown to be minimal, in contrast to the radiative power which is maximal at this laser intensity. However, these dependencies are very minor and are very difficult to see for the simulated work. Comparatively, for the ionic kinetic energy observed in this work (to be compared to P_{kin} [24]), we observe a large dependence of the ion kinetic energy fraction. This

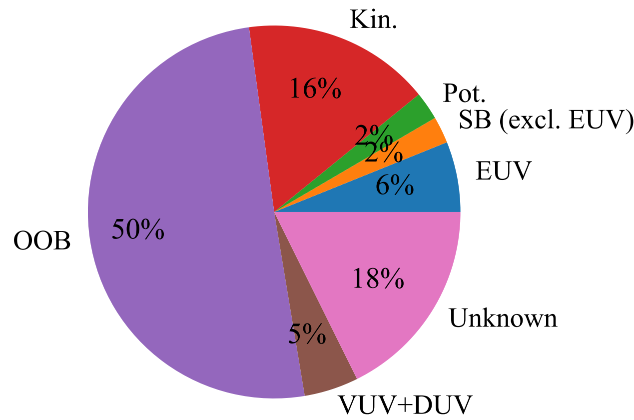

FIGURE 3.5: Energy partitioning of 4π emission from 2 µm laser-produced plasma. Laser intensity is maintained at 6.6×10^{10} W/cm^2 which is optimal for EUV emission. Fraction of the total input laser energy is shown for out-of-band (OOB) radiation, ionic kinetic energy (Kin.), EUV emission, summed VUV and DUV emission energies, ionization energy (Pot.), sideband emission (SB, excluding EUV) and the remaining energy fraction (Unknown) compared to the main pulse laser energy.

difference is attributed primarily to the inaccuracies of our measurements reconstructing highly energetic ions or the difference in target morphology, and not to the different driving laser wavelength. For the photonic emissions, we see similar dependence of the side-band emissions (to be compared to CE_p [24]) where there is a maximum fraction at the optimum intensity. It is interesting to note that Hemminga et al. [24] find an increasing fraction of reflected laser light (P_{ref}/P_{las}) which, although is maximum at 0.1 %, may be considered for future experiments as the fraction is higher at longer laser wavelengths.

3.6 Optimum Emission Plasma

For the high-CE case achieved with a laser intensity of 6.6×10^{10} W/cm^2, we demonstrate the partitioning of the emissions. The EUV energy detected by the photodiodes, emission spectra measured by the spectrometer, and energy calculated from ionic analysis are summed and compared to the total initial input laser energy of 85 mJ. The fraction of energy output for each emission channel is shown in Fig. 3.5.

We observe highest emission energies in the out-of-band region of wavelengths as detected by the spectrometer. In this case, around 50 % of the energy of the laser is emitted into this wavelength regime. Secondly, around 16 % of the laser energy is carried out by highly energetic charged tin ions. Following that, in-band EUV energy is at 6 %, the sum of VUV and DUV is 5 %, and the ion ionization energy is at 2 %.

There remains a large fraction ~18 % of the laser energy unaccounted for. As discussed above, a part of this remaining 15 mJ could possibly remain as reflected or transmitted laser light. There are other wavelength emissions unaccounted for in

this study (< 5.5 and > 265.5 nm), although we expect the fraction of energy emitted into these bands (ultraviolet-visible) is much lower than that of VUV and DUV. As shown in the inset of Fig. 3.3(a), and as calculated above using the $\bar{z}$ assumption, we predict that we are underestimating the ion kinetic energy and ion count, however, the underestimation seems to be minor. As a result of the underestimated ion count, and due to non-radiative charge recombination events, we further expect the ionization energy calculated to be a lower bound. Finally, since the plasma generated is not mass-optimized, we expect a significant fraction of the energy to be channeled into neutral tin debris.

In future experiments, the uncertainty in the fraction of energy channeled into ionic emissions can be reduced through more thorough retarding voltage scans under stable drive laser conditions. This may result in a more accurate reconstruction of the spectral charge states composition. Additionally, by observing the anisotropic imbalance of ion emission, the kinetic energy of neutral tin particles may be estimated following the work of Poirier [82]. Alternatively, a mass-optimized plasma, with limited excess mass and, thus, limited debris, could be investigated (see Chapter 4).

3.7 Conclusion

In this chapter, we have studied the emission characteristics of 2 μm laser-produced plasma light sources. We have identified the major emission energy channels to be the out-of-band emissions and ion kinetics. We were able to reconstruct up to 82 % of the energy of a high-CE plasma and up to 99 % of low drive laser intensity produced plasma. We have additionally proposed improvements to allow for the measurement of the remaining undetected fraction of the input laser energy.

The dependence of the energy partitioning on the drive laser intensity was shown and compared to previous work on simulated 1 μm wavelength laser driven tin droplets [24]. A (slightly) higher than optimum intensity driven plasma is shown to demonstrate similar ionic and photonic emissions to the plasma driven by a optimum intensity laser while emitting more EUV light due to the increased energy input. This finding, along with the findings of Chapter 2, promote the use of a higher intensity driver for plasma EUV light sources. Based on the knowledge of energy fractions channeled into the major emission channels, mitigation techniques could be developed and optimized. Accordingly, a high efficiency EUV light source could be developed with minimal impact from debris on surrounding sensitive optics and devices.

Chapter 4

Mass Efficient 2 µm Laser Produced Plasma

Physics is the science of matter & energy,
and how they interact.

Phil Berneburg

Using thin tin sheets preformed from a droplet, we investigate the mass-use of 2 µm laser-produced plasmas. We demonstrate a large dependence of the conversion efficiency of the plasma on the tin volume overlapping the laser beam. Mass-limited tin plasmas are described both experimentally and using radiation hydrodynamic simulations. We further show the effect of laser burning through targets of insufficient mass on EUV emission anisotropy and emission surface morphology. The dependence of mass use on laser intensity and pulse duration is demonstrated through observations of time-dependent EUV emission, side-view EUV images, and escaped laser light.

4.1 Introduction

In previous chapters, we demonstrated high-efficiency EUV generation (Chapter 2) with an understanding of the energy partitioning of plasma emissions (Chapter 3) using 2 µm-laser-driven tin plasma. In this chapter, we switch our focus towards the plasma's use of liquid tin and its ablation efficiency. Accordingly, we aim for both energy and mass-efficient laser produced plasma light sources. High mass use efficiency is desirable in a laser produced plasma EUV light source. Excess supplied mass, present in tin droplets or preformed sheets may contribute to debris and sputtering on nearby sensitive optics. With mass-optimized plasma sources, only the mass required to sustain the plasma is supplied, minimizing the amount of debris.

Previous studies have demonstrated the effect of droplet size on the efficiency of 1- and 2-µm laser-driven plasma EUV sources [22, 27]. In such studies, the dependency of the CE on droplet size is shown for non-preformed target experiments and on the sheet diameter for preformed targets. However, no investigation of the dependence of CE on target thickness, or the amount of mass overlapping the laser beam was yet performed. The prior studies did not extend to the range of droplet sizes such that mass-limited behavior is investigated. In order to understand the mass use rate

A publication manuscript with the contents of this chapter is in the works.

(mass use per nanosecond exposure of by the main-pulse) and to obtain a mass-optimized plasma, we aim to span this study to investigate the full range of mass overlap with the laser beam. Previous studies [31] have investigated the mass use rate and its dependence on laser wavelength and intensity for solid tin targets and laser wavelengths other than 2 µm. We aim to expand on this research by examining preformed liquid tin droplets under conditions relevant for EUV nanolithography.

In this chapter, we demonstrate the mass use efficiency of 2-µm-wavelength-laser-produced plasma and highlight its dependency on target thickness overlapping the laser beam. We show mass-limited laser-produced plasmas which exhibit low energy efficiency due to mass deficit. The key parameter is found to be the liquid volume overlapping the laser beam, a clear predictor of mass use efficiency. As previously investigated [9, 31], we further demonstrate a dependence of the mass use on laser intensity and pulse duration.

4.2 Experimental Methods

We employ an experimental setup similar to the last two chapters to study the mass use in 2 µm laser-driven tin plasmas. In a vacuum chamber maintained at $\sim 10^{-6}$ mbar, we stream droplets of liquid tin through a nozzle. The tin droplets are varied in diameter by controlling the volumetric flow rate and applying sinusoidal oscillations on the nozzle. The resulting liquid stream is broken into droplets of consistent diameter [83]. Measurements of the droplet sizes are based on magnified shadowgraphy images of the droplet stream at the point of laser impact [10].

First, a low-energy 1 µm wavelength pre-pulse laser is fired onto a tin droplet inducing a hydrodynamic deformation similar to the previous chapters [10, 12]. We use different pre-pulse laser energies E_p fired onto different diameters of tin droplets D_0 and change the pre-pulse to main-pulse delay time. This variation in D_0, E_p and delay results in tin sheets with various thicknesses and diameters [10, 12] as shown in Fig. 4.1(a)&(b). After the predetermined delay, a spatially and temporally flat-top 2 µm laser beam with energy enclosed within the FWHM of the spatial profile E_encl of 75% (see Chapter 2) is fired onto the tin sheet generating the plasma.

The liquid tin target preparation is described in Fig. 4.1. An example of the droplet deformation into a thin sheet is shown in Fig. 4.1(a). After the pre-pulse laser impact, the droplet expands radially and is propelled in the direction of the beam. At the hydrodynamic apex time t_apex, the sheet retracts due to the surface tension of the liquid [10, 12, 84]. Late-time sheets may have the same diameter as early-time sheets, but will be thinner due to the mass loss during the expansion, and retraction processes [12]. In Fig. 4.1(b), the expansion and retraction trajectories of all initial droplet size and pre-pulse energy combinations used in this study are shown as a function of time after pre-pulse impact.

The choice of a main-pulse with a flat spatial profile is motivated as follows. First, we aim to generate and study higher-CE plasmas driven by 2 µm laser light, relevant for EUV nanolithography; the highest CE values are obtained with flat-top profiles cf. Chapter 2. Second, a uniform intensity illumination of the tin sheet results in uniform laser ablation characteristics. A varying intensity profile will have varying ablation rates [9, 31], resulting in different mass usage across the tin sheet, which would hamper the interpretation of our experiments. The tin sheet varies in thickness [12], which may result in different dynamics of the mass use across the sheet. A

spatio-temporally uniform intensity laser would allow us to observe the dynamics with respect to the average sheet thickness overlapping the laser beam.

The generated tin plasma is studied using four EUV-detecting photodiodes (see Chapter 3) placed at varying angles with respect to the laser. The EUV emitting surface, and source size, are captured using the EUV imaging system similar to Chapter 2 placed at 90°. We additionally place two time-resolved EUV-sensitive photodiodes at angles 21° (forward) and 159° (backward) with respect to the laser propagation axis. These two photodiodes allow us to observe the time-dependent EUV emission and, thus, we may infer some dynamics of the observed plasma.

The main-pulse laser energy is measured before the pulse is directed into the vacuum chamber and is corrected for transmission through the vacuum window. We measure the transmission of the vacuum window before and after the experimental studies and interpolate the transmission drop using an exponential function. This interpolation assumes a constant tin deposition rate per laser shot onto the window. Based on intermediate measurements of intensity dependence of the CE, we re-calibrate the required input energy to account for the decreased transmission. This correction has been discussed in more detail in Chapter 3. The temporal profile of the laser pulse is measured before the vacuum chamber using fast photodiodes paired with a 2 µm wavelength band-pass filter. At the vacuum chamber exit, we additionally measure the escaped laser light in a similar manner, using a wavelength-selecting filter and a fast photodiode aimed at a beam dump. Due to the high NA of the laser imaging system, some laser light is clipped at the exit by the vacuum windows. Accordingly, the spatial edges of the laser beam could not be detected but we expect little variation of the temporal profile across the spatial domain.

Overlap Mass

The tin mass ($\tilde{m}$) overlapping the flat-top main-pulse laser beam (with diameter $\varnothing_L$) is calculated as

$$\tilde{m} = \rho \int_{\varnothing_L} V \, dV. \tag{4.1}$$

Here, the tin volume enclosed within the sheet (V_{sheet}) is calculated as [12]

$$V_{\text{sheet}} = \int_{R_0}^{R(t)} 2\pi r h(r,t) \, dr, \tag{4.2}$$

where r denotes the radial coordinate along the sheet and t the expansion time. In our experiments, the expansion time is the time delay between the pre-pulse and the main-pulse laser beams. The sheet thickness profile is given by h as [12]

$$h(r,t) = \frac{D_0^3}{a_0 u_0^2 t^2 + a_1 u_0 t r + a_2 r^2}, \tag{4.3}$$

or at later times as [85]

$$h(r,t) \approx \frac{V_0}{u_0 r t}, \tag{4.4}$$

4

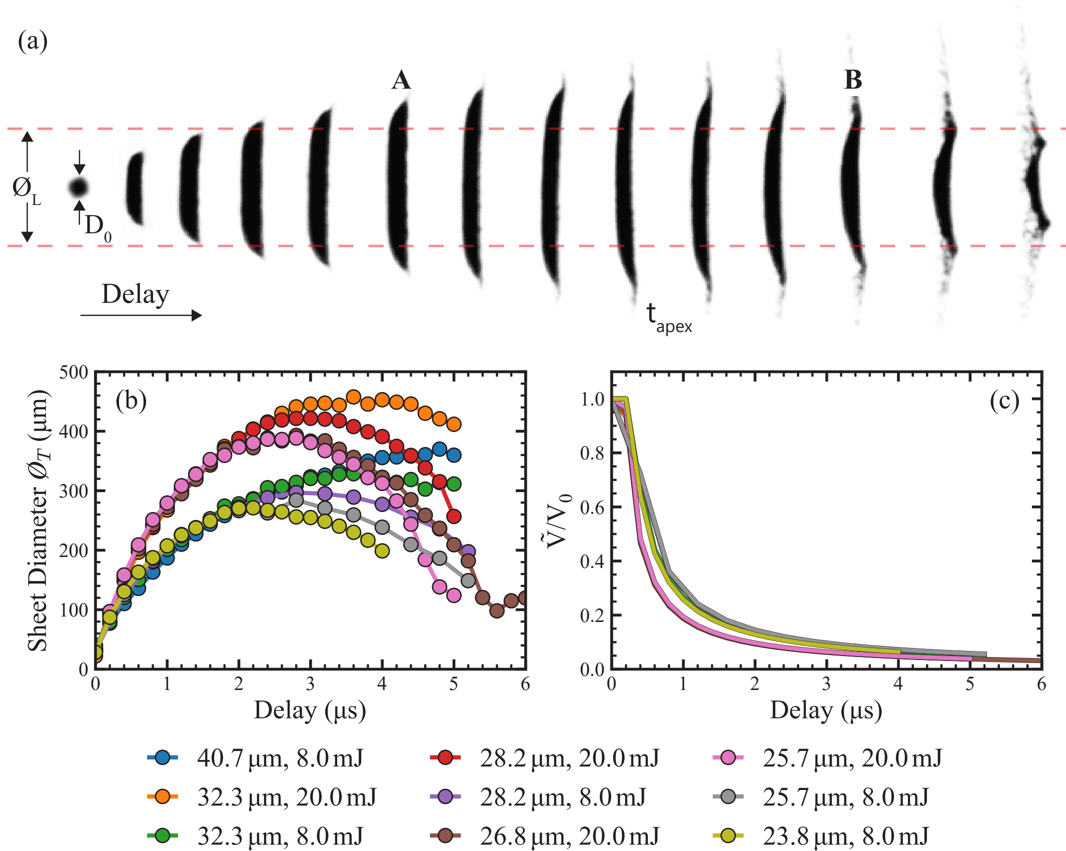

FIGURE 4.1: Tin droplet deformation and expansion. (a) Side-view shadowgraphy images of the preshaping of a 20 μm diameter tin droplet. Pre-pulse laser impacts from the left propelling and shaping the droplet with initial diameter D_0. A main-pulse laser diameter $Ø_L$ is indicated with the dashed line. The sheet reaches maximum diameter at the hydrodynamic apex time t_{apex} after which it contracts. Sheets **A** and **B** have similar sheet diameters but different average thicknesses. (b) The sheet diameter as a function of the expansion time (pre-pulse to main-pulse delay) for different droplet sizes and pre-pulse energies. (c) The calculated tin mass overlapping the main-pulse as a function of the expansion time following Villermaux and Bossa [85] through Eq. 4.6.

where V_0 is the initial droplet volume and u_0 is the initial expansion speed. The parameters a_0, a_1, and a_2 have been investigated by Liu et al. [12] and are shown to be 1.65(2), 6.9(3) and -2.4(8), respectively. We control the initial droplet diameter (D_0) and volume by varying the oscillation frequency of the liquid tin stream. The initial expansion speed is varied by changing the pre-pulse laser beam intensity, which alters the pressure impulse on the droplet and results in different propulsion and expansion rates. Accordingly, we can control the sheet thickness profile at the time of main-pulse laser impact by varying the droplet size, pre-pulse laser energy, and the pre-pulse to main-pulse delay time.

For simplicity in finding an analytical solution, we employ the simpler Eq. 4.4 in calculating the overlap volume. By substituting the sheet thickness given by Eq. 4.4 in Eq. 4.2, and following the findings of Liu et al. [12], we arrive at

$$V_{\text{sheet}} = \frac{2\pi V_0}{u_0}\int_{R_0}^{R(t)} \frac{1}{t}\,dr = \frac{2\pi V_0}{u_0 t}[R(t) - R_0]. \tag{4.5}$$

The integral limits are consistent with the initial droplet volume at $t = 0$ following the work of Villermaux et al. [85]. For early hydrodynamic times, this solution fails to predict reasonable sheet-laser overlap masses due to the limitations of the sheet thickness equation. This divergence is solved in calculating the sheet volume by utilizing the integral limits as of Eq. 4.5 [12]. We accordingly employ a piece-wise function to calculate the tin volume overlapping the laser beam ($\tilde{V}$), with exceptions at early times ($R_{sheet} < Ø_L/2$) to account for less than optimal laser-target overlap:

$$\tilde{V} = \begin{cases} V_0 & \text{if } R_{\text{sheet}} \text{ is} \leq Ø_L/2 \\ \frac{2\pi V_0}{u_0 t}[\frac{Ø_L}{2} - R_0], & \text{if } R_{\text{sheet}} \text{ is} \geq Ø_L/2 \\ \frac{2\pi V_0}{u_0 t}[R_{\text{sheet}} - R_0], & \text{if } R_{\text{sheet}} \text{ is} \leq Ø_L/2 \text{ and } t \geq t_{\text{apex}}. \end{cases} \tag{4.6}$$

The resulting calculated overlap volume normalized by the initial volume is shown in Fig. 4.1(c) for different initial droplet diameters and pre-pulse laser energies.

4.3 Theoretical Methods

In order to provide further understanding of the dynamics of mass use during laser exposure, we investigate 2 μm laser-driven plasma using RALEF-2D simulations [1]. We study the radiative hydrodynamic response of thin, flat tin disks of varying thicknesses and 150 μm diameter irradiated using a spatially and temporally flat-top laser pulse. The power density of the 2 μm laser pulse is maintained at 7×10^{10} W/cm^2 across an 85 μm beam diameter centered onto the tin target. The detailed workings of RALEF-2D simulations are described elsewhere [9, 67, 86].

We execute simulations of different tin target thicknesses to demonstrate the *overlap* mass dependence of the simulated laser-driven plasmas. We choose thicknesses in the range of 0.2–5 μm to be compared to the experimentally analogous preformed tin sheets. The overlapping tin mass is calculated based on the diameter of the laser beam and the tin sheet thickness. The simulations are executed up to 30 ns after laser impact with a time step of 0.5 ns.

[1]The RALEF-2D simulations were executed by Stan de Lange and analyzed by Yahia Mostafa.

The instantaneous and final conversion efficiencies are extracted from the simulations by detecting the escaped EUV light in the forward plane with respect to the laser axis. The laser intensity at the exit of the simulation is summed across the simulation domain to quantify the amount of escaped and transmitted laser light. Finally, EUV images are obtained by considering the local in-band emitting power at each time step. Only positive values of the local EUV power (emission) are considered and negative (absorption) values are reduced to zero. This consideration results in a more reliable computation of the 2D projected profile and time-integrated final result. While omitting the absorption regimes of the simulated plasma may alter the emission profile, we find there is minor differences when doing so, and accordingly choose the computationally reliable approach. The 2D profile of the in-band emission is Abel-transformed [87, 88] to obtain the projection as would be imaged in an experimental setup. This step is done using the PyAbel Python package [88]. The Abel transformation assumes an optically thin medium, where a cross-section of the cylindrically symmetric 3D plasma emissions is used to calculate the 2D projection as would be seen by an external observer [28, 87]. The assumption of optically thin media, underlying the Abel inversion approach, may limit the accuracy of our results. Although 2 μm laser-driven plasma has been shown to have less self-absorption at 13.5 nm [28] when compared to the 1 μm case, there may exist significant optical thickness altering the result of the transform. With larger optical thickness, we expect the resulting side-view images to be less bright due to the self-re-absorption of the EUV generated in the far-side of the plasma domain with respect to the observer. Nevertheless, we expect that the Abel-inverted images give important insight into the dominant emission area. The forward Abel-transformed images are summed for all time steps resulting in a time-integrated image of the EUV emission.

4.4 Mass Use

Using different liquid tin droplet sizes and pre-pulse laser energies, we form tin sheets of different thickness profiles as measured and calculated in Fig. 4.1. After a predetermined time delay, the 2 μm-wavelength main-pulse laser impacts the tin target forming the EUV emitting plasma. The 2 μm-wavelength drive laser characteristics are kept constant at 11 ns time duration and an intensity of 7×10^{10} W/cm^2.

In Fig. 4.2(a), we show the conversion efficiency of laser light into EUV light as a function of the target diameter $\varnothing_T$. The data shown are for targets generated using various pre-pulse energies and initial droplet sizes as shown in Fig. 4.1(b). We observe weak or no dependence of the CE on target diameter for diameters larger than the main-pulse beam size. Beyond full geometrical overlap, the emission anisotropy remains relatively constant resulting in similar EUV emission towards the forward 2π hemisphere. This lack of dependence of CE on target diameter is consistent with the observation of the CE dependence on geometrical overlap shown in Fig. 2 of Chapter 2.

Tin targets that do not exhibit full geometrical overlap with the main-pulse laser result in a large fraction of the laser energy escaping. This effect trivially decreases the CE and is the focus of the current study of mass use (see Chapter 2). Accordingly, targets with less than full geometrical overlap with the laser light are omitted from the plots of Fig. 4.2. Nevertheless, a large fraction of the generated plasmas exhibit a lower-than-optimum CE, specifically those of large target diameters. This suggests

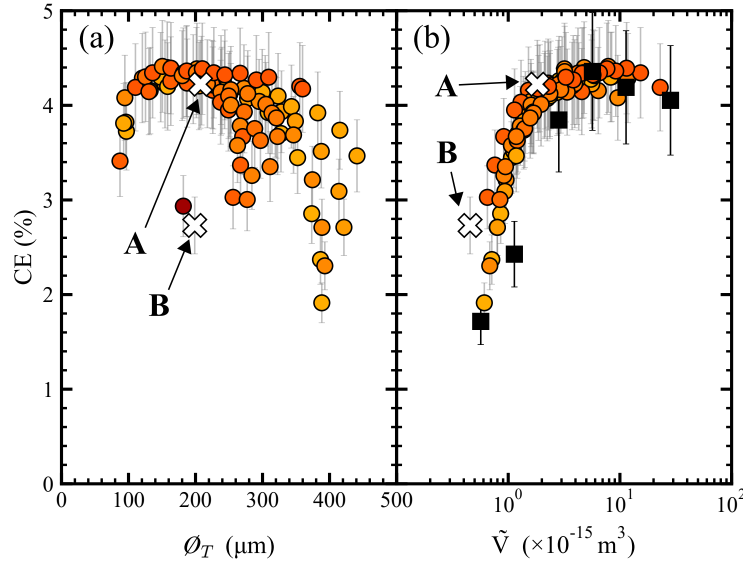

FIGURE 4.2: Dependence of CE on tin target parameters. Data points **A** and **B** indicate plasmas formed from similar target diameters but different thickness profiles obtained from the same droplet size and pre-pulse laser energy. (a) Experimentally measured CE as a function of tin target diameter using varying D_0 and E_p. (b) Collapse of CE as a function of calculated overlap volume (see the main text) with the main-pulse laser. Circle data points indicate experimental results. Square data points show the normalized RALEF-2D simulation results.

that the CE is additionally limited by something other than target diameter or laser characteristics.

To uncover the underlying origins of the limitations of CE, we turn to two example targets, targets **A** and **B**, which are preformed from the same droplet size using the same pre-pulse laser energy. The two targets have almost identical diameter (with full geometrical overlap with the main-pulse laser) but are observed at different expansion times. Target **A** is formed at the initial expansion trajectory of the preformed droplet and target **B** is formed beyond the apex time, after the sheet is contracting. The resulting prime difference between the two targets is the thickness profile as calculated by Eq. 4.6 and shown in Fig. 4.1(c). The decreased CE in target **B** is accordingly attributed to the limited thickness, and insufficient overlap volume of the target.

In Fig. 4.2(b), we show the same CE data shown in Fig. 4.2(a) as a function of the overlap volume calculated by Eq. 4.6. We observe a collapse of the spread in CE shown in Fig. 4.2(a) onto a single curve, indicating a strong dependence of the plasma emission characteristics on the available tin volume overlapping the drive laser. Similarly, targets **A** and **B** are highlighted demonstrating the difference in CE is due to different overlap volume.

The CE-$\tilde{V}$ curve shown in Fig. 4.2(b) shows a plateau of efficiency beyond a certain overlap volume. For plasmas formed using smaller overlap volumes, the available tin mass is not sufficient to maintain the EUV-emitting plasma and, thus, a lower CE is observed. For larger volumes, the CE plateaus near the optimum value for the 2 µm laser driver. Plasmas formed by tin sheets with very large overlap volumes

have excess tin volume and are not mass efficient since a similar efficiency plasma can be generated using less tin mass. The volume at which plasmas start exhibiting near peak CE (plateau) is around 2×10^{-15} m^3 for the present main-pulse settings.

RALEF-2D simulation results are shown in Fig. 4.2(b) in black boxes. The resulting CE is normalized to match the experimental results. The difference in peak CE values between the experimental and simulation results is around 40 % of the CE value, with the simulations here undershooting the experimental results. This difference is attributed to several parameter discrepancies between the experiments and simulations. In the simulations, a flat tin target with uniform thickness is assumed while in the experimental setting, the tin targets have a varying thickness profile and a sheet curvature. Additionally, the simulation results are shown to depend on simulation complexity (e.g. radiation groups, equation of state, and advection routines). The values shown here are from preliminary results of the simulated plasmas. The reduced complexity of the simulations shown here results in variation of the CEs, and an error based on these variations is calculated and shown on the data points in Fig. 4.2(b). In order to shift our focus on the mass use, we normalize the simulation results to demonstrate the similarities between the experimental and simulation results. Particularly, both sets of data demonstrate an increasing CE with increasing overlap volume, up until the point of optimum volume, after which the CE plateaus and does not increase further. The optimum overlap volume is shown to be slightly higher for the preliminary simulations and, consequently, further comparisons in this study take this apparent difference in mass-use rate into account.

The dependence of the CE of the generated plasmas on overlap volume is observed in Fig. 4.2(b) to be sub-linear with the dependence scaling approximately as CE $\propto \tilde{V}^{0.6}$. This less-than-linear dependence can be attributed to the different processes occurring using a low-mass target. While there exists mass flow from the liquid target towards the ablation front [9], we additionally observe mass propulsion and vaporization in the simulation results. For plasma generated using thin tin targets, the fraction of mass propelled away from the plasma, compared to the mass utilized towards the critical surface, is higher than for plasma generated using a thick sheet. The combination of the multiple factors contributing to mass use or loss results in the non-linear dependence of CE on overlapping tin volume as observed. We further note that despite the difference in the CE curve behavior between experiments and simulations, the slope of the increase in the mass-limited region is similar. This suggests that the complementary mass-use mechanisms observed in the simulations may also be occurring in the experimental study, although possibly at slightly different rates.

4.4.1 Burnthrough

In the previous section, we focused on the effect of available overlapping tin volume on the conversion efficiency of the generated plasmas. We observed a strong dependence of the EUV emission efficiency on the amount of volume overlapping the drive laser beam. In this section, we aim to observe the effects of overlap volume on other plasma characteristics, such as the size and morphology of the emission area and the time-resolved dependencies. We utilize both experimental and simulation results to observe differences between mass-sufficient and mass-limited 2 μm laser produced plasmas. For mass-limited plasmas, we observe the 'burnthrough' behavior, where the laser light ablates through the available mass and transmits through the tin target and plasma.

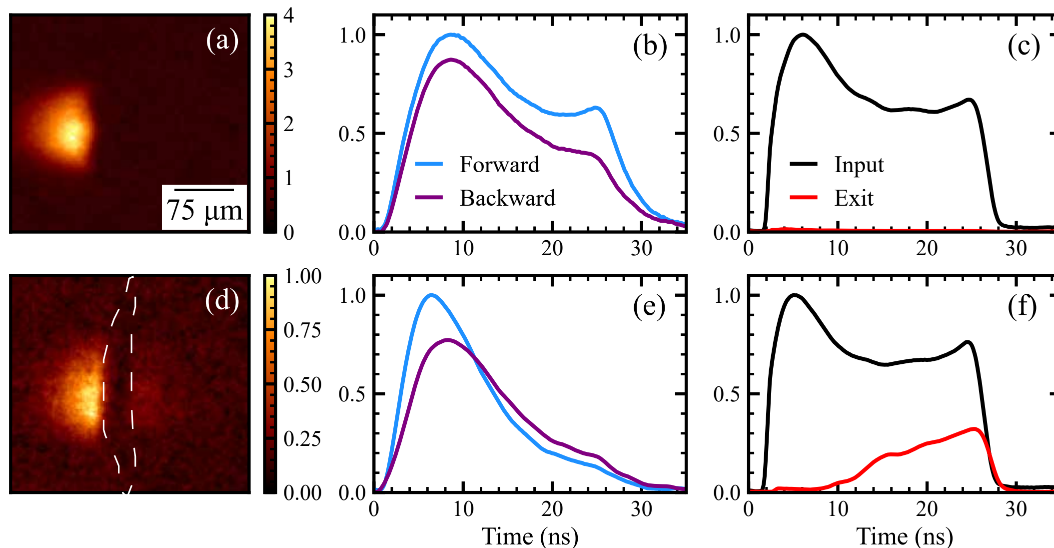

FIGURE 4.3: Experimental observations of mass-limited laser produced plasma using a 23.8 ns long flat-top main-pulse and $I = 6.5\times 10^{11}$ W/cm^2. The top row shows a high-CE non-burnthrough case to be compared to the bottom row showing a mass-limited low-CE plasma. Panels (a) & (d) show time-integrated side-view images of the EUV emission for the high-CE and mass-limited cases, respectively. The color bars indicate the local emission intensity in arbitrary units. The laser impacts from the left. In (d), the dashed lines indicate a line-out of the curved tin sheet as observed using shadowgraphy imaging. The ratio of maximum (local) emission intensity between the two cases is 4:1. Panels (b) & (e) show the time-resolved normalized EUV emissions in the forward (21°) and backward (159°) directions with respect to the laser. Panels (c) & (f) show the measured 2 µm laser light fired towards the tin sheet (Input) and the transmitted light after the tin sheet or plasma at the exit of the vacuum chamber (Exit).

In Fig. 4.3(a), we show an EUV image [similar to Chapter 2 Fig. 2.4(a)] of a high-CE plasma, sustained by a 107 μm diameter tin sheet of an average thickness of 2 μm overlapping the main-pulse. This target was preformed from a droplet with an initial diameter of 52 μm. For the same plasma, Fig. 4.3(b) shows normalized fast-photodiode time-resolved measurements of the EUV light emitted towards 21° (forward hemisphere) and towards 159° (backward hemisphere) with respect to the laser. In Fig. 4.3(c), the measured laser light intensities at the entrance and exit of the vacuum chamber are shown to demonstrate the input and transmitted laser light, respectively.

In a high-CE plasma as shown in Fig. 4.3(a),(b)&(c), the EUV emission profile follows the temporal profile of the drive laser. This similarity is observed for both the forward and backward emissions indicating that the dependence of EUV emission on the laser profile is isotropic. In this mass-sufficient case, the EUV emission is sustained throughout the entire drive laser pulse and no laser light at the exit of the chamber is observed. We can confidently conclude that in such a high overlap volume case, there is no burnthrough behavior.

A low-CE plasma is generated using identical main-pulse parameters driving a 282 μm diameter tin sheet. The tin sheet was achieved by preforming a 20 μm diameter droplet. This larger sheet diameter and smaller initial droplet size, compared to the high-CE case, result in a target with very little mass. Fig. 4.3(d) shows the side-view image of the EUV emission from this plasma which exhibits burnthrough characteristics. The dashed line indicates the outline of the curved tin sheet as observed through side-view shadowgraphs [$\sim$ 30 μm wide, cf. Fig. 4.1(a)]. Behind the shadow of the tin sheet, we observe EUV light emission which indicates a punch-through of the plasma and propulsion of the small amount of mass sustaining the plasma. Similar to Fig. 4.3(b), Fig. 4.3(e) shows the time-resolved EUV emission for the mass-limited plasma in the forward and backward directions. Fig. 4.3(f) further shows the measured laser light driving the plasma (Input) and transmitted or scattered through the plasma (Exit).

In comparison with the non-mass-limited case in the top row of Fig. 4.3, the mass-limited plasma in the bottom row shows a few burn-through indicators. As mentioned, there exists EUV light emission beyond the tin sheet as shown in Fig. 4.3(d) which does not exist in the mass-sufficient plasma. This EUV light measured may be an indication that the plasma is consuming the entirety of the overlapping tin mass and the plasma is propelled in the direction of the laser beam. There is also a clear observation of the reduction of emitted EUV (and consequently CE) in later times as shown in Fig. 4.3(e). The time at which the EUV emission deviates from following the laser profile [as is the case in Fig. 4.3(e)] highlights the time at which the available tin mass is no longer sufficient. This matches, roughly, with the time at which the laser light starts to transmit through the light source, $\sim$12 ns, as demonstrated in Fig. 4.3(f).

We show similar results from the radiation hydrodynamic simulations in Fig. 4.4. The top row of the figure demonstrates a mass-sufficient 2 μm laser-driven plasma, while the bottom row shows a mass-limited case. Fig. 4.4(a), (b) & (c) show the result of a 5 μm thick flat tin target illuminated by an 85 μm diameter beam. This thickness is chosen to ensure sufficient overlapping volume and no burnthrough. The bottom row, Fig. 4.4(d), (e) & (f), show a similar parameter simulation but with a thinner sheet thickness of 200 nm. This sheet thickness is chosen since it matches the experimental burnthrough case shown in the bottom row of Fig. 4.3.

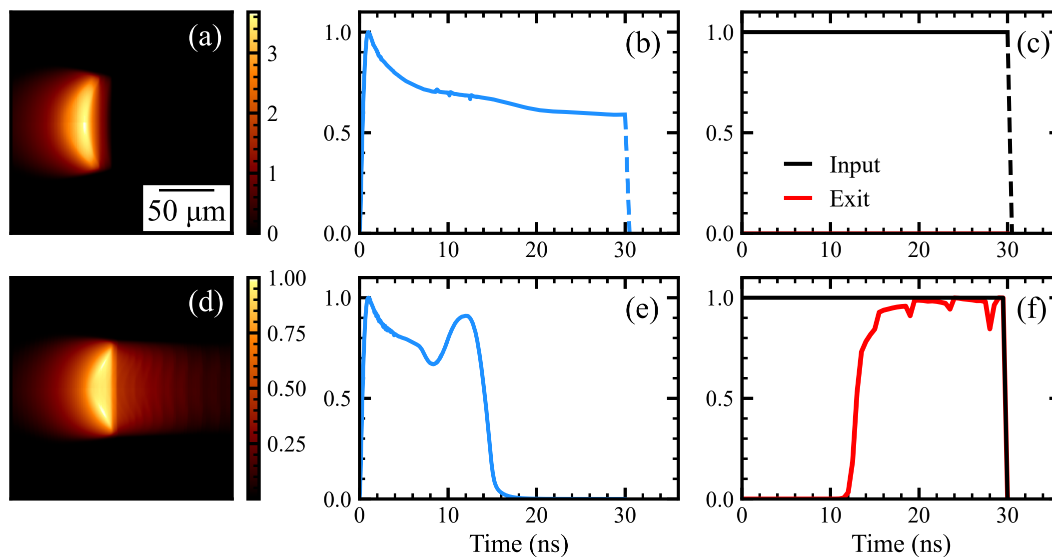

FIGURE 4.4: Observations of burnthrough in 2D hydrodynamic simulations in RALEF. Top row panels (a)–(c) show the results for a non-burn-through case of a 5 µm thick target to be compared to the bottom row (d)–(f) of simulated 200 nm burn-through case. (a) & (d) show the time-integrated Abel-transformed EUV emission images for the 5- and 0.2 µm tin sheet simulations, respectively. The ratio of the maximum emission intensity in (a) and (d) is 4:1. (b) & (e) show the normalized instantaneous EUV emission detected in the forward hemisphere. The dashed line in (b) is an artificial (the simulations run up to 30 ns) cut-off of the emission to demonstrate the drop in EUV emissions if the laser light is stopped (c) & (f) show the input 2 µm laser light and the exit laser light as detected behind the plasma light source. The dashed line in (c) shows the end of simulation time.

The simulation results of a mass-sufficient EUV emitting plasma shown in the top-row of Fig. 4.4 show results analogous to the experimental counterpart. The image of the EUV emissions [Fig. 4.4(a)] demonstrates a morphology similar to the experimental result. As expected from a mass-sufficient plasma, no laser light escapes the tin target and no plasma emits on the backside, as shown in Fig. 4.4(c). On the other hand, the EUV emission of the simulation results does not follow the flat temporal profile of the drive laser. We observe an initial sharp increase of the EUV emission attributed to the plasma formation time (<1 ns) followed by a gradual decrease of the instantaneous EUV emission. This profile is observed to be dependent on the simulation complexity and motivates further theoretical studies with increased complexity.

Simulations of a mass-limited plasma as shown in the bottom-row of Fig. 4.4 demonstrate results similar to the experimental mass-limited plasma. We observe EUV light emission behind the initial position of the tin sheet in the EUV emission images. In comparison to the experimental case, due to the absence of any sheet curvature and the planar nature of the simulations, we observe no shadow of the sheet. The instantaneous EUV emission shown in Fig. 4.4(e) demonstrates a sudden stop preceded by a slight increase in the EUV emission. The EUV emission stops at that time since there is no remaining tin mass to sustain the plasma. At later times, the mass diminishes to a level where the remaining liquid tin forms multiple small targets (high-density ‘ islands’) and vaporizes at which point the laser light is transmitted. The increase in EUV emission prior to burnout is caused by the changed emission anisotropy due to the morphology and low density of the tin target. The EUV emission resulting from this changed morphology and density is challenging to compute. The calculated laser absorption and EUV emission deviate from the values expected from the experimental results. Similar to the experimental case, we observe laser light at the exit of the simulation domain (passing through the tin target/plasma) at a similar time point that also roughly matches the point of diminishing EUV emissions.

Although the calculated experimental average thicknesses in Fig. 4.3 differ from the simulated thicknesses in Fig. 4.4, we observed many similarities. Comparing the mass-sufficient and mass-limited cases, we calculate the ratio of peak emission intensity as observed in the EUV images. For the experimental case, the ratio is calculated to be 4, very nearly identical to that of the simulations. This suggests a large similarity in the differences we observe comparing mass-sufficient to mass-limited targets, independent of whether it is experimental or simulated. We can thus conclude that the RALEF-2D simulations may provide us with further insights into the dynamics of the generated plasmas, which are difficult to obtain experimentally.

Next, we would like to demonstrate the observation of gradual burnthrough as the sheet thickness is decreased, using side-view EUV images. Additionally, this observation illustrates the extent of experimental control of burnthrough and the degree that the side-view EUV images are an accurate predictor and metric of plasma burnthrough.

In Fig. 4.5 we show the EUV images for plasmas formed from seven different initial droplet diameters preformed into 10 different sheet diameters (and correspondingly, thicknesses). For this set of studies, we employ a spatially larger main-pulse of 144 μm diameter, previously shown in Chapter 2, Fig. 2.1(e). The larger diameter of this laser setting allows us to take images significantly above the resolution limit of the EUV imaging setup (which is approximately 6.5 μm) and thus we can capture, in

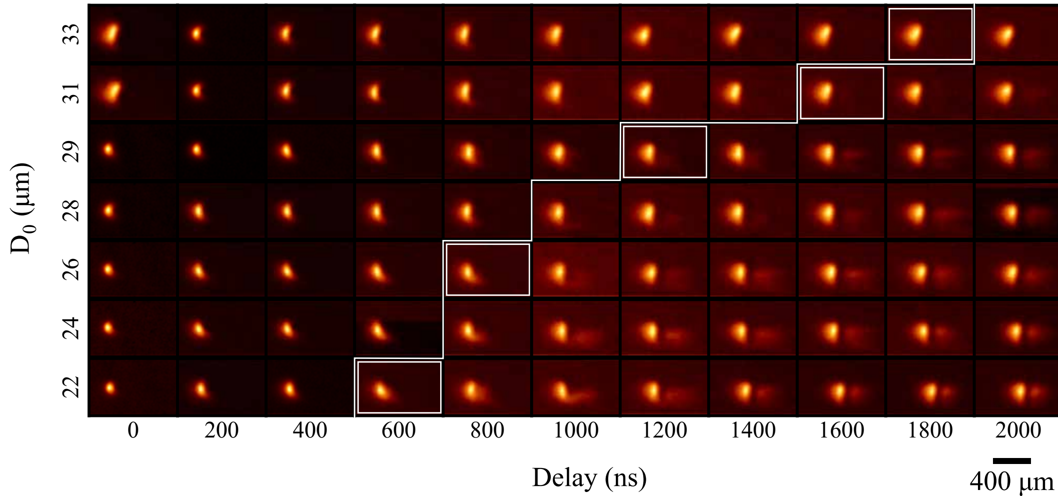

FIGURE 4.5: Side-view images of the EUV emission from mass-limited plasmas generated by a 2 μm laser using different tin targets. All targets are preformed using a pre-pulse with energy 8 mJ. Various droplet sizes and delay times are used, as indicated along the respective axes. The sheet thickness decreases along the diagonal (from left-upper to right-lower corner. High-CE minimum mass use cases of the same overlap volume (±7 %) are highlighted with a white box. The white line separates mass-sufficient cases (to the left) from mass-limited cases (to the right). A scale bar (relevant for all images) is shown at the bottom right.

4

detail, the variation in the emission across the emission area. For decreasing droplet size and an increasing pre-pulse to main-pulse delay time, the average sheet diameter decreases (see Eq. 4.4 and Eq. 4.3). Consequently, with decreasing sheet thickness, we observe more and more EUV light at the backside of the initial position of the tin sheet, relative to the main plasma generated at the front of the sheet. Optimum mass-use cases, as determined by the CE, are highlighted by the white boxes shown in the figure. The white line drawn separates the mass-limited cases from non-burnthrough measurements, as determined visually from the images. Plasmas to the left of the white line show no demonstration of mass-limited behavior while the images on the right show burnthrough of the EUV emission.

In the EUV images shown, we observe asymmetric burnthrough in mass-limited cases, where we detect EUV light at the backside of the tin sheet in the lower half of the images at higher thicknesses first, then symmetric emissions with decreasing thickness. This asymmetry of mass use rate can be directly correlated with the main-pulse laser's spatial intensity profile shown in Chapter 2, Fig. 2.1(e). The higher intensity lower half of the laser profile is associated with a higher mass use rate. This follows the work of Burdt et al. [31] and Basko et al. [9], where the mass use rate of a laser-produced plasma is shown to increase with laser intensity and decrease with laser wavelength. Accordingly, despite the symmetry of the preformed tin target, the burnthrough occurs asymmetrically for thicker tin sheets. For thinner tin targets, the laser burns through the available mass across its entire spatial profile and thus the asymmetry is not observed in our (non-time-resolved) EUV images. We predict that with sufficient nanosecond time-resolved images, the asymmetry caused by the main-pulse spatial profile may be resolved as the laser will burn through at the higher intensity spots first (assuming the laser spatial profile is time-invariant).

4.5 Mass Use Dependencies

In this section, we study the dependence of mass use, and specifically the burn-through characteristics, on the drive laser's intensity and the pulse duration. Since CE varies depending on the laser intensity (cf. Chapter 2), we base this study primarily on the observations of escaped laser and EUV light as well as light detected on the backside of the tin target as seen in EUV images.

As mentioned in the previous section, the mass use rate has been previously studied and is found to relatively weakly depend on the laser intensity [9, 31, 89]. The dependence on drive laser intensity is found to be less than linear: $\dot{m} \propto I^{0.56}$, for experimentally studied solid tin planar targets [31, 89] and a weaker $\dot{m} \propto I^{0.19}$ for spherically symmetric droplet targets derived by analytical studies of the laser ablation front [9]. Thus, we may expect the power dependence to depend on the tin target geometry. Since for our experiments, we use liquid tin planar targets which are prone to propulsion similar to the analytical studies, we predict the observed power dependence to lie in between these two specified cases.

4.5.1 Power Density

We observe the burnthrough characteristics for plasmas driven by three different main-pulse intensities of 2.4, 6.5, and 8.8 $\times 10^{10}$ W/cm^2 using an identical beam diameter of 85 μm and a pulse duration of 28 ns. In Fig. 4.6, the normalized laser light driving the plasma, the escaped laser light, and EUV emissions towards the forward and backward directions are shown. For each laser intensity case, the detected light signals are shown along with the side-view EUV images demonstrating the plasma burnthrough.

The laser-target overlap volume is identical in each case, and the sheet diameters are similar. For the lower intensity study, a different pre-pulse energy and droplet size was used and, thus, the position of the sheet, and correspondingly the plasma, is in a different location, as becomes apparent comparing Figs. 4.6(b) and (d). We also note that the temporal profile of the drive laser (Input) is slightly different for each case due to some variation in the laser output characteristics overthe course of the study. Nevertheless, the general shapes, and energies enclosed in full-width-half-maximum, are very similar.

We observe similar burnthrough for all three intensity cases with some differences in the emission characteristics. The time of initial transmission of (Exit) laser light is earlier for increasing laser intensity, although it is similar for the latter two cases. The peak of EUV emissions in the backward direction increases with increasing drive laser intensity. The backward EUV emissions detected by the diode (Fig. 4.6: left column) match the observation of increasing EUV light at the backside of the tin sheet as seen in the EUV images (Fig. 4.6: right column).

The observation of increasing burnthrough with increasing drive laser intensity can be observed by the backward EUV emissions and EUV images. However, little can be inferred in comparing the exit laser light as may be expected given the weak dependence of mass use rate on intensity. According to the analytical model [9], the mass flow rate is expected to increase only by approximately 20 %, comparing the lowest and highest intensity cases, despite a ∼2.5x increase in laser intensity. As observed in the backward EUV emission profile, the peak emission intensity increases by ∼40 % while the total emission (detected integral) remains roughly the same. The

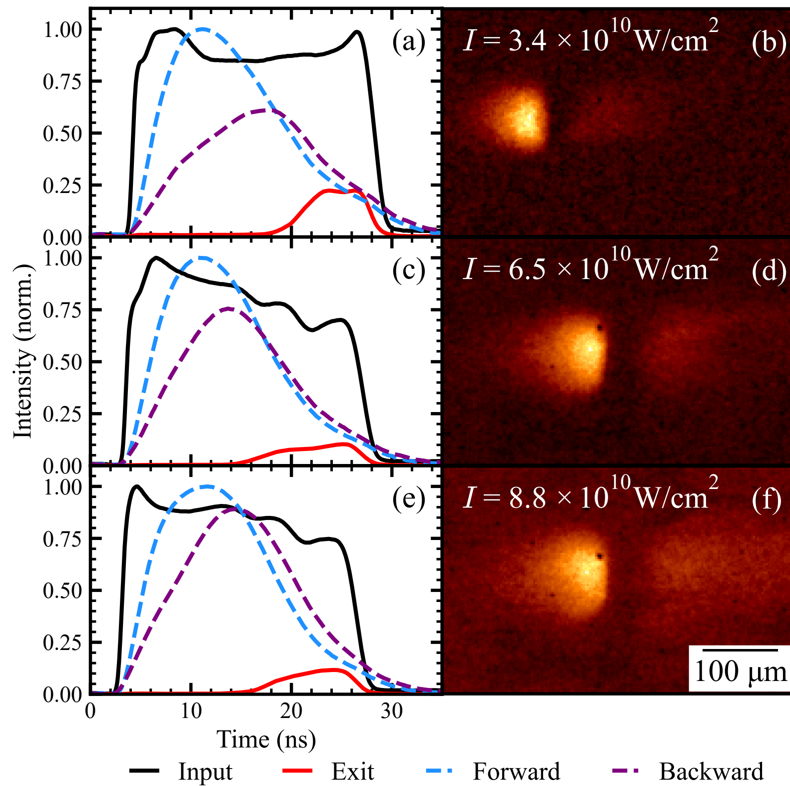

FIGURE 4.6: Plasma burnthrough characteristics on similar sheet diameter and thickness for three different 2 µm wavelength drive laser intensities. (a) Input and exit laser light, and EUV emissions in the forward and backward directions using a laser intensity of 3.4×10^{10} W/cm^2. (b) Normalized side-view EUV images under identical settings are shown in (a). Subfigures (c) and (d) show the results for an optimal (w.r.t. CE) EUV emission plasma driven by a laser intensity of 6.5×10^{10} W/cm^2. Panels (e) and (f) show the results for a higher than optimum drive laser intensity of 8.8×10^{10} W/cm^2. A scale bar relevant for all EUV images of 100 µm is shown.

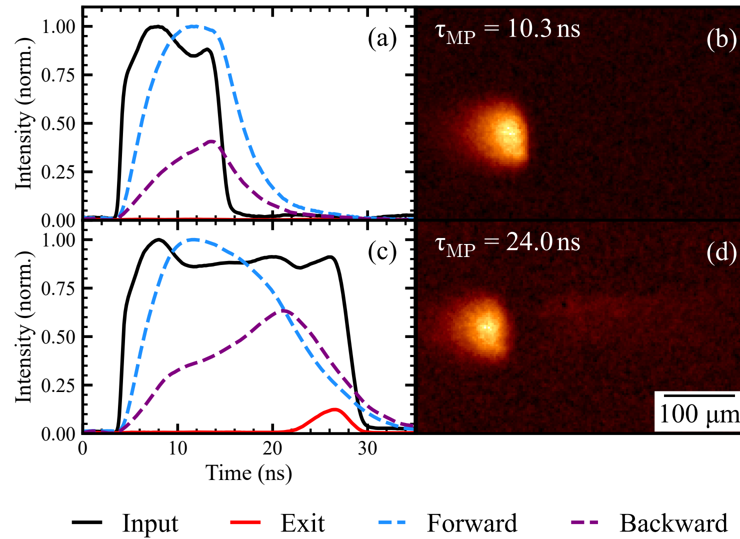

FIGURE 4.7: Comparison of the mass use of 10- and 24 ns long main-pulse driven plasmas generated by identical tin targets. Subfigures (a) and (b) show the results using a 10.3 ns long uniform intensity main-pulse on a 328 µm sheet with an average thickness of 70 nm. Subfigures (c) and (d) show the plasma characteristics under identical tin sheet diameter and thickness using a 24.0 ns long drive laser pulse. For each main-pulse duration case, the input and exit laser light are shown along with the plasma EUV emissions in the forward and backward directions. The right column shows the side-view EUV images of the generated plasmas showing burn-through for the 24 ns case. The scale bar for EUV images is shown in sub-panel (d).

total emission is observed to be similar for all drive laser intensity cases, despite increasing peak emission, due to the offset of burnthrough becoming earlier for higher intensities. This is difficult to observe directly due to the ∼ns RC time constant of the photodiode. Another factor contributing to the limited effect of laser intensity is the varying temporal profile of the drive laser. In the lower intensity case, the laser profile maintains near maximum intensity while in higher intensity cases there is a decrease across time. We note here that our calculation of laser intensity is based on an *assumed* perfect flat-top, and accordingly does not take into account the measured variations in the temporal profile.

4.5.2 Pulse Duration

Next, we aim to observe the effect of laser temporal pulse duration (τ_{MP}) on the burnthrough characteristics. Through maintaining a similar average intensity, the mass use rate is assumed to be kept at a fixed value. We study here two plasmas driven by the same laser intensity and target morphology (thickness and diameter), with two different pulse durations of 10.3 ns and 24.0 ns.

Fig. 4.7 shows the results of driving a 330 µm diameter tin target using an 85 µm diameter laser. The target is chosen to be larger than the beam to ensure full overlap. The laser intensity is kept near the optimum for EUV emission at 6.5×10^{10} W/cm^2 and the pulse duration is varied from 10.3 to 24.0 ns. The top row shows the results

for the shorter pulse duration case, demonstrating laser and EUV light measurements as well as the side-view EUV image. Similarly, the bottom row of Fig. 4.7 shows the results for the longer pulse duration measurement.

For the 10.3 ns pulse duration case we observe mass-sufficient behavior of the EUV emissions as well as no escaped laser light. This short pulse duration case also demonstrates a small EUV emission area and no light at the backside of the initial position of the tin sheet. These qualities are similar to the high-CE measurements shown in Chapter 2. In contrast, the same target illuminated using a 24.0 ns demonstrates reduced EUV emission (normalized by the pulse duration), and shows EUV at the backside of the tin sheet and escaped laser light. In Fig. 4.7(c), the forward EUV emissions can be observed to deviate from following the input laser light. At the same time of ∼22 ns (laser pulses are offset from zero), more escaped laser light is detected at the exit. We can thus conclude that for a sheet of this overlap volume of 1.6×10^{-15} m^3 there is sufficient mass to maintain plasmas driven by lasers of pulse durations of up to ∼20 ns. This overlap volume limit is similar to the value observed for 11 ns pulses in Fig. 4.2(b) of 2×10^{-15} m^3. Shorter pulse duration cases, such as the 10.3 ns case demonstrated, have sufficient overlap volume to maintain the plasma. Plasma driven by longer pulses will exhibit limited EUV emission and burnthrough.

The dependence of the mass use on pulse duration is expected to be linear, assuming a constant mass use rate. This assumption excludes effects of plasma onset (ion excitation and establishment of the critical surface) and plasma cool down effects. Both the onset and offset affect the observed linear dependence of mass use on the pulse duration of the drive laser. At the initial times of plasma generation, there are a few nanoseconds where the inverse-Bremsstrahlung absorption occurs, excites tin atoms, and establishes a plasma front [9]. This period of plasma formation may have a different mass-use rate than that of later times (>5 ns). When the drive laser light stops, there may additionally be a certain time where the tin plasma emits light while cooling down. However, we predict this cool-down time to be minimal (<1 ns) for the plasmas generated in this work, as supported by the simulation results. With longer pulses, the effects of the onset and offset times would be minimal, compared to the quasi-stationary behavior present throughout laser exposure [9].

We conclude on a weak dependence of the mass use rate on drive laser intensity, matching expectations based on relevant literature. This result may allow for the scaling of EUV output power, by scaling the intensity, with a limited need for increasing in the supplied mass. We additionally compare plasmas generated by short and longer pulse durations and demonstrate the need for additional mass for longer pulses, hypothesizing a near-linear scaling of mass use with pulse length. We however note that plasma onset and offset effects point towards a more favorable average mass-use rate for plasma driven by longer pulses.

4.6 Conclusion

In this chapter, we investigated the mass use of 2 µm wavelength laser driven tin plasmas. In contrast to previous studies and chapters, which focus only on EUV emission efficiency, we have identified a major dependence of the conversion efficiency on the tin volume overlapping the laser beam. We observe that for plasmas driven under a CE-optimized laser intensity, 85 µm beam diameter and 11 ns pulse duration, an optimum overlap volume is around 2×10^{-15} m^3. This optimum

is based on the emission characteristics of the EUV-emitting plasma. Generating plasma using thicker tin sheets results in excess mass with no increase in CE. Using thinner sheets results in laser burnthrough behavior where there is insufficient mass to maintain the tin plasma and consequently the emission efficiency decreases. We compare our experimental results of the dependence of CE on overlap volume with hydrodynamic simulations of a similar setup. We observe large similarities between the experiments and simulations which may allow us to further understand dynamics not detectable solely through experiments.

We compared the results from experimental and simulations for plasmas generated by 2 μm wavelength laser light using two different sheet thicknesses. We demonstrate key burnthrough metrics such as the time-resolved EUV emission anisotropy and escaped laser light. While the simulations result in slightly different mass use rates and accordingly require more mass than the experiments, the dynamics are shown to be identical. Side-view images of the EUV emissions are compared for mass-sufficient and mass-limited plasmas for both experiments and simulations. The origin of the light observed at the backside of the initial tin sheet position is identified to be due to the propulsion of the limited mass, as observed in the simulations.

EUV images are shown to be a key indicator of burnthrough behavior. By observing the EUV light emission at the backside of the sheet, we can accurately predict the mass-limited behavior of the generated tin plasmas. We further show the dependence of the burnthrough on the spatial intensity profile of the laser, where it burns through faster at higher intensities spots in the profile. Accordingly, we investigate the dependence of mass-limited behavior on the laser intensity for three intensities relevant for EUV nanolithography. We observe some dependence, however it is shown to be weak, as is supported by previous studies. Finally, the mass use rate is demonstrated by studying plasmas driven by two pulse durations under otherwise identical conditions. As expected, shorter pulse durations are shown to require less overlap volume while longer pulses demonstrate burnthrough for the same tin sheet thickness.

Industrial EUV sources employed for nanolithography generate plasma using a 10 μm wavelength laser driver of several-ten-nanoseconds [19, 20]. For comparison to our current work, we consider previously studied plasmas driven under industrial conditions using a shorter pulse duration of 15 ns [19]. In such cases, the 10 μm wavelength laser illuminates a preformed ∼30 μm tin droplet at a 100 kHz rate generating upwards of 250 W of in-band EUV power [19]. Assuming such a system utilizes the entirety of the available tin mass, the energy-per-unit-volume is calculated to be around 8×10^{14} mJ/m^3 per laser shot. As a side note, we may calculate, based on the numbers above, that mass-efficient laser-produced plasmas emit around three EUV photons per available tin atom. In state-of-the-art industrial vessels, optimization to values of 2–3×10^{15} mJ/m^3 per laser shot were reported. In our experiments, using a 2 μm wavelength laser driver of 11 s pulse duration, we calculate an energy efficiency of 7×10^{14} mJ/m^3 per laser shot, considering only the volume overlapping the beam. These numbers are remarkably close to those of Ref. [19] while the comparison to the state-of-the-art presents an active challenge. However, in our case there is more mass in the initial droplet: most of the mass is not utilized for EUV generation as the target is pre-shaped to sizes larger than beam diameter. With careful target shaping to minimize non-utilized mass, the initial tin volume can be driven closer to the overlapping volume. By doing so, the similar values for the mass use suggest

that the 2 μm wavelength laser-driven plasma may demonstrate similar mass use rates to the state-of-the-art systems employed for nanolithography applications.

This work lays the foundation for future studies considering the mass efficiency of laser-produced plasma light sources. Future studies could numerically investigate the dependence of the mass use rate on laser intensity and wavelength. We have demonstrated the criticality of having sufficient tin mass overlapping the drive laser beam. A tin target can accordingly be developed to have optimum mass, such that debris is limited while maintaining high EUV emission efficiency. Future work could address the mass efficiency considering the total input mass as delivered by the initial tin droplet. Following Liu et al. [12], a tin target with optimal overlap volume and minimum initial droplet size can be developed and optimized.

Conclusion

We set out to explore and characterize tin plasma extreme ultraviolet light sources alternative to the current industry standard. Specifically, we consider 2 µm wavelength lasers as an alternative to the state-of-the-art 10 µm wavelength drivers used in high-volume nanolithographic manufacturing. This consideration is based on the higher wall-plug efficiency of solid-state lasers capable of producing 2 µm light [90], as well as high laser-to-EUV conversion efficiencies [28]. Combined, a more efficient EUV light source may be in our hands to investigate.

We investigated 2-µm-laser-produced plasma light sources primarily experimentally in a controlled setup. We streamed droplets of liquid tin through a nozzle in a high-vacuum chamber. The droplets were preformed using a low energy 1 µm wavelength 'pre-pulse' laser, altering the morphology and mass distribution of the tin target. The targets formed were thin, relatively flat tin sheets. Subsequently, a higher energy, plasma generating, 2 µm 'main-pulse' impacts the tin target. The generated plasma emits primarily at 13.5 nm as well as a cascade of other wavelengths and highly energetic positively charged tin ions.

Since the quality of experimentation depends heavily on the understanding of our tools and devices, a large amount of effort was spent on the instrumentation. Neutral tin mass detectors (quartz microbalances) were installed to characterize the amount of emitted mass from the generated tin plasmas. Such mass detectors also allow for the calibration of the transmission of the main-pulse laser through the tin deposited on entrance windows. EUV-sensitive devices were extensively investigated and routinely calibrated in order to maintain reliable and accurate measurements of the EUV emissions. A set of time-resolved EUV-sensitive diodes were installed, characterized and utilized for many of the measurements in this thesis. In order to understand the plasma EUV source morphology, a concave mirror imaging system was designed, developed, installed and subsequently improved. Finally, we focused on developing and testing devices to be used in future research, expanding our understanding of EUV emitting plasmas.

In Chapter 1, we described a novel simultaneous imaging and spectroscopy device. Using a combination of a diffraction grating and tailored tapered zone plates, we could acquire the full spectrum of emission from the plasma, as well as a 1D image of the source at each wavelength, simultaneously. We demonstrated the workings of this device on a solid-target plasma light source where we characterized emissions in the 5–80 nm wavelength range. We further characterized the device response by performing plane-wave propagation simulations and comparing their results to the experimentally obtained measurements. We found a clear match which allows us to further decompose higher diffraction orders and understand the origins of the features present in the experimental results. Such a simultaneous imaging and spectroscopy apparatus can be employed further to study liquid tin plasma light sources relevant for nanolithography.

In Chapter 2 we demonstrated a high efficiency, compact EUV tin plasma light source driven by an in-house built 2 μm laser. We reached a record 5 % efficiency comparable to the industrial counterpart. This high efficiency is enabled by tuning the laser temporal and spatial profiles into a uniform intensity flat-top. Using constant intensity profiles, the plasma is driven to the same optimum temperature across the area illuminated by the beam. The dependence of emission efficiency, output energy, and source size on the laser parameters were investigated. Accordingly, high energies up to 12.5 mJ and high efficiencies were recorded for larger beam diameters and longer pulse durations. We observed the emission size of the plasma using a 13.5 nm wavelength imaging system where we find the plasma size to be compact. Therefore, this 2 μm driven, high brightness source can be employed in nanolithographic machines as it falls well within the reported etendue requirements.

In Chapter 3 we characterized the full energy emission of 2-μm-laser-driven tin plasmas. We investigate the photonic emissions as well as ionic emissions using a set of diodes, spectrometer and retarding field ion analyzers. Tallying up the total measured energies at >1 m from the plasma, we could reconstruct up to 99 % of the input laser energy for plasma driven by a low intensity laser pulse. For an optimum EUV emitting plasma, we reconstructed up to 82 % of the energy. While most of the photonic emissions occurred in the EUV range (6 %), the full emission spectrum carried around 63 % of the emission energy from the plasma. Additionally, the kinetics of the energetic ions accounted for 16 % while their ionization potential energy is found to be up to 2 % of the input laser energy. Although many energy loss channels remain undetected (such as escaped laser energy, reflected laser light, emission beyond the recorded spectral ranges, any unrecorded anisotropies in spectral components and energy into neutral tin emissions) we could recalculate a relatively high fraction of the initially supplied laser energy. Consequently, an understanding of the full energy picture, and partitioning of emission into EUV light versus ion (kinetic) energy can be further investigated and optimized.

Finally, in Chapter 4 we switched our focus towards the *mass* use efficiency of 2 μm laser produced plasma. We identified that the emission efficiency of the generated plasmas depends heavily on the available tin mass overlapping the main-pulse laser beam. The optimum required overlapping mass was calculated for the laser intensity and pulse duration case investigated. We studied the mass-limited plasmas both experimentally and aided by preliminary RALEF-2D hydrodynamic simulations. We identified many similarities between the experimental and simulation results. In both cases, we investigated the effect of insufficient mass on EUV emission, its anisotropy, and on the laser light that escaped through the tin plasma. We further demonstrated the reliability of side-view EUV imaging in demonstrating plasma burnthrough. Finally, we observed the effect of laser intensity on mass use and displayed the temporal development by observing plasmas driven by main-pulses of different temporal durations.

2 μm Laser Driven Plasma

We opened this thesis with the following research question:

What parameters determine the mass & energy efficiency of tin plasmas driven by a 2 μm wavelength laser?

Through the understanding gained in Chapters 2 & 3, we can formulate an answer to the subquestion related to energy efficiency. The energy efficiency of a 2 µm wavelength laser produced plasma depends heavily on the laser characteristics, provided the tin target exhibits full geometrical overlap with the laser pulse. We have found that the energy enclosed within the full-width-half-maximum of the laser (an indicator of the quality of spatial uniformity) profile is a good indicator of CE. A high-efficiency plasma can be generated using a spatially and temporally uniform laser pulse impacting a tin target. The higher the quality of the uniform spatial and temporal flat-top, the higher the CE. We have further demonstrated the effect of varying laser intensity, beam diameter, and pulse duration on the efficiency and total energy output. We conclude that a small sacrifice in energy efficiency, by significantly increasing laser intensity and beam diameter, yields high energy outputs. The first part of the answer to the research question is, in order of priority: laser-target geometrical overlap, laser profile uniformity, laser intensity, beam diameter, and pulse duration.

Through the learnings of Chapter 4, we can address the parameters determining the mass use efficiency. We observed that full geometrical overlap of the tin target is not the sole target parameter metric contributing to the energy efficiency of the produced plasma. A mass-sufficient (enough mass), preferably mass-efficient (just enough mass), tin target is required to sustain a high-energy, high-efficiency laser-produced tin plasma source. We find that mass-limited plasmas exhibit lower CE attributed to the burnthrough of the laser pulse through the tin target. The mass use efficiency of high EUV emitting plasmas is calculated to be similar to that of previous works investigating industrially relevant sources [19].

We further consider prospective EUV sources driven by 2 µm wavelength lasers. An optimum EUV source would need an appropriate drive laser intensity, long pulse duration, and sufficient tin mass. The drive laser intensity can be increased beyond the value required for optimum EUV emission efficiency in order to gain a higher energy output per laser pulse. Scaling the laser intensity to be slightly higher increases the EUV emission energy and requires little mass increase due to the non-linear dependence discussed in Chapter 4. This higher drive laser intensity, in combination with a long pulse duration will allow for high EUV emission energies at reasonable efficiencies and mass requirements.

The drive laser beam diameter needs to be tuned to balance the gain in EUV emission energy with the mass losses associated with preforming a tin target (to allow full geometrical overlap). Larger tin targets require considerable hydrodynamic deformation which results in mass loss through the ejection of fragments during the expansion time [12]. Accordingly, a laser beam with a diameter larger than 200 µm, requiring a tin target diameter of >200 µm, would be associated with a low mass use efficiency, considering the initial tin droplet. Following the work of Liu et al. [12], the droplet size and pre-pulse energy may be chosen to optimize target preparation. In the range of conditions relevant to the current work, a smaller droplet preformed using a higher energy pre-pulse is favorable.

An alternative mass-delivery method to tin sheets is to illuminate the undeformed droplet. This allows for a large overlap mass with the drive laser beam. By illuminating a tin droplet, a longer pulse duration can be sustained, resulting in high EUV energy emission per pulse [91]. This setup requires matching the laser beam diameter with a suitable droplet diameter. A laser beam spot size larger than the droplet

will result in energy loss as is transmitted beyond the tin target. Accordingly, scaling the output energy through expanding the beam diameter may not be suitable for unpreformed tin target systems. However, at optimum intensity, the possibility of pulses of much longer durations allow for scaling of the output EUV energy [91].

Outlook

The work presented in this thesis lays the foundation for considering plasmas driven by 2 µm wavelength lasers as an alternative to the current industrial standard of 10 µm. While we demonstrate high efficiency plasma light sources with further understanding of the full energy emission and mass use, there remain a few prospective relevant research questions.

Future work may employ the imaging-spectroscopy device described in Chapter 1. By installing this device to investigate plasma driven by 2 µm wavelength laser light, further insight into the source size and emission characteristics may be developed. With the detector mounted at 90° with respect to the laser beam, similar to the EUV imaging setup, both the longitudinal and radial characteristics may be observed. The spectral decomposition along the laser beam axis would be obtained, improving the understanding of plasma expansion and emission source size.

C

Higher conversion efficiencies may still be obtained in future experimentation if the drive laser beam quality is further improved. This expectation is based on the results obtained in Chapter 2. We report here laser beam spatial profiles of an energy enclosed of a maximum of 75 %, with a possibility to increase by optimizing the beam transport. Nevertheless, we note that such increase of beam quality is challenging for the employed master oscillator power amplifier systems. This difficulty arises due to the beam quality of the 2 µseed generated by the optical parametric oscillator as well as the low stability of the system [32]. Therefore, exploration of employing alternative drive laser systems of 2 µm wavelength may be of scientific interest. Thulium-based laser systems have already been developed and may stand as a potential candidate for such research [60, 90].

An improvement of the understanding of the experimental detectors as detailed above is of great interest to reduce the uncertainty in the valuation of emission energies from the generated plasmas. By narrowing down the uncertainty in the detected energies, and exploring additional energy loss channels, a complete reconstruction of the emission from a 2 µm wavelength driven plasma is possible.

The emission spectrum of tin plasmas exhibits a large amount of interesting unidentified features. Further work, supported by calculations of the distributions the available tin ions and excitation states may shed further light onto the origins of such unidentified emission lines.

Liu et al. [12] laid the foundation for calculating and optimizing the tin mass delivery as prepared by the pre-pulse laser. Utilizing their understanding, along with the calculations executed in Chapter 4, further studies may optimize the total mass input as is available in the initial tin droplet. The work in this thesis provides a guide to the amount of mass needed to overlap with the laser beam, for optimum EUV emitting plasmas driven by 2 µm light. This calculation of the required mass leads to a value of the required target thickness at full (radial) geometrical overlap. Subsequently, plasmas driven using preformed sheets may be generated using smaller initial droplet sizes.

Opening with and discussing the challenges of understanding the mass and energy efficiency of 2 μm wavelength laser produced tin plasmas, this thesis addresses several critical topics of relevance to such light sources. We aim to present a compelling case for the use of 2 μm wavelength light as a driver for future EUV light sources. The emission from plasmas driven by 2 μm light have been detailed in their emission efficiencies, total energies, as well as spectral character. The use of tin mass to sustain and drive the plasma has been described and addressed for relevant plasma parameters with novel identification of optimal mass. Parameters relevant to optimizing such light source have been introduced and studied, paving a way for a possibility of employing such systems in industrial applications.

Bibliography

[1]L. Poirier, A. Lassise, Y. Mostafa, L. Behnke, N. Braaksma, L. Assink, R. Hoekstra, and O. Versolato, *Energy- and charge-state-resolved spectrometry of tin laser-produced plasma using a retarding field energy analyzer*, Appl. Phys. B- Lasers O **128**, 135: 1–7 (2022).

[2]D. D. Zhang, M. R. Bennett, H. Cheng, L. Wang, H. Zhang, S. C. Reynolds, S. Zhang, X. Wang, T. Li, T. Urban, Q. Pei, Z. Wu, P. Zhang, C. Liu, Y. Wang, C. Wang, D. Zhang, and R. Lawrence Edwards, *Earliest parietal art: hominin hand and foot traces from the middle Pleistocene of Tibet*, Science Bulletin **66**, 2506–2515 (2021).

[3]M. Ameri, S. K. Costello, G. Jamison, and S. J. Scott, *Seals and Sealing in the Ancient World: Case Studies from the Near East, Egypt, the Aegean, and South Asia* (Cambridge University Press, 2018).

[4]Taiwan Semiconductor Manufacturing Company Limited, *5nm Technology*, Logic Technology (2023).

[5]Q. Huang, V. Medvedev, R. van de Kruijs, A. Yakshin, E. Louis, and F. Bijkerk, *Spectral tailoring of nanoscale EUV and soft x-ray multilayer optics*, Appl. Phys. Rev. **4**, 011104 (2017).

[6]F. Torretti, J. Sheil, R. Schupp, M. Basko, M. Bayraktar, R. Meijer, S. Witte, W. Ubachs, R. Hoekstra, O. Versolato, A. Neukirch, and J. Colgan, *Prominent radiative contributions from multiply-excited states in laser-produced tin plasma for nanolithography*, Nat. Commun. **11**, `10.1038/s41467-020-15678-y` (2020).

[7]G. O'Sullivan, B. Li, R. D'Arcy, P. Dunne, P. Hayden, D. Kilbane, T. McCormack, H. Ohashi, F. O'Reilly, P. Sheridan, E. Sokell, C. Suzuki, and T. Higashiguchi, *Spectroscopy of highly charged ions and its relevance to EUV and soft x-ray source development*, J. Phys. B: At. Mol. Opt. Phys. **48**, 144025 (2015).

[8]O. O. Versolato, J. Sheil, S. Witte, W. Ubachs, and R. Hoekstra, *Microdroplet-tin plasma sources of EUV radiation driven by solid-state-lasers (topical review)*, J. Opt. **24**, 054014 (2022).

[9]M. M. Basko, V. G. Novikov, and A. S. Grushin, *On the structure of quasi-stationary laser ablation fronts in strongly radiating plasmas*, Phys. Plasmas **22**, 053111 (2015).

[10]J. Hernandez-Rueda, B. Liu, D. J. Hemminga, Y. Mostafa, R. A. Meijer, D. Kurilovich, M. Basko, H. Gelderblom, J. Sheil, and O. O. Versolato, *Early-time hydrodynamic response of a tin droplet driven by laser-produced plasma*, Phys. Rev. Res. **4**, 013142 (2022).

[11]R. Meijer, D. Kurilovich, B. Liu, Z. Mazzotta, J. Hernandez-Rueda, O. Versolato, and S. Witte, *Nanosecond laser ablation threshold of liquid tin microdroplets*, English, Appl. Phys. A **128**, 1–8 (2022).

[12]B. Liu, D. Kurilovich, H. Gelderblom, and O. Versolato, *Mass loss from a stretching semitransparent sheet of liquid tin*, Phys. Rev. Appl. **13**, 024035: 1–10 (2020).

[13]D. Hudgins, N. Gambino, B. Rollinger, and R. Abhari, *Neutral cluster debris dynamics in droplet-based laser-produced plasma sources*, J. Phys. D: Appl. Phys. **49**, 185205 (2016).

[14]G. Yang and Y. Li, *Analysis and control of thermal and structural deformation of projection optics for 22-nm EUV lithography*, in Extreme Ultraviolet (EUV) Lithography III, Vol. 8322 (SPIE, 2012), p. 83222V.

[15]K. Liu, Y. Li, F. Zhang, and M. Fan, *Transient thermal and structural deformation and its impact on optical performance of projection optics for extreme ultraviolet lithography*, Jpn. J. Appl. Phys. **46**, 6568–6572 (2007).

[16]D. J. W. Klunder, M. M. J. W. van Herpen, V. Y. Banine, and K. Gielissen, *Debris mitigation and cleaning strategies for Sn-based sources for EUV lithography*, in Emerging lithographic technologies ix, Vol. 5751 (SPIE, 2005), pp. 943–951.

[17]S. Rai, K. Bijlsma, I. Rabadán, L. Méndez, P. Wolff, M. Salverda, O. Versolato, and R. Hoekstra, *Charge exchange in collisions of 1–100-keV Sn3+ ions with H2 and D2*, Phys. Rev. A **106**, 012804: 1–10 (2022).

[18]C. Luijten, *Energy saving in semiconductor manufacturing as design goal*, Feb. 2020.

[19]K. Kouge, S. Nagai, T. Hori, Y. Ueno, T. Yanagida, K. Miyao, H. Hayashi, Y. Watanabe, T. Abe, H. Nakarai, T. Saito, and H. Mizoguchi, *Update of development progress of the high power LPP-EUV light source using a magnetic field*, J. Photopolym. Sci. Technol. **33**, 37–44 (2020).

[20]M. A. van de Kerkhof, F. Liu, M. Meeuwissen, X. Zhang, M. Bayraktar, R. C. de Kruif, and N. V. Davydova, *High-power EUV lithography: spectral purity and imaging performance*, J. Micro/ Nanolithogr. MEMS MOEMS **19**, 033801 (2020).

[21]R. Schupp, F. Torretti, R. Meijer, M. Bayraktar, J. Scheers, D. Kurilovich, A. Bayerle, K. Eikema, S. Witte, W. Ubachs, R. Hoekstra, and O. Versolato, *Efficient generation of extreme ultraviolet light from Nd:YAG-driven microdroplet-tin plasma*, Phys. Rev. Appl. **12**, 014010: 1–11 (2019).

[22]R. Schupp, L. Behnke, J. Sheil, Z. Bouza, M. Bayraktar, W. Ubachs, R. Hoekstra, and O. O. Versolato, *Characterization of 1- and 2−μm-wavelength laser-produced microdroplet-tin plasma for generating extreme-ultraviolet light*, Phys. Rev. Res. **3**, 013294 (2021).

[23]S. H. Langer, H. A. Scott, T. C. Galvin, E. S. Link, B. A. Reagan, and C. W. Siders, *Simulations of laser driven EUV sources - the impact of laser wavelength*, in Proceedings of EUVL workshop (June 2020).

[24]D. J. Hemminga, O. O. Versolato, and J. Sheil, *Simulations of plasmas driven by laser wavelengths in the 1.064—10.6 μm range for their characterization as future extreme ultraviolet light sources*, Phys. Plasmas **30**, 033301 (2023).

[25]I. Y. Tolstikhina, S. Churilov, A. Ryabtsev, K. Koshelev, and V. Bakshi, "Euv source requirements for euv lithography", in *EUV Sources for Lithography*, edited by V. Bakshi (SPIE press Bellingham, Washington, Oxford, 2006) Chap. 2.

[26]I. Fomenkov, D. Brandt, A. Ershov, A. Schafgans, Y. Tao, G. Vaschenko, S. Rokitski, M. Kats, M. Vargas, M. Purvis, et al., *Light sources for high-volume manufacturing EUV lithography: technology, performance, and power scaling*, Adv. Opt. Technol. **6**, 173–186 (2017).

[27]R. Schupp, L. Behnke, Z. Bouza, Z. Mazzotta, Y. Mostafa, A. Lassise, L. Poirier, J. Sheil, M. Bayraktar, W. Ubachs, R. Hoekstra, and O. O. Versolato, *Characterization of angularly resolved EUV emission from 2-μm-wavelength laser-driven Sn plasmas using preformed liquid disk targets*, J. Phys. D: Appl. Phys. **54**, 365103 (2021).

[28]L. Behnke, R. Schupp, Z. Bouza, M. Bayraktar, Z. Mazzotta, R. Meijer, J. Sheil, S. Witte, W. Ubachs, R. Hoekstra, and O. O. Versolato, *Extreme ultraviolet light from a tin plasma driven by a 2-μm-wavelength laser*, Opt. Express **29**, 4475–4487 (2021).

[29]I. Tamer, B. A. Reagan, T. Galvin, F. Batysta, E. Sistrunk, D. Willard, A. Church, H. Neurath, J. Galbraith, G. Huete, and T. Spinka, *1 GW peak power and 100 J pulsed operation of a diode-pumped Tm:YLF laser*, Opt. Express **30**, 46336–46343 (2022).

B

[30]B. A. Reagan, I. Tamer, T. Galvin, F. Batysta, E. Sistrunk, D. Willard, A. Church, H. Neurath, J. Galbraith, G. Huete, C. Siders, S. Langer, and T. Spinka., *1 GW peak power and 100 J pulsed operation of a diode pumped λ= 1.9 µm laser*, in EUV Source Workshop 2022 Proceedings (Oct. 2022).

[31]R. A. Burdt, S. Yuspeh, K. L. Sequoia, Y. Tao, M. S. Tillack, and F. Najmabadi, *Experimental scaling law for mass ablation rate from a Sn plasma generated by a 1064 nm laser*, J. Appl. Phys. **106**, 033310 (2009).

[32]L. Behnke, E. J. Salumbides, G. Göritz, Y. Mostafa, D. Engels, W. Ubachs, and O. Versolato, *High-energy parametric oscillator and amplifier pulsed light source at 2-µm*, Opt. Express **31**, 24142–24156 (2023).

[33]O. O. Versolato, *Physics of laser-driven tin plasma sources of EUV radiation for nanolithography*, Plasma Sources Sci. Technol. **28**, 083001 (2019).

[34]V. Y. Banine, K. N. Koshelev, and G. H. P. M. Swinkels, *Physical processes in EUV sources for microlithography*, J. Phys. D: Appl. Phys. **44**, 253001 (2011).

[35]M. Purvis, I. V. Fomenkov, A. A. Schafgans, M. Vargas, S. Rich, Y. Tao, S. I. Rokitski, M. Mulder, E. Buurman, M. Kats, J. Stewart, A. D. LaForge, C. Rajyaguru, G. Vaschenko, A. I. Ershov, R. J. Rafac, M. Abraham, D. C. Brandt, and D. J. Brown, *Industrialization of a robust EUV source for high-volume manufacturing and power scaling beyond 250 W*, in Extreme Ultraviolet Lithography IX, Vol. 10583 (SPIE, 2018), pp. 476–485.

[36]H. Mizoguchi, H. Nakarai, T. Abe, K. M. Nowak, Y. Kawasuji, H. Tanaka, Y. Watanabe, T. Hori, T. Kodama, Y. Shiraishi, T. Yanagida, G. Soumagne, T. Yamada, T. Yamazaki, and T. Saitou, *High power LPP-EUV source with long collector mirror lifetime for high volume semiconductor manufacturing*, in CSTIC (2018), pp. 1–7.

[37]Z. Bouza, J. Byers, J. Scheers, R. Schupp, Y. Mostafa, L. Behnke, Z. Mazzotta, J. Sheil, W. Ubachs, R. Hoekstra, M. Bayraktar, and O. O. Versolato, *The spectrum of a 1-µm-wavelength-driven tin microdroplet laser-produced plasma source in the 5.5–265.5 nm wavelength range*, en, AIP Adv. **11**, 125003 (2021).

[38]F. Torretti, A. Windberger, A. Ryabtsev, S. Dobrodey, H. Bekker, W. Ubachs, R. Hoekstra, E. V. Kahl, J. C. Berengut, J. R. Crespo López-Urrutia, and O. O. Versolato, *Optical spectroscopy of complex open-4d-shell ions Sn^{7+}-Sn^{10+}*, Phys. Rev. A **95**, 042503 (2017).

[39]J. Scheers, C. Shah, A. Ryabtsev, H. Bekker, F. Torretti, J. Sheil, D. A. Czapski, J. C. Berengut, W. Ubachs, J. R. C. López-Urrutia, R. Hoekstra, and O. O. Versolato, *EUV spectroscopy of highly charged Sn^{13+}-Sn^{15+} ions in an electron-beam ion trap*, Phys. Rev. A **101**, 062511 (2020).

[40]R. M. van der Horst, J. Beckers, E. A. Osorio, D. I. Astakhov, W. J. Goedheer, C. J. Lee, V. V. Ivanov, V. M. Krivtsum, K. N. Koshelev, D. V. Lopaev, F. Bijkerk, and V. Y. Banine, *Exploring the electron density in plasma induced by EUV radiation: I. Experimental study in hydrogen*, J. Phys. D: Appl. Phys. **49**, 145203 (2016).

[41]F. Döring, B. Rösner, M. Langer, A. Kubec, A. Kleibert, J. Raabe, C. A. F. Vaz, M. Lebugle, and C. David, *Multifocus off-axis zone plates for x-ray free-electron laser experiments*, Optica **7**, 1007–1014 (2020).

[42]J. O. Schunck, F. Döring, B. Rösner, J. Buck, R. Y. Engel, P. S. Miedema, S. K. Mahatha, M. Hoesch, A. Petraru, H. Kohlstedt, C. Schüssler-Langeheine, K. Rossnagel, C. David, and M. Beye, *Soft x-ray imaging spectroscopy with micrometer resolution*, Optica **8**, 156–160 (2021).

[43]A. V. Baez, *Fresnel zone plate for optical image formation using extreme ultraviolet and soft x radiation*, J. Opt. Soc. Am. **51**, 405–412 (1961).

B

[44]F. Marschall, Z. Yin, J. Rehanek, M. Beye, F. Döring, K. Kubiček, D. Raiser, S. T. Veedu, J. Buck, A. Rothkirch, et al., *Transmission zone plates as analyzers for efficient parallel 2D RIXS-mapping*, Sci. Rep. **7**, 8849 (2017).

[45]A. Jonas, T. Meurer, B. Kanngießer, and I. Mantouvalou, *Reflection zone plates as highly resolving broadband optics for soft X-ray laboratory spectrometers*, Rev. Sci. Instrum. **89**, 026108 (2018).

[46]S. Ali and C. Jacobsen, *Effect of tilt on circular zone plate performance*, J. Opt. Soc. Am. A **37**, 374–383 (2020).

[47]L. E. Ocola, J. Maser, S. Vogt, B. Lai, R. Divan, and G. B. Stephenson, *Tapered tilted linear zone plates for focusing hard x-rays*, in SPIE Proceedings, Vol. 5539 (Nov. 2004), pp. 165–173.

[48]K. Li and C. Jacobsen, *More are better, but the details matter: combinations of multiple Fresnel zone plates for improved resolution and efficiency in X-ray microscopy*, J. Synchrotron Rad. **25**, 1048–1059 (2018).

[49]S. J. Goh, H. M. J. Bastiaens, B. Vratzov, Q. Huang, F. Bijkerk, and K. J. Boller, *Fabrication and characterization of free-standing, high-line-density transmission gratings for the vacuum UV to soft x-ray range*, Opt. Express **23**, 4421–4434 (2015).

[50]M. Bayraktar, H. M. J. Bastiaens, C. Bruineman, B. Vratzov, and F. Bijkerk, *Broadband transmission grating spectrometer for measuring the emission spectrum of EUV sources*, NEVAC blad **54**, 14–19 (2016).

[51]R. Schupp, F. Torretti, R. A. Meijer, M. Bayraktar, J. Sheil, J. Scheers, D. Kurilovich, A. Bayerle, A. A. Schafgans, M. Purvis, K. S. E. Eikema, S. Witte, W. Ubachs, R. Hoekstra, and O. O. Versolato, *Radiation transport and scaling of optical depth in Nd:YAG laser-produced microdroplet-tin plasma*, Appl. Phys. Lett. **115**, 124101 (2019).

[52]K. Matsushima and T. Shimobaba, *Band-limited angular spectrum method for numerical simulation of free-space propagation in far and near fields*, Opt. Express **17**, 19662–19673 (2009).

[53]H. W. Schnopper, L. P. V. Speybroeck, J. P. Delvaille, A. Epstein, E. Källne, R. Z. Bachrach, J. Dijkstra, and L. Lantward, *Diffraction grating transmission efficiencies for XUV and soft x rays*, Appl. Opt. **16**, 1088–1091 (1977).

[54]M. Waldrop, *The chips are down for Moore's law*, Nat. News **530**, 144 (2016).

[55]J. van Schoot, K. Troost, F. Bornebroek, R. van Ballegoij, S. Lok, P. Krabbendam, J. Stoeldraijer, J. Benschop, J. Finders, H. Meiling, E. van Setten, B. Kneer, P. Kuerz, W. Kaiser, T. Heil, and S. Migura, *The future of EUV lithography: continuing Moore's Law into the next decade*, in Extreme Ultraviolet Lithography IX, Vol. 10583 (2018), 105830R.

[56]A. Sasaki, A. Sunahara, H. Furukawa, K. Nishihara, S. Fujioka, T. Nishikawa, F. Koike, H. Ohashi, and H. Tanuma, *Modeling of radiative properties of Sn plasmas for extreme-ultraviolet source*, J. Appl. Phys. **107**, 113303 (2010).

[57]Y. Nishimura, Y. Ueno, S. Nagai, F. Iwamoto, K. Miyao, H. Hayashi, Y. Watanabe, T. Abe, H. Nakarai, and H. Mizoguchi, *Key technology development progress of the high power LPP-EUV light source*, in Optical and EUV Nanolithography XXXV, Vol. 12051 (2022), 120510T.

[58]T. Kentaro, Y. Pan, A. Sunahara, K. Kouge, H. Mizoguchi, and K. Nishihara, *Observation of plasma inflows in laser-produced sn plasma and their contribution to extreme-ultraviolet light output enhancement*, Sci. Rep. **13**, 10.1038/s41598-023-28500-8 (2023).

[59]Z. Y. Shi, Y. Yuan, W. P. Wang, Y. Y. Ma, X. Y. Sun, N. Lin, and Y. X. Leng, *Enhanced extreme ultraviolet conversion efficiency of a 2 μm laser-driven preformed tin-droplet target using short picosecond pre-pulses*, Phys. Plasmas **30**, 043107 (2023).

[60]I. Tamer, B. A. Reagan, T. Galvin, J. Galbraith, E. Sistrunk, A. Church, G. Huete, H. Neurath, and T. Spinka, *Demonstration of a compact, multi-joule, diode-pumped tm:ylf laser*, Opt. Lett. **46**, 5096–5099 (2021).

[61]T. Sizyuk and A. Hassanein, *Tuning laser wavelength and pulse duration to improve the conversion efficiency and performance of EUV sources for nanolithography*, Phys. Plasmas **27**, 103507 (2020).

[62]M. Brandstätter, M. M. Weber, and R. S. Abhari, *Non-axisymmetric droplet irradiation effects on ion and extreme ultraviolet light emission of laser-produced plasma light sources*, J. Appl. Phys. **129**, 233306 (2021).

[63]Y. Yuan, Y. Y. Ma, W. P. Wang, S. J. Chen, Y. Cui, M. Zi, X. H. Yang, G. B. Zhang, and Y. X. Leng, *Enhancing the conversion efficiency of extreme ultraviolet light sources using a 2 μm wavelength laser*, Plasma Phys. Control. Fusion **64**, 025001 (2021).

[64]L. Yin, H. Wang, B. A. Reagan, C. Baumgarten, Z. Lyu, R. Soufli, E. Gullikson, V. N. Shlyaptsev, and J. J. Rocca, *Using temporally synthesized laser pulses to enhance the conversion efficiency of Sn plasmas for EUV lithography*, IEEE Photonics J. **13**, 1–15 (2021).

[65]Z. Bouza, J. Scheers, A. Ryabtsev, R. Schupp, L. Behnke, C. Shah, J. Sheil, M. Bayraktar, J. R. C. López-Urrutia, W. Ubachs, R. Hoekstra, and O. O. Versolato, *EUV spectroscopy of Sn5+–Sn10+ ions in an electron beam ion trap and laser-produced plasmas*, J. Phys. B: At. Mol. Opt. Phys. **53**, 195001 (2020).

[66]J. Filevich, J. J. Rocca, E. Jankowska, E. C. Hammarsten, K. Kanizay, M. C. Marconi, S. J. Moon, and V. N. Shlyaptsev, *Two-dimensional effects in laser-created plasmas measured with soft-x-ray laser interferometry*, Phys. Rev. E **67**, 056409 (2003).

[67]J. Sheil, O. Versolato, V. Bakshi, and H. Scott, *Review of the 1st EUV light sources code comparison workshop*, Atoms **11**, `10.3390/atoms11100130` (2023).

[68]F. Torretti, R. Schupp, D. Kurilovich, A. Bayerle, J. Scheers, W. Ubachs, R. Hoekstra, and O. O. Versolato, *Short-wavelength out-of-band EUV emission from sn laser-produced plasma*, J. Phys. B: At. Mol. Opt. Phys. **51**, 045005 (2018).

[69]A. Roy, G. Arai, H. Hara, T. Higashiguchi, H. Ohashi, A. Sunahara, B. Li, P. Dunne, G. O'Sullivan, T. Miura, T. Mocek, and A. Endo, *Evolution of laser-produced Sn extreme ultraviolet source diameter for high-brightness source*, Appl. Phys. Lett. **105**, 074103 (2014).

[70]Z. Bouza, "Developments for broadband spectral and spatial characterization of tin plasma light sources for EUV lithography", PhD thesis (Oct. 2023).

[71]A. N. Heays, A. D. Bosman, and E. F. van Dishoeck, *Photodissociation and photoionisation of atoms and molecules of astrophysical interest*, A&A **602**, A105 (2017).

[72]R. M. van der Horst, J. Beckers, E. A. Osorio, D. I. Astakhov, W. J. Goedheer, C. J. Lee, V. V. Ivanov, V. M. Krivtsum, K. N. Koshelev, D. V. Lopaev, F. Bijkerk, and V. Y. Banine, *Exploring the electron density in plasma induced by EUV radiation: I. experimental study in hydrogen*, J. Phys. D: Appl. Phys. **49**, 145203 (2016).

[73]F. Torretti, F. Liu, M. Bayraktar, J. Scheers, Z. Bouza, W. Ubachs, R. Hoekstra, and O. Versolato, *Spectral characterization of an industrial EUV light source for nanolithography*, J. Phys. D: Appl. Phys. **53**, 055204 (2019).

[74]L. Poirier, A. Bayerle, A. Lassise, F. Torretti, R. Schupp, L. Behnke, Y. Mostafa, W. Ubachs, O. Versolato, and R. Hoekstra, *Cross-calibration of a combined electrostatic and time-of-flight analyzer for energy- and charge-state-resolved spectrometry of tin laser-produced plasma*, Appl. Phys. B- Lasers O **128**, 39: 1–11 (2022).

[75]A. Kramida, Yu. Ralchenko, J. Reader, and and NIST ASD Team, NIST Atomic Spectra Database (ver. 5.11), [Online]. Available: `https://physics.nist.gov/asd` [2024, January 25]. NIST, Gaithersburg, MD. 2023.

B

[76]D. Hemminga, L. Poirier, M. Basko, R. Hoekstra, W. Ubachs, O. Versolato, and J. Sheil, *High-energy ions from Nd:YAG laser ablation of tin microdroplets: comparison between experiment and a single-fluid hydrodynamic model*, Plasma Sources Sci. Technol. **30**, 105006: 1–10 (2021).

[77]R. A. Burdt, Y. Ueno, Y. Tao, S. Yuspeh, M. S. Tillack, and F. Najmabadi, *Recombination effects during expansion into vacuum in laser produced Sn plasma*, Appl. Phys. Lett. **97**, 041502 (2010).

[78]I. Roudskoy, *General features of highly charged ion generation in laser-produced plasmas*, Laser Part. Beams **14**, 369–384 (1996).

[79]J. Sheil, L. Poirier, A. C. Lassise, D. J. Hemminga, S. Schouwenaars, N. Braaksma, A. Frenzel, R. Hoekstra, and O. O. Versolato, *Power-law scaling relating the average charge state and kinetic energy in expanding laser-driven plasmas*, Phys. Rev. Lett. **133**, 125101 (2024).

[80]J. Heymes, M. Soman, G. Randall, A. Gottwald, A. Harris, A. Kelt, I. Moody, X. Meng, and A. D. Holland, *Comparison of back-thinned detector ultraviolet quantum efficiency for two commercially available passivation treatments*, IEEE TNS **67**, 1962–1967 (2020).

[81]L. Poirier, A. Lassise, R. Hoekstra, J. Sheil, and O. Versolato, *Dependence of ion charge-energy emission from Nd:YAG-laser-produced plasma on laser intensity in the 0.4–40×10^{10} W/cm2 range*, Phys. Plasmas **30**, 083505 : 1–10 (2023).

[82]L. Poirier, “Ion diagnostics for extreme ultraviolet nanolithography”, PhD thesis (Oct. 2023).

[83]D. Kurilovich, “Laser-induced dynamics of liquid tin microdroplets”, PhD thesis (Apr. 2019).

[84]H. Gelderblom, H. Lhuissier, A. L. Klein, W. Bouwhuis, D. Lohse, E. Villermaux, and J. H. Snoeijer, *Drop deformation by laser-pulse impact*, Journal of Fluid Mechanics **794**, 676–699 (2016).

[85]E. Villermaux and B. Bossa, *Drop fragmentation on impact*, J. Fluid Mech. **668**, 412–435 (2011).

[86]D. Hemminga, “Single-fluid radiation-hydrodynamic modeling of laser-driven EUV-emitting plasmas”, PhD thesis (Nov. 2023).

[87]D. D. Hickstein, S. T. Gibson, R. Yurchak, D. D. Das, and M. Ryazanov, *A direct comparison of high-speed methods for the numerical Abel transform*, Rev. Sci. Instrum. **90**, 065115 (2019).

[88]S. Gibson, D. D. Hickstein, R. Yurchak, M. Ryazanov, D. Das, and G. Shih, *Pyabel/pyabel: v0.9.0*, version v0.9.0, Dec. 2022.

[89]F. Dahmani and T. Kerdja, *Measurements and laser-wavelength dependence of mass-ablation rate and ablation pressure in planar layered targets*, Laser Part. Beams **9**, 769–778 (1991).

[90]C. W. Siders, A. C. Erlandson, T. C. Galvin, H. Frank, S. Langer, B. A. Reagan, H. Scott, E. F. Sistrunk, and T. M. Spinka, *Efficient high power laser drivers for next-generation high power EUV sources*, in Proc. of EUV Source Workshop (Nov. 2019).

[91]S. J. J. de Lange, D. J. Hemminga, Y. Mostafa, R. A. Meijer, O. O. Versolato, and J. Sheil, *Modeling the hundreds-of-nanoseconds-long irradiation of tin droplets with a 2 μm-wavelength laser for future EUV lithography*, PSST **33**, 105003 (2024).

B

List of Publications

CHAPTER 1
Y. Mostafa, Z. Bouza, J. Byers, I. Babenko, W.M.G. Ubachs, O.O. Versolato and M. Bayraktar, *Extreme ultraviolet broadband imaging spectrometer using dispersion-matched zone plates*, Opt. Lett. **48**(16) (2023).
Chosen as Editor's Pick

CHAPTER 2
Y. Mostafa, L. Behnke, D. J. Engels, Z. Bouza, J. Sheil, W. Ubachs, and O. O. Versolato, *Production of 13.5 nm Light with 5% Conversion Efficiency from 2 μm Laser Driven Tin Microdroplet Plasma*, Appl. Phys. Lett. **123** (2023).

The author has also contributed to the following publication:

R. Schupp, L. Benhke, Z. Bouza, Z. Mazzotta, **Y. Mostafa**, A. Lassise, L. Poirier, J. Sheil, M. Bayraktar, W. Ubachs, R. Hoekstra, and O. O. Versolato, *Characterization of angularly resolved EUV emission from 2-μm-wavelength laser-driven Sn plasmas using preformed liquid disk targets*, J. Phys. D **54** (2021).

Z. Bouza, J. Byers, J. Scheers, R. Schupp, **Y. Mostafa**, L.P. Behnke, Z. Mazzotta, J. Sheil, W.M.G. Ubachs, R. Hoekstra, M. Bayraktar, and O.O. Versolato, *The spectrum of a 1-μm-wavelength-driven tin microdroplet laser-produced plasma source in the 5.5–265.5 nm wavelength range*, AIP Adv. **11**(12) (2021).

J. Hernandez-Rueda, B. Liu, D. J. Hemminga, **Y. Mostafa**, R. A. Meijer, D. Kurilovich, M. Basko, H. Gelderblom, J. Sheil, and O. O. Versolato, *Early-time hydrodynamic response of a tin droplet driven by laser-produced plasma*, Phys. Rev. Research **4** (2022).

L. Poirier, A. Bayerle, A. Lassise, F. Torretti, R. Schupp, L. Behnke, **Y. Mostafa**, W. Ubachs, O. O. Versolato, and R. Hoekstra, *Cross-calibration of a combined electrostatic and time-of-flight analyzer for energy-and charge-state-resolved spectrometry of tin laser-produced plasma*, Appl. Phys. B. **128**(3) (2022).

L. Poirier, A. Lassise, **Y. Mostafa**, L.P. Behnke, N. Braaksma, L. Assink, R. Hoekstra, and O.O. Versolato, *Energy- and charge-state-resolved spectrometry of tin laser-produced plasma using a retarding field energy analyzer*, Appl. Phys. B- Lasers O **128**(7) (2022).

L.P. Behnke, E.J. Salumbides, G. Göritz, **Y. Mostafa**, D.J. Engels, W.M.G. Ubachs and O.O. Versolato, *High-energy parametric oscillator and amplifier pulsed light source at 2-μm*, Opt. Express **31**(15) (2023).

S.J.J. de Lange, D.J. Hemminga, **Y. Mostafa**, R.A. Meijer, and J. Sheil, *Modeling the hundreds-of-nanoseconds-long irradiation of tin droplets with a 2 μm-wavelength laser for future EUV lithography*, PSST **33**(10) (2024).

I. Babenko, **Y. Mostafa**, Z. Bouza, O.O. Versolato and M. Bayraktar, *Spectral and spatial resolution of an extreme ultraviolet broadband imaging spectrometer based on dispersion-matched zone plates*, AIP Adv. **14**(10) (2024).

Acknowledgements

> If I have seen further than others,
> it is by standing upon the shoulders of giants.
>
> *Isaac Newton*

This thesis, and the work leading to and supporting it, would not have been possible without the help and guidance of many.

To **Oscar Versolato**, thank you for your mentorship and support during my time in your group. I appreciate the opportunity to engage in the world of plasma physics and for the experiences I gained over the past four years. I wish you and your team continued success. Thank you, **John Sheil**, for your supervision and the many insightful discussions we shared about our research. Your guidance has been valuable, and I wish you and your group the best of luck in the future. I would also like to extend my gratitude to **Wim Ubachs** and **Ronnie Hoekstra** for their support and contributions throughout my PhD journey.

To my paranymphs, thank you for supporting this thesis throughout its entire journey. **Kevin Murzyn**, a bond that survives both bingo night and crying in the French forest is one that lasts forever. Kevin, 7A by 2025! **Diana Potse**, who would have thought indeed? Ever since meeting at USVA, we have been a great duo, just like fire and ice (=warm water). Thank you both for your support throughout the last years and on my defense day!

To my colleagues, thank you all for making this work possible and creating a fun atmosphere to carry out research. **Lucas Poirier**, from sliding on your skateboard to *Font*, we have formed a very valuable friendship that is close to my heart. Your contributions to this thesis, scientific and otherwise, are very much appreciated. **Zoi Bouza**, from very early on I knew we would get along very well. We collaborated on a few topics that featured in both our theses. You made going to work a fun part of the day for me and we formed a Mediterranean friendship that will last forever! **Lars Behnke**, working with you was fantastic in many ways. We spent many days and weekends together in the lab and I will remember those days fondly. From walking on (and falling in) the frozen Ij, to our boat days around Amsterdam, you are missed in the Netherlands but I hope you are enjoying sunny state! To the one who taught me it all, **Ruben Schupp**, thank you! Your skills of laser-on-droplet alignment deserved nothing but applause. Although you carried on in your success elsewhere, we remained in contact all those years, and I hope for years to come. Keep digging!

I would like to further thank my colleagues and collaborators for their significant contributions to the work within this thesis. **Diko Hemminga**, **Adam Lassise**, **Dion Engels**, **Jane Babenko**, **Karl Schubert**, **Xyoisan Danser**, **Stan de Lange**, **Mardou Bijker**, **Luc Assink**, **Klaas Bijlsma**, **Emiel de Wit**, **Mart Salverda**, **Christos Messinis**, **Kevin Mongey**, **Sander Schouwenaars**, **Edcel Salumbides**, **Hugo França**, **Mengqi Du**, **Randy Meijers**, **Bo Liu**, **Javier Hernández**, **James Byers**, **Ksenia Abrashitova** and **Matthijs Velsink**, thank you all for your valuable work and I wish you further success with your careers.

The experimental work in this thesis is majorly supported by **Laurens van Buuren**. Laurens, thank you so much for everything you do, you act as the backbone to all our

research endeavours. I enjoyed our chats in and outside of the lab about concerts, baseball and more. I wish you all the best! **Nik Noest-Hermans** and **Arend-Jan van Calcar**, thank you for all your help! I would like to further thank **Henk-Jan Boluijt** and **Iliya Cerjak**, your engineering excellence has enabled many of the advances set forth in this work.

To **Jorijn Kuster** and **Marco Konijnenburg**, thank you for your continuous support of the data acquisition software. I was always amazed by what you have enabled and how fast you respond to our requests. Almost all data presented in this thesis has been acquired flawlessly and channeled through your scripts. I would like to extend my thanks to **Duncan Verheijde** and **Pepijn Huider** for their support of electronic components and read-out devices. Without your valuable work, time-resolved EUV emission and Sn ion charge analyses would not be possible.

Thank you **Marjan Fretz** for providing the support and structure that enables all these projects and many more. **Joost Frenken** and **Wim van der Zande**, thank you for providing the leadership for ARCNL.

To **Muharrem Bayraktar**, thank you for the very productive discussions and for the opportunity to collaborate on the imaging spectrometer, it was a great pleasure! **Michael Purvis**, I appreciate our talks and discussions even though we are separated by 9000 km. Your feedback has really driven our studies forward.

Thank you, **Tamalika**, for your continued support and guidance over the last 5 years! My interest and love for physics and establishing a welcoming academic atmosphere were fueled during my time working with you. I wish you all the best!

Sherif, we have known each other since we were 6 years old. Through great times and terrible times we stood together. There's no one I would rather discuss everything with, whether international politics or street stand candies, more than you. I with you best of luck in Vancouver and a healthy future!

Lina, we have grown closer despite the now longer distance. I hope this bond continues to strengthen! **Felipe**, for much of the time we have known together, we shared very similar experiences. Thanks for being there and for our daily talks. My movie recommendation to you is Kira and El Gin! To my podcast co-host, **Sandra**, thank you for all the amazing road trips we have had! Next time, no wasps! Despite living in different countries, **Marisa**, our friendship is as strong as it always has been. Ever since the Acco weekend away and making friends with sheep #12562, we have had a strong connection. **Maria**, I am very thankful for the laughter and great times we had together, I hope that continues in the future. Thank you **Alfid** for always being there. Our talks always brought me serenity and excitement for the future.

Jack, sorry I frustrated you as the 'obnoxious American' in Onderwater's class. If it was not for that we would not be measuring muon lifetimes, listening to live jazz, sailing in the North Sea, dancing to Parov Stellar and upholding our two nations' treaties. We have truly made a lasting friendship! But remember, cold is just an emotion. Now, **Vincent**, we first met on your 18$^{\text{th}}$ birthday in 2015! Since then we have done every single bachelor and masters courses together where your curiosity and intelligence drove me to reach for excellence. From steak nights on Christmas, Kroton TSD, and spending hours on an SEM, we have come a long way. And do not worry guys, I have not been to De Negende Cirkel since.

Youssef, Omar, Ahmed, may our timeless calls never end. I wish you all the best in your careers and life!

To my parents, thank you for the incredible support throughout all these years. None of what I do today would be possible without your guidance and motivation to explore and test out new things. **Alia**, thank you for everything. You always stood as the guiding role model for my life and continue to be so. I wish all the best to you and your family!